



Terms and Conditions of Use of Digitised Theses from Trinity College Library Dublin

Copyright statement

All material supplied by Trinity College Library is protected by copyright (under the Copyright and Related Rights Act, 2000 as amended) and other relevant Intellectual Property Rights. By accessing and using a Digitised Thesis from Trinity College Library you acknowledge that all Intellectual Property Rights in any Works supplied are the sole and exclusive property of the copyright and/or other IPR holder. Specific copyright holders may not be explicitly identified. Use of materials from other sources within a thesis should not be construed as a claim over them.

A non-exclusive, non-transferable licence is hereby granted to those using or reproducing, in whole or in part, the material for valid purposes, providing the copyright owners are acknowledged using the normal conventions. Where specific permission to use material is required, this is identified and such permission must be sought from the copyright holder or agency cited.

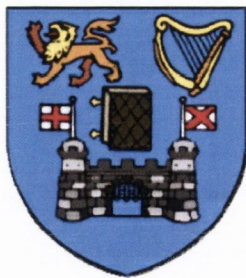
Liability statement

By using a Digitised Thesis, I accept that Trinity College Dublin bears no legal responsibility for the accuracy, legality or comprehensiveness of materials contained within the thesis, and that Trinity College Dublin accepts no liability for indirect, consequential, or incidental, damages or losses arising from use of the thesis for whatever reason. Information located in a thesis may be subject to specific use constraints, details of which may not be explicitly described. It is the responsibility of potential and actual users to be aware of such constraints and to abide by them. By making use of material from a digitised thesis, you accept these copyright and disclaimer provisions. Where it is brought to the attention of Trinity College Library that there may be a breach of copyright or other restraint, it is the policy to withdraw or take down access to a thesis while the issue is being resolved.

Access Agreement

By using a Digitised Thesis from Trinity College Library you are bound by the following Terms & Conditions. Please read them carefully.

I have read and I understand the following statement: All material supplied via a Digitised Thesis from Trinity College Library is protected by copyright and other intellectual property rights, and duplication or sale of all or part of any of a thesis is not permitted, except that material may be duplicated by you for your research use or for educational purposes in electronic or print form providing the copyright owners are acknowledged using the normal conventions. You must obtain permission for any other use. Electronic or print copies may not be offered, whether for sale or otherwise to anyone. This copy has been supplied on the understanding that it is copyright material and that no quotation from the thesis may be published without proper acknowledgement.



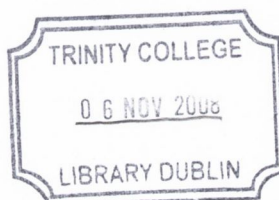
Mechanical Properties of Biopolymers Reinforced with Carbon Nanotubes

By
David Blond

A thesis submitted for the degree of
Doctor of Philosophy
At the
University of Dublin

School of Physics
Trinity College Dublin

2008



THESIS
8652

DECLARATION

This thesis has not been submitted as an exercise for a degree at any other university. Except where stated, the work described therein was carried out by me alone.

I give permission for the Library to lend or copy this thesis upon request.

Signed:

A handwritten signature in blue ink, consisting of a series of loops and a long horizontal stroke extending to the right.

Declaration

I declare that the work in this dissertation has not been previously submitted as an exercise for a degree to this or any other university.

The work described herein is entirely my own work, except for the assistance mentioned in the acknowledgements and the collaborative work mentioned in the list of publications.

I agree that Trinity College Dublin may lend this dissertation on request.



David Blond

“Education is a progressive discovery of our own ignorance.”
Will Durant (1885-1981)

“The most exciting phrase to hear in science, the one that heralds new discoveries, is not
“Eureka!” (I found it!) but “That's funny”...”
Isaac Asimov (1920-1992)

Acknowledgements

Most importantly, I would like to thank Prof. Werner Blau who gave me the opportunity to study for a PhD and for both his scientific and financial support. It was a great pleasure to have been involved in such a friendly, stimulating and rewarding group. Equal thanks must go to Prof. Jonathan Coleman for all of his supervision, and assistance. I am extremely grateful to both of you for all of the support, expertise and ample opportunities for travel to conferences over the years. Without this help, this thesis would not have been possible.

I would like to thank Dr Valerie Barron for her help and supervision first as an ERASMUS student and then during the early stages of my PhD. I also would like to thank her and Joseph Mackle for the collaboration with the NCBES of Galway.

I also would like to thank Prof Boland for his collaboration in the electrospinning project. I would like to thank especially Dorothee Almecija who carried out all the sample preparations and the AFM measurements on electrospun nanofibres.

I would like to express my gratitude to Dr Emer Lahiff, Siobhan Colfer, Helen Cathcart, Dr James Doyle, Dr Robert Murphy and Dr Denis McCarthy for proof reading this thesis. That was greatly appreciated. You have my “french” word.

From the group, first of all I would like to thank you all (past and present members) for working together and having a great amount of fun inside and outside the College. Thanks to Dr Leslie Carpenter, Dr Manuel Ruether and Dr Colin Belton for their useful advices. Special thanks go to Fiona J Blighe, William Walshe, Nick Piskunov, Martin Djiango and Karen Young for their huge help in the electrospinning project. Thanks also to Dr Martin Cadek, Dr Kevin Ryan, Dr Valeria Nicolosi and Umar Khan for sharing their knowledge and time in the PMMA and PLLA projects. I would like to thank Dr Rory Leahy and Neill McEvoy for the Raman measurements Darren Lee who saves me a lot of time on computer issues.

Lots of thanks has to go to Joe McCauley, Mick Reilly, Dave Grouse, Pat Murphy and Gordon O'Brien who gave me a huge help to built the electrospinning set up. I would like to thank everyone in the Centre for Microscopy Analysis, and in particular Neal Leddy. I also would like to thank the MI crew especially, Dr Chris Keely, Dr Ramesh Babu, Keith Fortune, Trevor Wood, Dr Gordon Armstrong who provided knowledge expertise and assistance in my research. Thanks to Jeanette Cummins John, Kelly

and Ken Concannon for all the administrative and technical support they provided and Liam Brennan at NUI Galway for his technical support.

Finally I want to dedicate a very special thanks to my parents for their unconditional support and patience from the beginning. Without you this achievement wouldn't be possible, I dedicate this thesis to you. Big thanks to the rest of the family, Thierry, Karen, Ghislain (Agathe, Quentin and ?). Last but not least, Estelle for everything and especially your patience and understanding.

Table of Contents

Declaration	i
Acknowledgements.....	iii
Table of Contents.....	iv
List of Tables.....	viii
List of Figures and Illustrations.....	ix
Abstract.....	xiii
Chapter 1. Introduction.....	1
1.1 Background and Motivation.	1
1.2 Thesis Outline.....	3
1.3 References.....	4
Chapter 2: Materials & Background.	5
2.1 Introduction.....	5
2.2 Polymers.	5
2.2.1 Introduction to Polymers.	5
2.2.2 Poly (methyl methacrylate).....	7
2.2.3 Poly(vinyl alcohol).	9
2.2.4 Poly (lactic Acid).	10
2.2.5 Biosteel ®.	10
2.3 Carbon Nanotubes.....	14
2.3.1 Physical Properties of Carbon Nanotubes.	14
2.3.2 Electronic Properties of Carbon Nanotubes.....	18
2.3.3 Thermal Properties of Carbon Nanotubes.	19
2.3.4 Mechanical Properties of Carbon Nanotubes.	20
2.3.5 Carbon Nanotubes Production Methods.....	20
2.3.6 Health Impact of Carbon Nanotubes.	22
2.4 Polymer Carbon Nanotubes Composites.....	26
2.4.1 Functionalisation of carbon nanotubes.	28
2.4.2 Electrical Properties.....	28
2.4.3 Mechanical Properties.....	28
2.5 References.....	30
Chapter 3: Composite Processing & Characterisation Methods.....	36
3.1 Introduction.....	36
3.2 Composites Processing.	36
3.2.1 In Situ Polymerisation.	37
3.2.2 Solution Processing.....	37
3.2.3 Electrospinning Processing.....	39
3.2.3.1 Introduction.....	39
3.2.3.2 Electrospinning process.	40

3.2.3.3 Electrospinning Parameters.....	44
3.2.3.4 Electrospinning Potential Applications.....	48
3.3 Techniques of Characterisation.....	49
3.3.1. Fourier Transform Infrared Spectroscopy (FTIR).	49
3.3.2 Raman Spectrometry.....	50
3.3.3 Thermogravimetric Analysis.....	52
3.3.4 Differential Scanning Calorimetry.....	52
3.3.5 Transmission Electron Microscopy (TEM).	54
3.3.6 Scanning Electronic Microscopy (SEM).	55
3.3.7 Tensile Testing.	56
3.3.8 Atomic Force Microscopy (AFM).	57
3.4 Mechanical Reinforcement of Composites Using Filler.....	60
3.4.1 Rule of Mixtures.	60
3.4.2 -Shear-Lag Theory.	60
3.4.3 Halpin-Tsai Theory.....	63
3.5 Summary.....	64
3.6 References.....	65
Chapter 4: Properties of PMMA Reinforced With Carbon Nanotubes.....	70
4.1 Introduction.....	70
4.2 Background and Motivation.....	70
4.3 Films Preparation.	72
4.4 FTIR Characterisations.	73
4.5 Mechanical Characterisations.	75
4.5 Conclusion.	89
4.6 References.....	89
Chapter 5: Properties of PLLA and Biosteel Reinforced With Carbon Nanotubes.....	92
5.1 Introduction.....	92
5.2 PLLA Composites Studies.....	92
5.2.1 Background and Motivations.	92
5.2.2 Film Preparations.	93
5.2.3 Mechanical Characterisations.	95
5.2.4 Thermal Characterisations.	102
5.2.4.1 Thermogravimetric Analysis.....	102
5.2.4.2 Differential Scanning Calorimetry Analysis.....	104
5.2.5 Conclusion.	106
5.3 Biosteel Composite Studies	108
5.3.1 Introduction.....	108
5.3.2 Film Preparation.....	109
5.3.3 Mechanical Characterisations.	110
5.3.4 Conclusion.	114
5.4 References.....	115
Chapter 6: Properties of PVA Composites Produced by Electrospinning.....	117

6.1 Introduction.....	117
6.2 Background and Motivations.....	117
6.3. PVA Electrospun Film Preparations.....	118
6.4 Mechanical Properties of PVA Electrospun Films prepared using a Stationary Plate Collector.....	122
6.5 Mechanical Properties of PVA Electrospun Films using a Rotating Drum Collector....	126
6.7 Mechanical Properties of PVA Composite Electrospun Nanofibres	140
6.7. Conclusion.	118
6.8 References.....	142
 Chapter 7: Conclusion & Future Work.	 145
7.1 Conclusions.....	145
7.2 Future work.....	148
 Appendix: Publication List.....	 150

List of Tables

Table 2.1: Tensile mechanical properties of spider silks and other materials.....	13
Table 2.2: Summary of the nanotubes structure.....	17
Table 2.3: Summary of carbon nanotubes production techniques.....	25
Table 3.1: Comparison of processing techniques for synthesising polymeric nanofibres.....	39
Table 4.1: IR frequencies of the different compounds of the reacted and unreacted carbon nanotubes.....	75
Table 4.2: Summarisation of the main mechanical results.....	88
Table.5.1: Summary of the mechanical properties of PLLA/CNT composites.....	107
Table 5.2: Summary of the mechanical properties of Biosteel composites.....	115
Table 6.1: Summary of the mechanical results for PVA composites.....	142

List of Figures and Illustrations

Figure 2.1: Classification of Polymers.....	5
Figure 2.2: Schematic of PMMA polymerisation.....	7
Figure 2.3: Synthesis of methacrylic acid.....	8
Figure 2.4: Synthesis of MMA monomers.....	8
Figure 2.5: Schematic structure of Poly (vinyl alcohol).....	9
Figure 2.6: The two common polymerisation schemes for poly (vinyl alcohol).....	10
Figure 2.7: Two Polymerisation schemes for poly (lactic acid).....	11
Figure 2.8: Stereoisomers of lactic acid.....	12
Figure 2.9: Structure of a native major ampullate silk.....	13
Figure 2.10 Diamond (a,) and graphite (b), structure.....	14
Figure 2.11: A C ₆₀ molecule and others fullerenes.....	15
Figure 2.12: Representation of single and multi walled nanotubes.....	16
Figure 2.13: The 2 D graphene sheet along with the (n,m) pairs that specify the chiral vector of the nanotubes.....	16
Figure 2.14: The thermal conductivity as a function of the temperature according.....	19
Figure 2.15: Stress strain curves of individual MWNTs.....	21
Figure 2.16: Schematic of an arc discharge generator.....	23
Figure 2.17: Experimental set up for the production of nanotubes by laser ablation.....	23
Figure 2.18: Schematic of Chemical Vapour Deposition.....	24
Figure 3.1: Schematic of electrospinning set up to produce polymeric nanofibres.....	40
Figure 3.2: Schematic of the electrified jet path and the Taylor cone in the electrospinning process.....	44
Figure 3.3: SEM of electrospun nanofibres from different polymer concentration solutions.....	45
Figure 3.4: Schematic distribution of solvents molecules in high (<i>A</i>) and low (<i>B</i>) polymer viscosity solution.....	45
Figure 3.5: A fast feed rate results in droplet formation on PVA (a) and PLLA (b) electrospun nanofibres.....	47
Figure 3.6: Potential applications for polymer electrospun nanofibres.....	48

Figure 3.7: Energy level diagrams for Stokes Raman scattering and Anti-Stokes Raman scattering.....	50
Figure 3.8: DSC curve showing several transition types.....	53
Figure 3.9: Illustration of the two types of DSC machines.....	53
Figure 3.10: Composites tested using the Zwick tensile tester.....	56
Figure 3.11: Diagram of an AFM set up.....	57
Figure 3.12: SEM image of nanofibres onto SiO ₂ trenches.....	58
Figure 3.13: Schematic of a fixed nanofibre in a lateral test with AFM tip.....	58
Figure 3.14: AFM pictures of the nanofibre before (a) and after lateral bending test (b).....	59
Figure 3.15: Force-displacement curve for a single nanofibre of PVA composite.....	59
Figure 4.1: Drop cast films of PMMA/CNTs composites, a) by solution mixing processing b) by in situ polymerisation processing.....	71
Figure 4.2: Homogenous solid of polymerised PMMA and PMMA/CNTs.....	72
Figure 4.3: Drop-cast PMMA composites films with range of volume fraction of nanotubes from 1.8×10^{-4} to 6×10^{-3}	73
Figure 4.4: FTIR spectra of reacted and unreacted carbon nanotubes.....	74
Figure 4.5: Representative Stress-Strain curves for Composites <i>A</i> for a range of volume of nanotubes.....	76
Figure 4.6: Representative stress-strain curves for Composites <i>B</i> for a range of volume fractions of nanotubes.....	76
Figure 4.7: Strain at break of Composites <i>A</i> and <i>B</i> as a function of volume fraction of carbon nanotubes.....	77
Figure 4.8: Young's Modulus for composites <i>A</i> and <i>B</i> as a function of volume fraction of carbon nanotubes.....	78
Figure 4.9: TEM picture of OH functionalized MWNTs.....	81
Figure 4.10: Ultimate tensile strength and breaking strength for PMMA composites blended with polymerised PMMA and commercial PMMA as a function of volume fraction of carbon nanotubes.....	82
Figure 4.11: SEM picture of Polymer-covered nanotubes bridging a crack in a composite blended with polymerised PMMA.....	85
Figure 4.12: Toughness for PMMA composites blended with polymerised PMMA and commercial PMMA as a function of volume fraction of carbon nanotubes.....	87
Figure 5.1: Drop-casting PLLA LMW composite films with range of volume fraction of OH functionalised MWNTs from 1.8×10^{-4} to 6×10^{-3}	94
Figure 5.2: Synthesis of SWNTs P5.....	94
Figure 5.3: Representative stress-strain curves for PLLA/CNTs composites for a range of volume fractions of nanotubes.....	95
Figure 5.4: Strain at break of PLLA/CNTs composites as a function of volume fraction of carbon nanotubes.....	97

Figure 5.5 Young's Modulus for PLLA/CNTs composites as a function of volume fraction of carbon nanotubes.....	98
Figure 5.6: Ultimate tensile strength for PLLA/CNTs composites as a function of volume fraction of carbon nanotubes.....	99
Figure 5.7: Breaking strength for PLLA/CNTs composites as a function of volume fraction of carbon nanotubes.....	100
Figure 5.8: Toughness for PLLA/CNTs composites as a function of volume fraction of carbon nanotubes.....	102
Figure 5.9: Weight loss versus temperature for PLLA LMW composites and OH-MWNTs and their first derivatives.....	103
Figure 5.10: 1 st and 2 nd heat scan of PLLA LMW composites with 0.006 volume fraction of OH-MWNTs.....	104
Figure 5.11: Glass transition and percentage crystallinity of PLLA LMW composites as a function of volume fraction of carbon nanotubes.....	105
Figure 5.12.: Drop-casting Biosteel composite films with range of volume fractions of P5 functionalised SWNTs from 2.3×10^{-4} to 3.6×10^{-3}	110
Figure 5.13: Representative stress-strain curves for Biosteel composites for a range of volume fractions of nanotubes.....	111
Figure 5.14: Mechanical properties of Biosteel composites for a range of volume fractions of nanotubes.....	112
Figure 6.1: Synthesis of P8-SWNTs.....	118
Figure 6.2: a) Electrospinning set up with a stationary plate collector, b) PVA electrospun film.....	119
Figure 6.3: SEM images of electrospun PVA films prepared using various parameters.....	120
Figure 6.4: Representative Raman spectra of PVA/CNT electrospun membranes.....	121
Figure 6.5: Representative stress-strain curves for PVA/CNT electrospun composites with a range of nanotube volume fractions.....	122
Figure 6.6: Strain at break of PLLA/P8-SWNT electrospun film composites as a function of nanotube volume fraction.....	123
Figure 6.7: Mechanical properties of electrospun PVA films as a function of the nanotube volume fraction.....	124
Figure 6.8: Electrospinning apparatus using a rotation drum collector.....	126
Figure 6.9: SEM pictures of PVA/P8-SWNTs electrospun films for various speed rotation and cross sections of the films at the higher speed rotation.....	128
Figure 6.10: FWHM plotted as a function of the rotation speed.....	129
Figure 6.11: Representative stress-strain curves of PVA/P8-SWNTs bulk and electrospun composites.....	130
Figure 6.12: Mechanical parameters for drop-cast and electrospun composites.....	131
Figure 6.13: The density of the electrospun films as a function of the rotation speed of the drum.....	132
Figure 6.14: Average diameters of PVA and composites electrospun composite.....	133
Figure 6.15: Force-displacement curve for a single nanofibre of PVA composite.....	134

Figure 6.16: Schematic of model used to calculate the mechanical properties of a single electrospun nanofibre.....	134
Figure 6.17: Mechanical parameters for single electrospun nanofibres.....	136
Figure 6.18: a) 1 st and 2 nd heat scan of PVA electrospun and drop cast film composites with 0.43 vol% of P8-SWNTs, b) Crystallinity, χ , as a function of the volume fraction of carbon nanotubes of electrospun composites films.....	138

Abstract

Three biopolymers; poly(methyl methacrylate) (PMMA); poly(L-lactic acid) (PLLA); poly(vinyl alcohol) (PVA) and an engineered spider silk (Biosteel®) have been independently doped with carbon nanotubes. PMMA was functionalised with OH-functionalised multi-walled carbon nanotubes (OH-MWNTs) by in situ polymerisation. Infrared absorbance studies revealed covalent bonding between the polymer strands and the nanotubes. The treated nanotubes were blended in solution with both in-house synthesised PMMA and commercial PMMA before drop-casting to form composite films. For composites blended with in-house synthesised PMMA, increases in the Young's modulus (Y), breaking strength (σ_B), ultimate tensile strength (σ_C), and toughness (T) of $\times 1.9$, $\times 4.7$, $\times 4.6$, and $\times 13.7$ respectively were observed upon the addition of less than 0.5 wt% nanotubes. For commercial PMMA, the increases in the above mentioned mechanical parameters were $\times 1.2$, $\times 1.5$, $\times 1.5$, and $\times 3$ respectively. In both cases, effective reinforcement was only observed for nanotube contents of up to ~ 0.1 vol %. Above this volume fraction, all mechanical parameters tended to reduce, probably as a result of nanotube aggregation. In addition, scanning electron microscopy (SEM) studies of the composite fracture surfaces after film breakage showed that a polymer layer coated the nanotubes. The fact that the polymer rather than the interface fails suggests that functionalisation results in an extremely high polymer/nanotube interfacial shear strength.

Composites films were formed by solution mixing and drop cast processing using low and high molecular weight PLLA and both OH-MWNTs and single walled nanotubes functionalised with octadecylamine (P5-SWNTs). The best mechanical reinforcement was achieved with low molecular weight PLLA and OH-MWNTs. The investigated mechanical parameters (Y , σ_C , σ_B , and T) showed increases of $\times 1.4$, $\times 1.4$, $\times 1.4$, $\times 3$ and $\times 3.8$ respectively. Thermal analysis has shown that nanotubes do not have an effect on the thermal degradation of the degradation of the samples. Moreover, the glass transition and the percentage crystallinity do not undergo dramatic changes by the addition of CNTs.

Nanotube-silk composites were prepared by mixing functionalised nanotubes and Biosteel in 1,1,1,3,3,3-Hexafluoro-2-propanol. Composite films were then produced by drop-casting techniques. The mechanical properties of the pure Biosteel films were lower than expected due

to the effect of the strong denaturing solvent. Increases in stiffness, strength, ductility and toughness were observed at very low nanotube loading levels. Analysis of the rate of increase of stiffness as a function of volume fraction showed extremely good polymer-nanotube stress transfer. However, all mechanical results saturated at a volume fraction of $\sim 0.1\%$ as a result of nanotube aggregation.

PVA nanofibre composite films were produced using electrospinning techniques by adding m-poly (aminobenzene sulfonic acid) functionalised SWNTs (P8-SWNTs). Raman spectroscopy was carried out, demonstrating that good nanotube dispersions were achieved in all electrospun PVA films for a range of P8-SWNT volume fractions. Mechanical measurements were performed on these composites, revealing a linear increase in all of the mechanical parameters investigated, (Y , σ_C , σ_B , and T), up to a maximum of 0.43 vol% of nanotubes. Above this concentration, all mechanical properties decreased, suggesting nanotube aggregation. The average density and porosity of these membranes was calculated to be 205 kg/m^3 and 84% respectively. At the optimum nanotube loading level, electrospun composite membranes displayed a toughness of 15.56 J/g . DSC analysis showed a linear increase in the crystallinity up to 0.2 vol% of nanotubes. DSC also established an increase in the crystallinity in this polymeric system, due to the electrospinning technique. A study was also carried out using a rotating drum collector to produce electrospun PVA membranes with 0.43 vol% nanotubes for various rotation speeds. Effective alignment of nanofibres as a result of increasing the rotation speed was demonstrated using Fast Fourier Transform analysis and SEM characterisation. Electrospun composite membranes obtained at the high rotation speeds displayed a Young's modulus and strength values that were within the same range as for the drop cast films produced from the same solution, but with a density that was 5 times lower.

Chapter 1. Introduction.

1.1 Background and Motivation.

Polymers have been a part of life since the beginning of humankind. Natural polymers include tar, shellac, tortoise shell, horns and tree saps that produce amber and latex. These polymers were processed with heat and pressure into articles such as hair ornaments and jewellery. Natural polymers began to be chemically modified during the 1800s to produce many materials. The most famous of these were vulcanised rubber, gun cotton and celluloid. It was only at the beginning of the 20th century that synthetic polymer started to be produced (Bakelite). Since then, the polymer industry has grown and has become a crucial part of our every day life, providing materials for construction, commerce, transportation and entertainment across the globe. Estimates of global polymer production ranges from 350 billion euros to more than 570 billion euros. This represents an annual production of 114-181 billion kg [1].

In general, polymeric materials are not chemically or molecularly homogenous but are multicomponent systems. Adding fillers such as minerals, ceramics, metals or even air can generate an infinite variety of materials with unique physical properties and competitive production costs. In the late 1980s, a new type of polymer filler known as nanoparticles (spheres, rods, plates) generated a lot of interest within the academic and industrial community. This new class of material known as “polymer nanocomposites” not only improve the performance of traditional filled polymers but introduce completely new combinations of properties which enable new applications for polymers. For example, low volume additions (1-5%) of nanoparticles such as layered silicates provide property enhancements that are comparable to those achieved by conventional loading (15-40%) of traditional fillers [1]. The lower loadings facilitate processing and reduce component weight. Moreover, new composite properties which were not possible with traditional fillers are now available such as reduced permeability, optical clarity, self-passivation and increased resistance to oxidation and ablation. These features have been successfully used commercially for example for automotive parts, coatings or flame retardants. Recent Market surveys have estimated global consumption

of polymer nanocomposites at 170 million euros with an average potential growth rate at 24% [2, 3].

Polymer nanocomposites have attracted a lot of interest in the medical field as biomaterials. These composites can be defined as a non-drug substance suitable for inclusion in systems which augment or replace the function of bodily tissues or organs. When the class of material is placed in contact with a biological system, three types of interactions can be classified. A biomaterial is biocompatible which means it has the ability to elicit an appropriate host response in a specific application. Biomaterial can be bio-inert, bio-active or bio-resorbable. The term bio-inert refers to any material that once placed in a biological system has minimal interaction with its surrounding. By opposition, bio-active refers to any material that interacts with its living surrounding where it was placed. Bio-resorbable refers to a material that upon placement within a biological system starts to dissolve (resorbed) and slowly replaced by a biological structure. Polymer nanocomposites can be produced from synthetic polymer, natural polymer or biopolymers. A biopolymer is a macromolecule produced by living organism such as proteins and nucleic acid. They are used in biomedical technologies such as tissues engineering, bone replacement/repair, dental applications and controlled drug delivery. Adding nanofillers to polymers could dramatically improve the existing applications of polymers in the biomedical area. For example, hydroxyapatite polymer nanocomposites have been used as biocompatible and osteoconductive substitutes for bone repair and implantation [4, 5]. Aliphatic polyester has also been used with nanoclays to produce strong composites for high load bearing applications[6].

Recently, a great deal of attention has been focussed on one type of nanofiller in the field of polymer nanocomposites. Since their discovery in 1991[7], carbon nanotubes appear to be one of the most promising fillers for various polymer applications. This is because they have crucial characteristics which have not been displayed by any previous material. They possess outstanding mechanical, thermal and electrical properties [8]. In addition they display nanoscopic morphology and high aspect ratio. Therefore, they are expected to play a major role in the polymer industry and more particularly in a biomedical sector as great fillers for bio materials.

1.2 Thesis Outline.

The aim of this thesis was to produce a new class of composites for potential medical applications such as scaffolds for tissue engineering. Several types of polymers and biopolymers were investigated to produce composites reinforced with carbon nanotubes. The choices of the polymers host were based on their abilities to be used a biomaterial. The main focus of this work was to assess the optimum loading level of carbon nanotubes required to improve the mechanical properties of the pristine matrices. In order to make these polymers carbon nanotubes composites, two methods of productions were chosen. The first method was based on solution mixing followed by drop cast processing to make thin films composites. The second method also involved solutions mixing and electrospinning processing to produce porous nanofibres composites.

Chapter 2 addresses a succinct overview of the polymers used in this work. These are Poly (methyl methacrylate), Poly (L-lactic acid) and Poly (vinyl alcohol). This chapter also presents a general description of the properties of carbon nanotubes followed by a relevant discussion of polymer / carbon nanotube composites.

Chapter 3 discusses the methods used to produce our polymer composites followed by a more exhaustive presentation of electrospinning processing. In addition, a description of the techniques of characterisation carried out in this thesis is also presented. Finally, this chapter concentrates on relevant theoretical models of mechanical reinforcement for polymer / carbon nanotube composites.

Chapter 4 presents the study on Poly (methyl methacrylate) / carbon nanotube composites. This includes a presentation of production methods of these composites achieved by in situ polymerisation and drop cast processing. In addition, the mechanical properties of these materials are presented. From these results and using SEM, models are also addressed to understand the effective mechanical reinforcements observed from these polymer composites.

Chapter 5 describes firstly the preparation of two grades of Poly (L-lactic acid) polymers reinforced with two batches of carbon nanotubes. This is then followed by the mechanical and

thermal characterisation. The second part of the chapter presents a brief study on composites of a commercial spider silk (Biosteel®) reinforced with carbon nanotubes. This work mainly focuses on the mechanical properties of these materials.

Chapter 6 introduces the production and the characterisation of Poly (vinyl alcohol) nanofibre films reinforced with carbon nanotubes by electrospinning processing. After a brief presentation of the optimum parameters used to obtain these nanofibre composite films, their mechanical properties are addressed. Finally mechanical properties of single nanofibre composites investigated by AFM technique are presented. A model is also discussed to explain the mechanical reinforcement observed.

Chapter 7 concludes with a summary of the main results from the various studies performed in this thesis. A concise discussion from these results on possible future work is then presented.

1.3 References.

1. Winey, K.I. and R.A. Vaia, Polymer nanocomposites. *Mrs Bulletin*, 2007. 32(4): p. 314-319.
2. McWilliams, A., Nanocomposites, Nanoparticles, Nanoclays, Nanotubes. NANO21C, BCC Research, Norwalk, CT, 2006.
3. Thayer, A.M., *Chem. Eng. News*, 2000. 78(36): p. 16.
4. Uchida, A., et al., The use of calcium hydroxyapatite ceramic in bone tumour surgery. *J Bone Joint Surg Br*, 1990. 72-B(2): p. 298-302.
5. Cooke, F.W., *Ceramics in Orthopedic-Surgery. Clinical Orthopaedics and Related Research*, 1992(276): p. 135-146.
6. Krikorian, V. and D.J. Pochan, Poly (L-lactic acid)/layered silicate nanocomposite: Fabrication, characterization, and properties. *Chemistry of Materials*, 2003. 15(22): p. 4317-4324.
7. Iijima, S., Helical microtubules of graphitic carbon. 1991. 354(6348): p. 56-58.
8. Baughman, R.H., A.A. Zakhidov, and W.A. de Heer, Carbon nanotubes - the route toward applications. *Science*, 2002. 297(5582): p. 787-792.

Chapter 2: Materials & Background.

2.1 Introduction.

This chapter will introduce the main properties of materials used in this research, namely polymers and carbon nanotubes. A brief overview of polymers is presented with particular emphasis on the polymer matrices used in this project. The physical and chemical properties of carbon nanotubes are also discussed.

2.2 Polymers.

2.2.1 Introduction to Polymers.

A polymer can be defined as a large molecule constructed from many smaller structural units, called monomers, covalently bonded together in any conceivable pattern. To qualify as a monomer, a molecule must possess two or more reactive sites, through which they can be linked to form a polymer chain. The number of bonding sites is referred to as the “functionality” of the monomer. Bonding sites may consist of a reactive functional group such as amino groups ($-\text{NH}_2$). Alternatively, they may consist of double bonds which react under suitable conditions to provide the covalent linkage between repeating units. Such strong linkages form the backbone of the polymer chains. Polymers can be classified in two main categories; the natural and the synthetic polymers. These categories can subsequently be divided into sub-groups as shown in Figure 2.1.

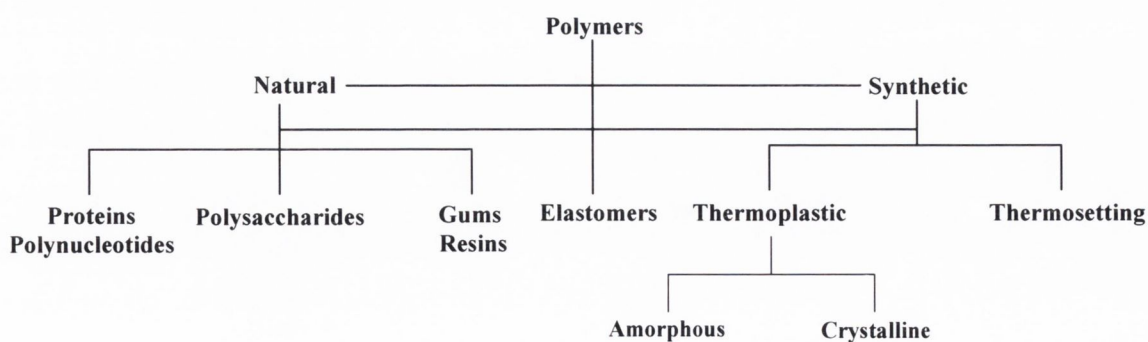


Figure 2.1: Classification of Polymers.

Furthermore, polymers are also classified as amorphous or crystalline, depending on the degree of order amongst the polymer chains. The properties of polymer depend on their physical structure. This includes branching, tacticity, chain flexibility, steric effect and crosslinking. These parameters will affect the glass transition and melts temperature. Chemical properties such as the type and polarity of the side groups also influence the polymer properties. Side groups will affect molecular interactions within the polymer, and therefore influence melting point and strength. Types of interactions include dipole-dipole and Van der Waals which are generally weaker

The two main techniques used to produce synthetic polymers are condensation and the addition polymerisation. In the case of condensation polymerisation, monomers have at least two functional groups such as alcohol, amine or carboxylic acid group. During the condensation reaction, two different monomer structures react to form a dimer with the release of a small molecule such as H_2O . This reaction propagates a number of times to obtain a long polymer chain. Some common polymers synthesised by this method are polyamides (carboxylic acid + amine) and polyesters (carboxylic acid + alcohol). However, not all condensation reactions involve the liberation of small molecules. For example, active hydrogen is transferred from one molecule to the next during polyurethane synthesis (dialcohol + diisocyanate). Addition polymerisation involves monomers containing carbon to carbon double and triple bond. In these monomers unsaturated carbon bonds can be broken resulting in "chain polymerisation" where numerous monomers link together. There are three steps in addition reaction; initiation, propagation and termination. During initiation, an initiator molecule which can be either a free radical, an anionic or cationic initiator activates a monomer by opening an unsaturated carbon bond. In the propagation phase, the newly formed radical reacts with the active double bond of another monomer molecule. This sequence is repeated to form a long polymer chain. Termination occurs either when all monomers have been consumed or when two active chain ends bond together. Polymerisation can also be terminated by the reaction of an active chain with an initiator, an impurity or an inhibitor. Polymers such as polyethylene, polypropylene and polyvinyl chloride are synthesised by this method.

Advantages of polymers include low cost, simple synthesis and processability. Polymers are low density materials. They can easily be molded into complex shape, which are

strong and relatively inert. The main techniques for polymer processing are injection molding, compression molding, transfer molding, blow molding and extrusion. Polymers exhibit properties that are attractive for many applications such as clothing, food packaging, medical devices and aircrafts. Natural polymers such as silks, collagen and agarose have found usage in many tissue engineering applications.

Three different thermoplastic polymers will be presented in thesis, namely Poly (methyl methacrylate) (PMMA), Poly (vinyl alcohol) (PVA) and Poly (L lactic acid) (PLLA). These materials are capable of changing shape on the application of a force and retaining this shape on removal of this force. Also, they will soften when heated above the glass transition and it is a totally reversible and repeatable process. One other feature of these polymers is that they can be considered as biocompatible, i.e. the ability of having a none toxic response or injurious effect on biological systems.

2.2.2 Poly (methyl methacrylate).

PMMA was first developed in 1928 in various laboratories and become commercially available in 1933. Since then PMMA has been used in many applications in the automobile industry, building and lightening industry and other applications including CD production, pens, furniture and electronics. PMMA is also used as a biomaterial because of its compatibility with human tissue. Its transparency makes PMMA suitable for hard contact lenses and intraocular lense replacements to treat cataracts. Thanks to its mechanical properties, this polymer is also used as a cement to affix implants or to remodel damaged bones.

The synthetic polymerisation of PMMA can be achieved either by radical polymerisation or anionic polymerisation (fig: 2.2).

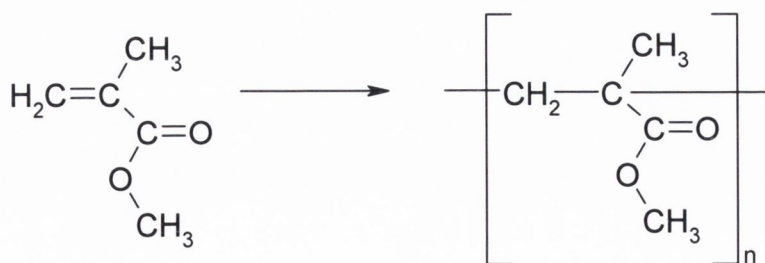


Figure 2.2: Schematic of PMMA polymerisation.

The monomer methyl methacrylate can be synthesised by the reaction of the cyanhydric acid with acetone. The resulting salt then undergoes then under an esterification with methanol to form MMA. An alternative method is the oxidation of isobutene followed by reaction with water to produce methacrylic acid (fig: 2.3).

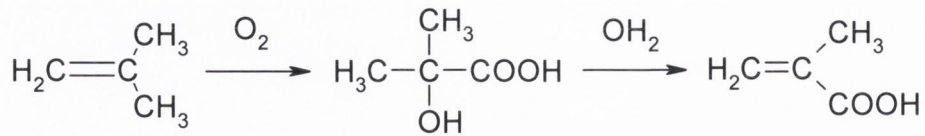


Figure 2.3: Synthesis of methacrylic acid.

Afterwards, the methacrylic acid undergoes an esterification with methanol to form the MMA monomer (fig: 2.4).

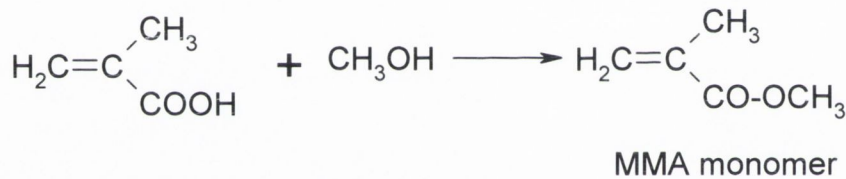


Figure 2.4: Synthesis of MMA monomers.

PMMA is usually atactic. The substituent group (CO-OCH₃) is randomly located along polymer macromolecules. PMMA is defined as totally amorphous. This also explains the transparency of PMMA. However, PMMA can have a syndiotactic arrangement in some cases. The transmission coefficient of PMMA is higher than mineral glass and between 3600 and 100nm (UV) very little electromagnetic radiation is absorbed. Unfortunately, PMMA can be easily scratched which limits its application in precision optics. The glass transition (T_g) will vary according to the tacticity of the polymer. Atactic PMMA have a T_g around 65°C and syndiotactic PMMA has a T_g at 140°C. Commercial PMMA usually has a T_g around 105°C.

Two types of PMMA will be investigated in this thesis. The first one was purchased from Aldrich (M_w ~ 50000 mol/g). The second PMMA was produced by radical polymerisation in our laboratory using the free radical initiator Azobisisobutyronitrile 2,2 (AIBN).

2.2.3 Poly(vinyl alcohol).

The first successful preparation of PVA was achieved by Herman and Haehnel in 1924 [1]. It became commercially available in the 1950's by Dupont®. Since its discovery, Poly (vinyl alcohol) has attracted intense interests due to its properties. Initially PVA was mainly used in the textile industry. However, due to excellent film forming, emulsifying and adhesive properties, this polymer has been exploited in numerous applications. For example, PVA is used in hairsprays, shampoo glues latex paints and as an adhesive and a thickener material in paper coatings. Some other applications include building reinforcement and packaging materials. More recently, PVA has been investigated for biomedical applications as it is nontoxic, non carcinogenic and shows good biocompatibility. As a results PVA is now used as hydrogel for soft contact lens materials, artificial skin and cartilage replacement and vocal cord reconstruction [2-4].

PVA is an organic polymer with a carbon backbone and hydroxyl side groups as seen in Figure 2.5.

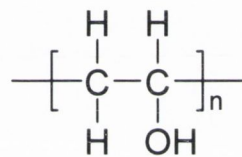
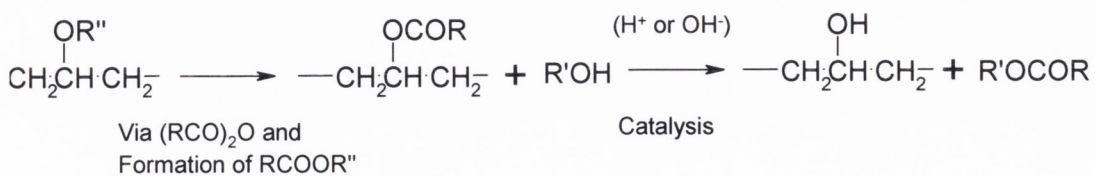


Figure 2.5: Schematic structure of Poly (vinyl alcohol).

Unlike many vinyl polymers, PVA is not polymerised from its monomer which is a tautomeric form of acetaldehyde. Instead of being produced by direct addition or condensation polymerisation, PVA is synthesised by the hydrolysis of Poly (vinyl acetate). This can be achieved in a number of ways as shown in Figure 2.6 [5].



Or else

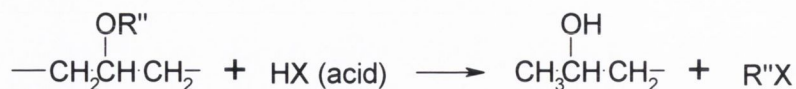


Figure 2.6: The two common polymerisation schemes for poly (vinyl alcohol)

In general, these reactions do not go to completion. Therefore commercial PVA will contain various amounts of residual acetate groups. Many studies have been carried out to determinate the effects of this on the properties of PVA [5]. It has been reported that less than 0.5% of residual acetate groups can be detrimental to the tensile strength of the polymer [6].

The molecular weight distribution of PVA can be controlled either by the preparation method or, by fractionation and selection [5]. The range of molecular weights can goes from a few thousand up to about a million g/mol. The degree of hydrolysis, which quantifies the number of hydroxyl groups present in the polymer chain, is an important factor which influences physical characteristics such as solubility, viscosity, strength and crystallinity. Also, the majorities of commercially available grades of PVA are atactic and contain significant portions of syndiotactic diads. The crystallinity should be therefore poor. However, it has been reported that 70% crystallinity was achieved by annealing common atactic PVA [7]. This can be explained by the relatively small size of hydroxyl groups, which enables the polymer to assume both L- or D- stereoisomer in an atactic chain within a single crystal lattice. The thermal properties also change according to crystallinity and the degree of hydrolysis. A fully hydrolysed PVA will have a peak of melting around 230°C, this decreases to 180-190°C for partially hydrolysed grades. The glass transition temperature is in the region of 85°C.

In this work, polyvinyl alcohol was purchased from Sigma Aldrich (Product code: 9002-89-5) with a molecular weight ranging from 30,000 to 70,000 g/mol and a degree of hydrolysis at 98%.

2.2.4 Poly (lactic Acid).

Poly (lactic acid) (also known as poly lactide acid) was first discovered by Carothers in 1932 [8]. PLA is a linear thermoplastic aliphatic polyester derived from 100% renewable

resources, such as corn, and the polymer is compostable [9, 10]. These features make PLA very attractive for industry since many common used polymers are petroleum based. Biopolymers are becoming increasingly desirable due to the drastic reduction in fossil fuel reserves. Moreover the production of lactic acid, which is necessary for the polymerisation, can be obtained from the formation of glucose. One of the most abundant sources of sugar is dextrose, which can be extracted from corn. Materials such as grass and even biomass can also be used to produce lactic acid.

The production of PLA can be achieved via two methods, as shown in Figure 2.7. Using the first method, polymerisation is realised by direct condensation of lactic acid and the removal of water with the use of solvent under high vacuum and temperature (fig: 2.7 (1)). Only low molecular weight polymers can be produced because of difficulties associated removing with water and impurities. Using the second method, polymerisation occurs via the cyclic intermediate dimer (lactide), through a ring opening process [10]. Here the water is removed under milder conditions without solvent to produce the lactide. The ring opening polymerisation is accomplished under heat without solvent treatment (fig: 2.7 (2)). By controlling the purity of the dimer, it is possible to produce a wide range of molecular weights.

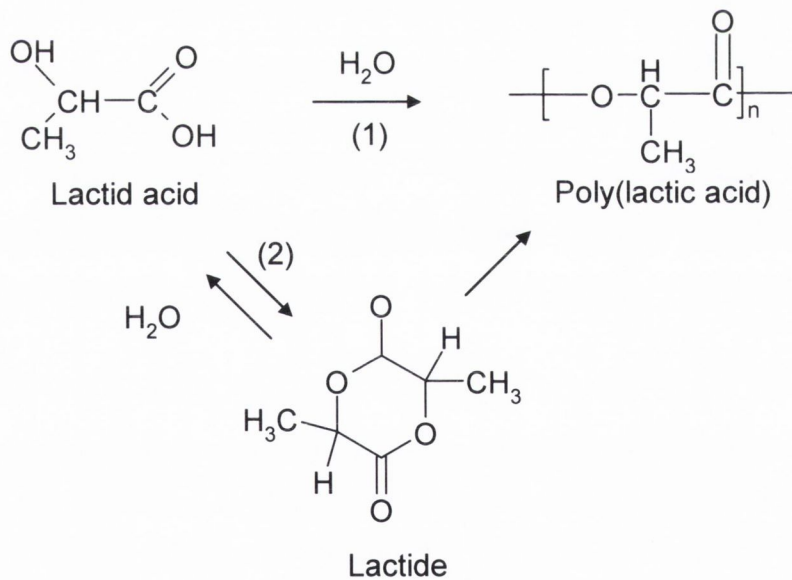


Figure 2.7: Two Polymerisation schemes for poly (lactic acid)

The production of the lactic acid from sugar fermentation results in the formation of chiral molecules. Lactic acid can exist as the L- or D- stereoisomer (fig: 2.8). Chemically synthesised, lactic acid gives racemic mixtures (50% D and 50% L). However fermentation is very specific, allowing the production of essentially one major stereoisomer. Therefore the production of cyclic lactide dimer results in three potential polymer forms: poly (L- lactic acid) (PLLA), poly (D- lactic acid) (PDLA) and poly (L, D- lactic acid) (PDLLA). The properties will vary according to the type of PLA formed. As an example, PLLA and PDLA are semi crystalline polymers with a glass transition temperature typically between 55-65°C and a melting temperature around 160-170°C. On a contrary PDLLA is totally amorphous.

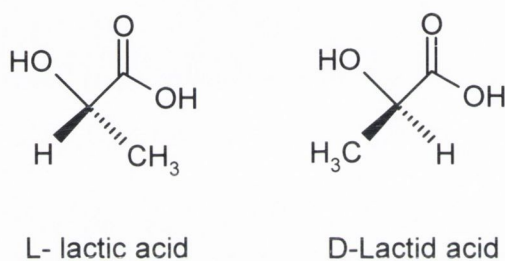


Figure 2.8: Stereoisomers of lactic acid.

Due to availability and production costs, the initial uses of PLA were for biomedical applications such as sutures [11] and drug delivery systems [12]. However PLA is now found in numerous industries. For example, this polymer is a promising alternative to poly(ethylene terephthalate which) is widely used in food packaging. Poly (lactic acid) also has many potential uses in fibres and non-woven L- or D- stereoisomer materials. It is easily converted into a variety of fibre forms using conventional melt-spinning processes. Major applications for PLA fibres and non-wovens materials include clothing and furnishings such as drapes, upholstery and covers. Some potential applications include household and industrial wipes, diapers, feminine hygiene products, disposable garments, and UV resistant fabrics for exterior use (awnings, ground cover, etc.) [13].

2.2.5 Biosteel ®.

Spider silks are protein-based biopolymer filaments or treads secreted by specialized epithelial cells as concentrated soluble precursors of highly repetitive primary sequences. This

biomaterial is one of the most impressive products made by a living organism. Spider silks display some outstanding mechanical properties as seen in Table 2.1.

Material	Stiffness (GPa)	Strength (GPa)	Extensibility	Toughness (MJm ⁻³)
Areneus MA silk	10	1.1	0.27	160
Areneus Viscid silk	0.003	0.5	2.7	150
Bombyx silk	7	0.6	0.18	70
Tendon collagen	1.5	0.15	0.12	7.5
Bone	20	0.16	0.03	4
Wool, 100% RH	0.5	0.2	0.5	60
Elastin	0.001	0.002	1.5	2
Resilin	0.002	0.003	1.9	4
Synthetic rubber	0.001	0.05	8.5	100
Nylon fibre	5	0.95	0.18	80
Kevlar 49 fibre	130	3.6	0.027	50
Carbon fibre	300	4	0.013	25
High-tensile steel	200	1.5	0.008	6

Table 2.1: Tensile mechanical properties of spider silks and other materials [14].

These properties are the result of a complex structure. For example, the silk polymer network synthesised from the major ampullate silk gland (MA) is a combination of amorphous chains of amino acid and β sheet crystal (fig 2.9)

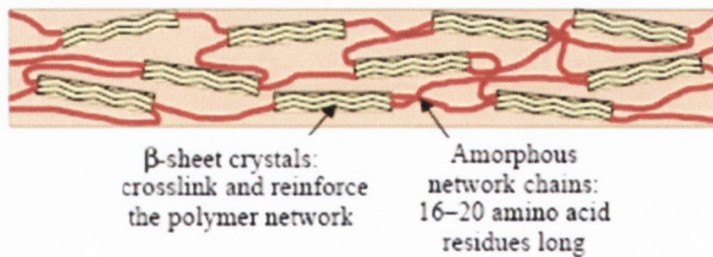


Figure 2.9: Structure of a native major ampullate silk [14].

However, the use of this material is limited by the difficulty to domesticate and therefore to control the fabrication of spider silk. This issue was recently addressed by the commercialisation of the product known as Biosteel. This new class of biopolymer is developed by Nexia Biothechnologies since 2002. Its production is achieved by expressing the dragline silk genes of two spider species in goat cells silk [15]. Dragline silk, made by the MA gland, is used as a safety line and as a the frame thread of the spider's orb.

2.3 Carbon Nanotubes.

2.3.1 Physical Properties of Carbon Nanotubes.

Carbon is the sixth most abundant element in the world. It occurs in all organic life and is the basis of organic chemistry. Due to its electronic configuration, $1s^2 2s^2 2p^2$, three types of hybridisation can occur, namely sp , sp^2 and sp^3 . This property allows carbon atoms to bond with each other and a wide variety of other elements forming nearly ten million known compounds. There are three isotopes of carbon: C_{12} (98.89%), C_{13} (1.11 %) and trace amounts C_{14} .

Until the 1980's, only two allotropic crystalline forms of carbons were known (fig: 2.10). The first structure is diamond and it consists of sp^3 hybridisation between four carbon atoms. The distance between each atom is 1.56 \AA . With a density of 3.52 g/cm^3 diamond is the hardest materials known. This is due to the 3d interlocking covalent bonds. Moreover, the absence of delocalised electrons makes diamond a poor electrical conductor (10^{-11} S/m) [16]. Graphite, the second allotrope, is based on sp^2 hybridisation between three carbon atoms. This involves the formation of a planar sheet structure with a C-C sp^2 bond length of 1.42 \AA . The overlapping of unhybridised P_z orbitals results in weak Van der Waals interactions between adjacent graphite layers. Therefore, graphite is a soft material. The inter-layer separation distance is 3.35 \AA . Also, P_z electrons are delocalised across the carbon sheets which enables it to conduct electricity. In plane graphite conductivity was measured to be 10^5 S/m [17]

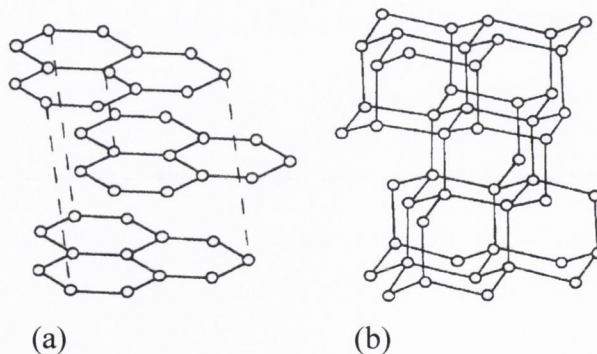


Figure 2.10: Diamond (a,) and graphite (b), structure.

A new allotrope of carbon was discovered in 1985 by Kroto, Curl and Smalley [18]. In 1996 this work was awarded the Nobel Prize in Chemistry. This structure called the Buckminsterfullerene (Bucky ball or C_{60}), consists of a spherical molecule with 60 carbons

atoms arranged into 20 hexagons and 12 pentagons. This geometry satisfies Euler's law which states that with 12 pentagons and any number of hexagons it is possible to construct a polyhedron. Twelve is the minimum number of pentagons required to give sufficient positive curvature to close this architecture into a sphere. The discovery of C_{60} had a huge impact in the field of both chemistry and physics research [19, 20]. Krätsmer and Huffman [21] dramatically improved the production method of fullerenes. Their technique is based on an arc discharge method where graphite is vaporized in an atmosphere of helium. With this work, C_{70} (molecule made of 70 atoms of carbons) was produced. Subsequently, more molecules were discovered such as C_{76} , C_{80} and C_{84} . By adding extra hexagons, these molecules begin to elongate and start to lose their spherical shape adopting a more cylindrical form (fig 2.11).

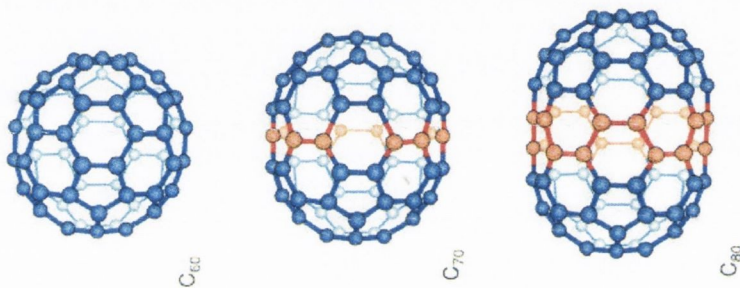
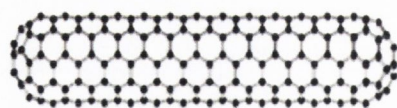
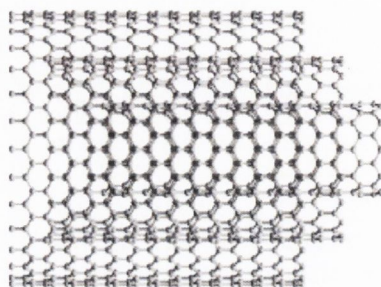


Figure 2.11: A C_{60} molecule and others fullerenes.

Extensive research, using the arc discharges method, has led to the breakthrough of multi-walled carbon nanotubes (MWNTs) by Iijima et al in 1991 in the scientific community [22]. A couple of years later, single-walled nanotubes (SWNTs) were discovered [23, 24]. However, carbon nanotubes have been produced and observed under a variety of conditions prior to 1991. In 1952, Radushkevich et al. published clear images of 50 nanometre diameter made of carbon [25]. Using a vapour-growth technique, Oberlin et al. published in 1976 hollow carbon fibres with diameters in the nanometre range [26]. SWNTs can be described as a single graphene sheet rolled up into a cylinder and capped at either end by a fullerene hemisphere. Therefore, a perfect nanotube will be made of millions of hexagons with only twelve pentagons. The diameter is usually less than 2nm. MWNTs are composed of concentric sets of SWNTs with an inter-shell spacing of 0.34 nm. Depending on the number of shells present, MWNTs can have a diameter range from 2 to 100nm. Typically, carbon nanotubes are microns long, but tubes up to 4cm long have been reported [27]. As a result, carbon nanotubes possess a very large aspect ratio and can be approximated to one-dimensional structures. The structures of SWNTs and MWNTs are represented in Figure 2.12.



a) Single-walled nanotubes



b) Multi-walled nanotubes

Figure 2.12: Representation of single and multi walled nanotubes [28].

Several structures are possible for SWNTs by rolling up the hexagonal lattice of carbon at different angles. This property is known as the chirality or helicity of a carbon nanotube. Based on this rolling angle, three types of nanotubes are possible: armchair, zigzag or chiral. In the armchair structure, two C-C bonds on opposite sides of each hexagon are perpendicular to the tube axis (fig: 2.13). In the zigzag arrangement, these bonds are parallel to the tube axis. For all the others conformation, where the C-C bonds lie at an angle to the tube axis, nanotubes will have a chiral structures. MWNTs can be a combination of each structure because it can have several shells, i.e., which can be armchair, zigzag or chiral.

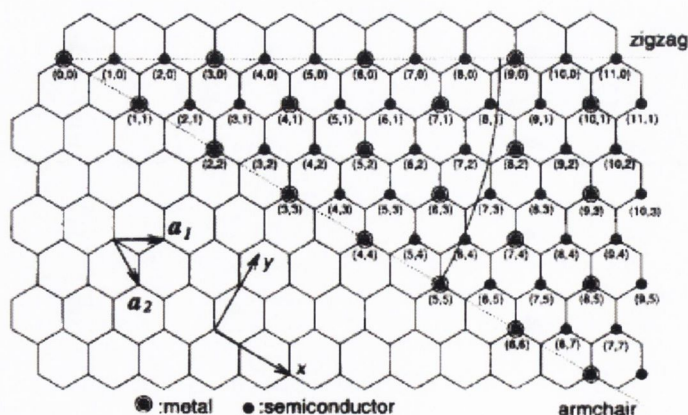


Figure 2.13: The 2 D graphene sheet along with the (n,m) pairs that specify the chiral vector of the nanotubes.

The chirality of nanotubes can be defined mathematically in terms of chiral vectors by the following equation $\vec{C}_h = m\vec{a}_1 + n\vec{a}_2$ and an angle θ . In this case, a_1 a_2 are the unit vectors in the two dimensional hexagonal lattice and m and n are integer units ($0 \leq n \leq m$). If $\theta = 0$ and $n = m$, the nanotubes will have an armchair structure. When $n = 0$, zigzag nanotubes will be formed. In all other cases, nanotubes will be chiral with a finite wrapping angle θ , where $0^\circ \leq \theta \leq 30^\circ$. The diameter of the nanotubes can also be expressed by the following equation (2.1):

$$d = \frac{|\vec{C}_h|}{\pi} = \frac{a(m^2 + mn + n^2)^{1/2}}{\pi} \quad \text{Equation: 2.1}$$

Where a corresponds to the lattice constant in the graphene ($a = \sqrt{3}a_{cc}$), a_{cc} corresponds the nearest neighbour C-C distance, 1.42 Å [29]. The chiral angle θ can also be defined by the following equation (2.2):

$$\theta = \arctan\left(\frac{n\sqrt{3}}{2m+n}\right) \quad \text{Equation: 2.2}$$

All data relative to the nanotube structure is summarised in the table 2.2 below.

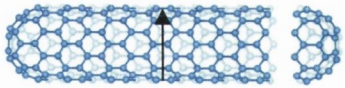
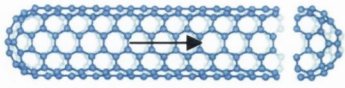
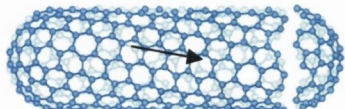
Structure	Integer	Angle of chirality	Diameter	Example
zigzag	$(0,m)$ $n = 0$ or $m = 0$	$\theta = 0^\circ$	$d = a_{cc} \frac{\sqrt{3} m}{\pi}$	 $(0,9) \Rightarrow d = 7,0 \text{ \AA}$
armchair	(n,n) $n = m$	$\theta = 30^\circ$	$d = a_{cc} \frac{\sqrt{3} m}{\pi}$	 $(5,5) \Rightarrow d = 6,8 \text{ \AA}$
chiral	(n,m) $n \neq m$	$0 < \theta < 30^\circ$ $\theta = \text{Arctan}\left(\frac{n\sqrt{3}}{2m+n}\right)$	$d = a_{cc} \frac{\sqrt{3(n^2 + nm + m^2)}}{\pi}$	 $(10,5) \Rightarrow d = 10,4 \text{ \AA} ; \theta = 11^\circ$

Table 2.2: Summary of the nanotubes structure [30].

2.3.2 Electronic Properties of Carbon Nanotubes.

SWNTs can either be metallic or semiconducting. Their electronic conductivity has been predicted to depend sensitively on their tube diameter and the wrapping angle[29, 31-33]. In other words, the electronics properties of SWNTs will depend on their tube indices (n,m). A slight change in these parameters can cause a shift from metallic to semiconductor behaviour. Three configurations can be described:

1 - If $n = m$, which correspond to the armchair structure, nanotubes have bands crossing at the Fermi level and therefore are metallic. In other word, they have a zero band gap.

2 - Zigzag and Chiral tubes will also show metallic behaviour if,

$$\frac{(m - n)}{3} = l \quad \text{Equation: 2.3}$$

where l is an integer.

3 - Nanotubes can be semiconducting with an energy gap of the order $\sim 0.5\text{eV}$ [29]. In this case, this energy gap can be directly related to the diameter of the tube by the following equation 2.4:

$$E_{gap} = \frac{2\gamma_0 a_{C-C}}{d} \quad \text{Equation: 2.4}$$

Where a C-C is equal to 1.42 \AA , d is the diameter and γ_0 is the C-C tight binding overlap energy. Experimentally, γ_0 , the overlap energy was estimated be 2.7 eV . This value was calculated for a SWNT using Scanning Tunnelling Microscopy (STM) [29]. This is close to the theoretical value which was calculated as 2.5eV for a single graphene sheet [34, 35].

For MWNTs, each adjacent shell can have a different chirality. Therefore, concentric shells could have both metallic and semi conducting electronics properties. Similarly to SWNTs, these properties can also be defined according to equation 2.3. At room temperature, the thermal energy exceeds the band gap energy for nanotubes with diameter greater than 14 nm . Therefore, all MWNTs above this diameter will behave as metals or as semi metal materials.

Nanotubes can be considered as one dimensional object because of their aspect ratio. This allows charge carriers to travel through nanotubes without scattering. Hence ballistic transport is possible. This enables nanotubes to carry very large current densities of up to 10^9 A/cm², which is the highest known value for any material [36]. It is also approximately 1000 times the current carrying capacity of copper [37]. In addition, a carrier mobility of 10^5 cm²/Vs has been measured in semi-conducting nanotubes [38]. These properties make CNTs desirable to be used as electrical components. Several researchers have also observed superconductivity in SWNTs at very low temperatures (~1K). A group in Hong Kong has even reported that SWNTs (a = 4Å) embedded in zeolite matrixes were superconducting below 20 Kelvin [39].

2.3.3 Thermal Properties of Carbon Nanotubes.

Diamond and graphite are known to have a very high thermal conductivity at room temperature [40]. The tangential thermal conductivity of graphite is approximately ~ 3000 Wm⁻¹K⁻¹. Nanotubes have been predicted to have similar or even superior thermal conductivity [41]. Moreover, the thermal properties for both SWNTs and MWNTs remain to be thoroughly investigated. One of the issues is that it is difficult to perform measurements on a single nanotube. This is mainly due to aggregation effects. Theoretical work predicts that thermal conductivity along the tube axis could go from 1800 up to 6000 Wm⁻¹K⁻¹ for a single CNT at room temperature [42]. These high values are explained by the dominant contribution of the phonons [43] and their large mean free paths (~100 nm). It was also suggested that the thermal conductivity was temperature dependent [42, 44] as it can be seen in Figure 2.14.

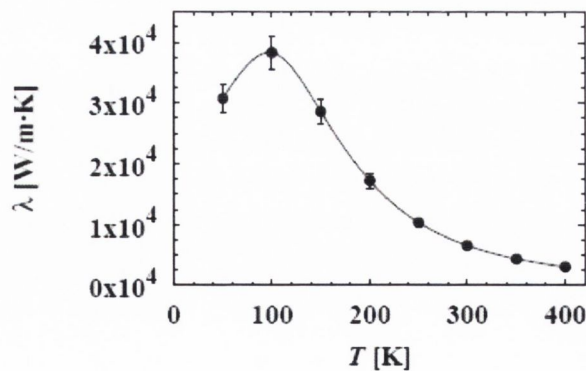


Figure 2.14: The calculated thermal conductivity as a function of the temperature according to Berber et al [44].

By using molecular dynamic simulations, on several types of SWNTs from 100 K to 500 K, Osman et al established that the thermal conductivity was not dependent on the chirality of nanotubes [45]. They also observed a peaking behavior of the thermal conductivity before falling off to higher temperatures. The peak shifted to higher temperatures for large nanotube diameters. A conductivity of $3000 \text{ Wm}^{-1}\text{K}^{-1}$ has been measured on individual MWNTs. In this case, the mean free path was estimated to be 500 nm [46].

2.3.4 Mechanical Properties of Carbon Nanotubes.

One of the most interesting features of carbon nanotubes are their outstanding mechanical properties. The high elastic modulus of a graphene sheet ($\sim 1000 \text{ GPa}$) [47] means carbon nanotubes may be stiffer and stronger than any known materials. This is due to strong covalent bonding between carbon atoms.

In 1993 computational work predicted a Young's modulus of 1500 GPa for SWNTs [48]. A few years later, additional theoretical work presented results where the Young's modulus was 1 TPa and the shear modulus was 0.45 TPa. These values were the same for any type of nanotube [49]. The first direct measurement was performed by Wong et al in 1997 using Atomic Force Microscopy (AFM)[50]. This measurement was achieved by randomly dispersing arc-MWNTs onto a MoS_2 substrate. Tubes pinned by depositing pads of SiO through a shadow mask. AFM was then used to directly measure lateral force – distance characteristics at various positions along the length of the nanotubes. Average value of 1.28 TPa and 14 GPa were obtained respectively for the Young's Modulus and the bending strength. Salvetat et al dropped a solution of MWNTs onto a well-polished alumina ultrafiltration membrane. Some of the tubes were therefore positioned across the pores (200 nm). By using an AFM in contact mode, they were able to bend MWNT over one of those pores [51]. The Young's modulus obtained for arc-discharge tubes was in a range from 650 GPa up to 1220 GPa, whereas for catalytically grown tubes the modulus dropped dramatically (10-50 GPa). This can be explained by the fact that the arc-discharge method produces CNTs with almost no defects. By contrast, nanotubes grown by catalytic methods will contain more defects.

The first stress strain response and strength at failure measurements were achieved on individual Arc-MWNTs in 2000 [53]. In order to reach this goal, Yu et al used a “nanostressing stage” located within a SEM. The nanotube was held at both ends by AFM cantilevers and stretched. The elongation of the CNT was plotted against the force applied and stress strain curves were obtained as shown in Figure 2.15.

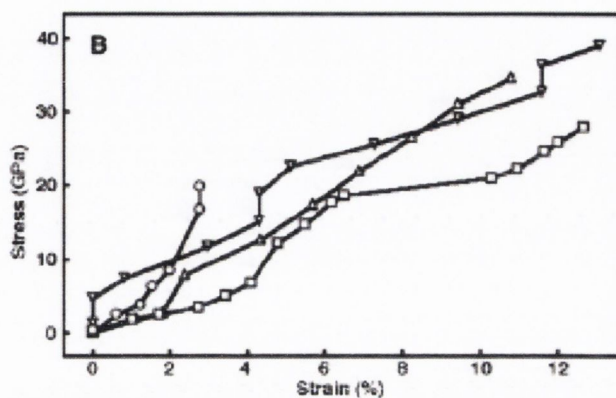


Figure 2.15: Stress strain curves of individual MWNTs [53].

The Young’s modulus values for the outer MWNT layer obtained from this curve ranged from 0.27 TPa to 0.95 TPa. Fracture of MWNTs occurred at strains of up to 12 % with strengths ranging from 11 up to 63 GPa. This gives an approximate value for nanotube toughness at ~ 1240 J/g [54]. The first measurement carried out on SWNTs was performed by Salvetat et al using a rope of SWNTs [55]. The technique they used was similar to the one used to measure the mechanical properties of MWNTs method [51]. They found a value of 1 TPa for the elastic modulus of a small diameter SWNTs (1.4 nm). Yu et al also performed some measurements on SWNTs ropes [56]. In this case, they used a “nanostressing stage” as described above. The breaking tensile strength for a SWNT was measured to be from 13 GPa to 52 GPa (mean 30 GPa). The Young’s Modulus was also evaluated to be in the range 0.32 TPa to 1.47 TPa (mean 1.002 TPa). In addition, failure occurred at a maximum strain of 5.3 % giving a toughness of ~ 770 J/g. Carbon nanotubes are also remarkably flexible and resilient materials. Using individual MWNTs, Falvo et al. have shown than they can be bent repeatedly through large angles using the tip of an AFM (Nanomanipulator AFM system)[57].

2.3.5 Carbon Nanotubes Production Methods.

To be commercially viable, CNTs needs to be produced on a large scale. The first macroscopic production of a few grams was realised in 1992 [58]. This was sufficient in order to carry out experimental work, but still too low for industrial scale. Therefore, much research has been done in a attempt to increase production. Nowadays, production rates have dramatically increased to kg per day. The cost, however, remains prohibitively high with a price of around 50 to 100 euros per gram of SWNTs. Another challenge is to produce nanotubes where the chirality, yield and the number of defect are controlled. This is key factor for many applications.

Today, there are three primary methods to produce carbon nanotubes. These are arc discharge, laser ablation and chemical vapor deposition. Both MWNTs and SWNTs can be synthesised by these techniques.

Arc discharge was the first method used to produced C_{60} and MWNTs [21]. In this process, two aligned graphitic rods, separated by few millimetres, are set up in chamber a containing an inert gas (such as helium) and connected to a power supply. When a high current is applied through theses rods (100 A), carbon sublimes forming a plasma between the graphitic rods. One electrode is stationary (anode) and the other one is moveable (cathode). In this way it is possible to keep the electrical current at a constant value by controlling the distance between theses electrodes. Condensed products are deposited onto the anode in the form of a hard outer shell with an inner core shell containing both nanotubes and carbon soot. By adding metal catalysts such as iron or cobalt into the cathode, SWNTs can be produced. This technique allows the production of high quality nanotubes with few defects. Unfortunately, the resulting product needs to be purified and nanotubes formed are short (50 μm). The production rate is about 120 grams per day with a low yield of 30 %. Although, Cadek et al. reported a yield up to 48 % for MWNTs [59]. A typical arc discharge apparatus is presented in the Figure 2.16.

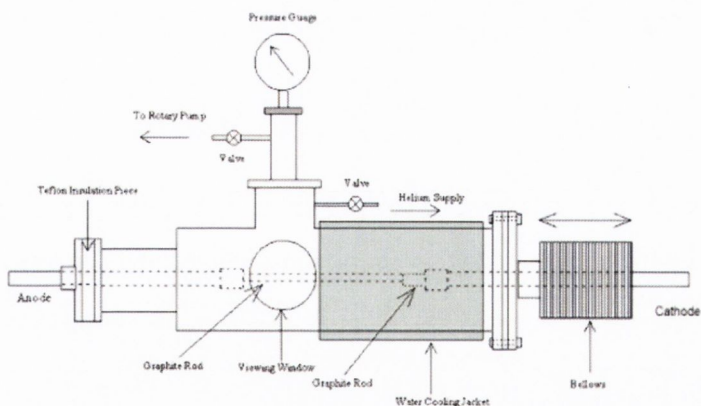


Figure 2.16: Schematic of an arc discharge generator [60].

The laser ablation technique was the first method used to generate fullerenes in the gas phase [18]. Carbon sublimation is achieved using a Nd: YAG pulsed laser, focused on a graphite disc surface under an argon (or helium) atmosphere at 500 Torr. The graphite target is set in a quartz tube and heated up to approximately 1200°C (fig: 2.17). The sublimed carbon vapour is carried by the argon flow and then condenses onto a water cooled copper collector. Similar to the arc discharge method, the presence of metallic particles (Fe, Co, or Ni) enables the formation of SWNTs. Product is collected from the water cooled support and also from the walls of the quartz tube. The yield and quality of nanotubes depends on the furnace temperature and the choice of catalytic particles [61]. For example, at 1200 °C, the nanotubes are free of defects. When the temperature decreases, the number of defects increases [62]. Also, the nanotube diameter can be tailored by varying the furnace temperature. Laser ablation gives a yield of nanotubes between 40% and 50%. However, this method is quite expensive due to the use of high purity graphite rods and the laser power required for this application. Also, the production rate is about 50 g per day which is very low for industrial applications.

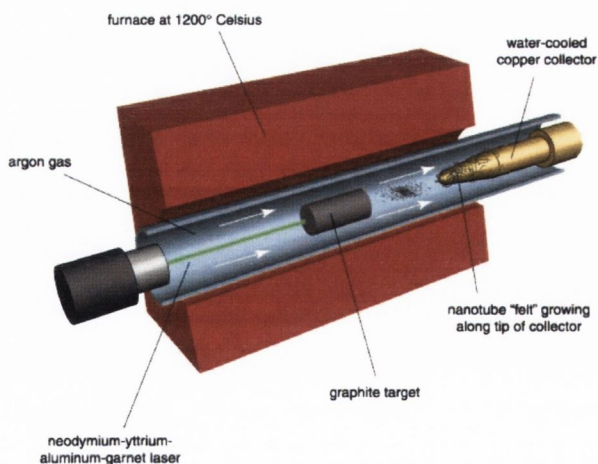


Figure 2.17: Experimental set up for the production of nanotubes by laser ablation[63].

The third and most common method used to produce nanotubes is Chemical Vapour Deposition (CVD). Yacaman et al. were the first to synthesise CNTs using the catalytic decomposition of acetylene over iron particles at 700°C [64]. Typically, the experiment is carried out under atmospheric pressure in a flow furnace. Catalysts particles can be either introduced in a gas phase or placed onto a substrate (fig 2.19). Hydrocarbon sources are decomposed into carbon radicals which nucleate onto the catalyst surface and reassemble to form nanotubes. Amorphous carbon (layers and filaments) and graphite layers can also be formed. During the procedure, the temperature can range from 500°C to 1100°C. Changing parameters such as the nature of the substrate, the size of metal particles and the reaction conditions (time, temperature, pressure), enables the size and the length of produced nanotubes to be controlled. For example, SWNTs of 0.6 mm long have been produced using CVD [65].

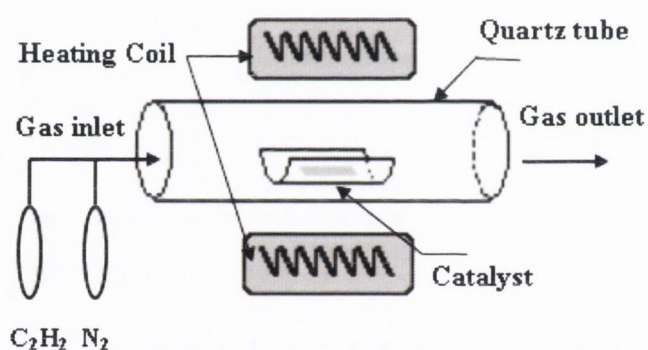


Figure 2.18: Schematic of Chemical Vapour Deposition [60].

One interesting variation of CVD is Plasma-Enhanced Chemical Vapour Deposition (PECVD). Using PECVD allows nanotubes to be grown perpendicular to the substrate surface [66]. CVD is therefore the most promising production technique it allows control of diameter, length and growth direction. Also, it is possible to scale up the production to industrial levels (50 kg per day). However, CVD techniques result in more nanotube defects compared with laser ablation or arc discharge. This results in lower value mechanical and electrical properties. Finally, it has to be emphasised that none of these techniques can produce specific nanotube chirality. The table below (Table 2.3) gives a summary of the CNT production methods.

Method	Principle	Advantage	Disadvantage	Production rate
Arc discharge (Iijima 1991)	Carbon atoms are generated through an electric arc between two graphite rods @ $T > 3000^{\circ}\text{C}$. Nanotubes are formed on one of the rods.	Few structural defects for both SWNTs and MWNTs	Short nanotubes and low yield production (30%)	120 g day^{-1}
CVD (Yacaman 1993)	A substrate is placed in an oven @ 600°C and carbon bearing gas is slowly added. Carbons atoms are formed by gas decomposition and then recombine as CNTs	Possibility of long nanotubes, high yield and easiest to scale up to industrial production	CNTs have more defect.	50 kg day^{-1}
Laser ablation	Carbon atoms are generated by the blast of a laser on a graphite target which contains appropriate particles. High temperature (3000°C).	Easy to control the diameter by varying the reaction temperature. Good yield production.	Most costly method because of the use of lasers.	50 g day^{-1}

Table 2.3: Summary of carbon nanotubes production techniques.

2.3.6 Health Impact of Carbon Nanotubes.

The use of carbon nanotubes in on a daily basis and more particularly for medical applications requires first a comprehensive impact on health because of their nanoscales. Most of nanomaterials (fullerenes, nanoparticles, nanofibres and nanotubes) are made of carbon atoms, with distinct geometries, surface area and diverse physical and chemical properties. Thus, according to these factors, some nanoparticles may be potentially toxic. And they can be considered as dangerous as quartz [67]. Concern has been raised over the safety of CNTs because they have three properties that are clearly associated with pathogenicity in particles. First they are nanoparticles so they have more toxicity than larger sized particles due to a larger surface area. This increases the intrinsic toxicity of the surface [68, 69]. However, Sayes et al. demonstrated that cytotoxicity of SWNTs on human fibroblast decreased by increasing

the degree of functionalisation on the surface [70]. CNTs are also fibre shaped and so they might behave like asbestos and other pathogenic fibres which have toxicity associated with their needle like shape. Sato et al. separated MWNTs of 220 and 825 nm using controlled strong acid condition [71]. During a short incubation time, clusters of both samples were shown to be surrounded by macrophages as a consequence of the activation of innate immunity. The shorter tubes displayed a lower inflammatory response. In both cases, no severe effects, such as necrosis or degeneration, were observed around CNTs throughout the experimental period of 4 weeks. CNTs are essentially graphitic structure and so they are expected to be biologically biopersistent. Biopersistence is a key factor in the toxicology of very long fibres, which are often difficult for macrophages to phagocytose. A high Biopersistence increases the toxicity of all fibres. Therefore, long CNTs ($>17 \mu\text{m}$) may become biopersistent and thus they may induce toxic response such as glass fibre (Ye et al). Despite the evidence of CNTs cytotoxicity in both in vitro and in vivo studies [72], there have also been a number of published studies into CNT-based biomaterials, which support the biocompatibility of CNT and CNT-based materials with various cell lines, and antibodies [73-75]. Therefore, the use of carbon nanotubes for biomedical applications still needs further investigation in order to fully assess the risk of handling those materials.

2.4 Polymer Carbon Nanotubes Composites.

Due to their outstanding properties, carbon nanotubes can be seen as ideal candidate for advanced filler materials in composites. The π -bonding along the side walls allows an excellent electrical conduction while strong carbon-carbon bonds are responsible for mechanical robustness. Their high aspect ratio suggests that percolation in composites may be achieved at low loadings content. High strength combined with low density make CNTs the potential ultimate reinforcement for polymer materials. The first polymer-nanotube composite was made by Ajayan et al in 1994 using purified arc discharge nanotubes with epoxy resin by mechanical mixing [76]. Since then much more research was carried out to use nanotubes in polymer or epoxy matrix for the improvement of the mechanical, electrical and thermal properties of neat materials.

Properties of the polymers carbon nanotubes composites used in this thesis will be presented in more detailed in chapter four, five and six.

2.4.1 Functionalisation of carbon nanotubes.

In order to fully exploit the unique properties of nanotubes, it is necessary to be able to process and handle these materials on a macroscopic scale. Carbon nanotubes in their unmodified, pure form are highly unreactive due to the seamless arrangement of hexagon rings without any dangling bonds. This makes them insoluble in all common solvents. Also, this can result in a lack of interfacial bonding between polymer matrix and carbon nanotubes. Therefore, covalent functionalisation and surface chemistry are important factors for CNT processing and applications.

Covalent modifications of CNTs tips and sidewalls can be achieved by oxidation or fluorination. As one might expect, the more highly strained caps at the end of nanotubes contain the most reactive carbon atoms [77] and hence the ends of nanotubes are the more susceptible to functionalisation than the side-walls. Also, it is known that real nanotubes are not completely defect free. Several different structures other than the main hexagonal shape are incorporated along the tubule wall such as pentagons and heptagonal rings. These sites are potentially more reactive than the more stable hexagonal lattice [78]. Also smaller diameter SWNTs are more reactive than larger nanotubes.

Carbon nanotubes respond to strong acids and other chemical oxidisers which can attach functional groups such as hydroxyl, carboxyl and ketone groups [79-81]. Other species such as small molecules or polymer chains can then be covalently attached to these functional groups through traditional chemical reactions [82]. After various modifications, dissolution of carbon nanotubes in various organic is possible (tetrahydrofuran, dichloromethane and chloroform) [83-86]. Water soluble functionalised nanotubes have also been achieved [85, 86]. Direct fluorination of side walls has also been produced between 250°C and 400°C [87]. Fluorination above 400°C was found to cause decomposition of the nanotube structure demonstrating the harsh treatment involved.

The major drawback of covalent functionalisation is that these modifications dramatically alter the structure and intrinsic electrical and mechanical properties of CNTs. Another way to enable a good dispersion of CNTs and therefore to make them suitable for polymer composites is the use of non-covalent chemistry. This type of chemistry involves self-assembly of molecules or macromolecules about nanotubes to form thermodynamically stable structure held together by weak non-covalent interactions. These include hydrogen bonding, π - π stacking, van der Waals forces, electrostatic forces and hydrophobic and hydrophilic interactions [88, 89]

2.4.2 Electrical Properties.

Improving the electrical conductivity of bulk polymers is important for many applications by using conductive fillers. For example, CNTs can be used for electromagnetic interference, flexible display or electrostatic dissipations [90]. For this purpose, Sandler et al improved the conductivity of an epoxy resin from 10^{-6} Sm^{-1} up to 10^{-2} Sm^{-1} by adding less than 0.1 volume fraction of SWNTs [91]. CNTs are really interesting compared to other filler such as carbon black because of their high aspect ratio and high electrical conductivity. This is because the critical loading level of filler called percolation threshold required to achieve a dramatic increase of the conductivity of the composite decrease when the aspect ratio of the filler increase. Lowering the percolation threshold as much as possible is crucial for conducting composites. If the amount of fillers is too high, this may results in unwanted changes of the overall properties of the composites and processing issues. Therefore, CNTs have a great potential for this purpose. For example, conductivity of most polymers lies in the region of 10^{-10} Sm^{-1} . But according to the polymer matrix, conductivities of 0.01 to 0.1 Sm^{-1} can be obtained for 5 % loading of CNTs [92]. Therefore, CNTs can improve polymers conductivities without changing the intrinsic properties of the polymers host. However, if nanotubes content exceeds 10 wt %, the viscosity of the composite can be too large for processing [93].

2.4.3 Mechanical Properties.

Four main parameters are required for an effective reinforcement. These are large aspect ratio, good dispersion, alignment and interfacial stress transfer. The mechanical

strength enhancement is the results of the load transfer from the polymer matrix to the embedded tubes [94]. This transfer occurs at the interface between the polymer and the filler. Thanks to their large aspect ratio, carbon nanotubes can increase the interfacial area between themselves and the polymer. This enables a greater stress transfer between these two materials. However, the length of the nanotubes can have a significant effect on the reinforcement. This matter will be discussed in more detail in the following chapter. The effect of the alignment is less crucial. The difference between random orientation and perfect alignment is a factor of five in composite modulus it will be shown in more detail in chapter 3. While alignment is necessary to maximise strength and stiffness, it is not always beneficial. Aligned composites have very an-isotropic mechanical properties, which may need to be avoided in bulk samples. In fibres however alignment has no downside and is a way to maximise reinforcement.

Dispersion of nanotube is crucial for reinforcement. Nanotubes must be individually coated with polymer to achieve a good load transfer between these two materials. Good dispersion also results in a more uniform stress distribution and minimizes the presence of stress concentration centres. The effects of poor dispersion can be seen in a number of systems when the nanotube loading content is increasing beyond the point where aggregation begins due to strong inter-tubes Van der Waals interactions. As a result, the strength and the modulus generally decrease [95].

One of the most important requirements for reinforcement is that the external stress applied to the composites is efficiently transferred to the nanotubes. An interesting parameter to quantify this transfer is the interfacial shear strength (IFSS) which governs the maximum stress transfer to the nanotube [54]. Computational works have been carried out to evaluate the IFSS polymer and epoxy Carbon nanotubes composites [54]. Despite the difficulty to measure the IFSS with nanotubes, some progress has been made. For example, Wagner et al used observations of stress induced nanotube fracture made by TEM to estimate a value of 500 MPa [96]. Atomic force microscopy was also used to manipulate nanotubes protruding from holes in an epoxy / CNTs film. When nanotubes were embedded with short lengths IFSS was estimated to be between 300-400 MPa. But this value dropped to 30-90 MPa with longer embedded lengths suggesting that end effects are important [97]. Barber et al pushed perpendicularly CNTs into the surface of heated polyethylene-butene matrix. After cooling they measured the force required to pull the nanotubes out. The measured force was between 10-100 MPa [98].

The strength of the interface will also depend on the interaction between the polymer and the nanotubes. An this interaction dependent on the matrix type [99]. A number of studies suggest that interfacial interactions with nanotubes result in an interfacial region of polymer with morphology and properties different to the bulk. For example, conjugated polymers can wrap around MWNTs [100]. In addition, dendritic polymer growth has been observed to nucleate from defects on the nanotube [100, 101]. Others studies mentioned nucleation of crystallinity in the presence of nanotubes [102, 103]. Using PVA, this nucleation results in high strength crystalline coating [104]. However, the strongest interface appears to be created by functionalisation. The young's modulus of the polymer can double or even triple by adding nanotubes to the matrix [105]. Nanotubes can also increase dramatically the toughness of the composite by absorbing the energy applied to the matrix. Using a coagulation spinning technique with PVA, Neri et al produced fibres with a remarkable toughness of 500 J/g with less 1 wt % of nanotubes [106].

2.5 References

1. Roff, W.J., J.R. Scott, and J. Pacitti, *Handbook of Common Polymers*. CRC Press, Cleveland,, 1971: p. p. 72.
2. Hyon, S.H., et al., *Poly(vinyl alcohol) hydrogels as soft contact lens material*. *Journal of biomaterials science*. Polymer edition, 1994. 5: p. 394.
3. Hassan, C.M. and A.P. Nikolaos, *Structure and Applications of Poly(vinyl alcohol) Hydrogels Produced by Conventional Crosslinking or by Freezing/Thawing Methods* *Advances in Polymer Science*, 2004. 153: p. 37.
4. Peppas, N.A. and R.E. Berner, *Proposed method of intracopdal injection and gelation of poly (vinyl alcohol) solution in vocal cords: polymer considerations* *Biomaterials*, 1980. 1: p. 153.
5. Pritchard, J.G., *Poly(vinyl alcohol); Basic properties and uses* Gordon and Breach Science Publishers, London, 1970.
6. Tsiji, W., R. Kitamura, and T. Ikida, *Bull. Inst. Chem. Kyoto Univ.*, 1964. 42: p. 93.
7. Kenny, J.F. and G.W. Willcockson, *J. Polymer Sci*, 1966. 4: p. 679.
8. Carothers, W., *United States Patent 5075115*. 1932.
9. Tsuji, H. and Y. Ikada, *Blends of Aliphatic Polyesters. II. Hydrolysis of Solution-Cast Blends from Poly(L-lactide) and Poly (1-caprolactone) in Phosphate-Buffered Solution* *Journal of Applied Polymer Science*, 1998. 67(3): p. 405.
10. Drumright, R.E., P.R. Gruber, and D.E. Henton, *Poly(lactic Acid Technology)*. *Advanced Materials*, 2000. 12(23): p. 1841.
11. Lipinsky, E.S. and R.G. Sinclair, *Is lactic acid a commodity chemical?* *Chem. Eng. Prog.*, 1986. 82: p. 26.
12. Vert, M., G. Schwach, and J. Coudane, *J. Macromol. Sci. Pure Appl. Chem*, 1995. A32: p. 787.

13. Lunt, J. and A. Shafer, *Polylactic Acid Polymers from Corn: Potential Applications in the Textiles Industry*. 2002.
14. Gosline, J.M., et al., *The mechanical design of spider silks: from fibroin sequence to mechanical function*. J Exp Biol, 1999. 202(23): p. 3295-3303.
15. Lazaris, A., et al., *Spider Silk Fibers Spun from Soluble Recombinant Silk Produced in Mammalian Cells*. Science, 2002. 295(5554): p. 472-476.
16. Kaye & Laby, Table of Physical and Chemical Constants 1995. 16th Ed.
17. Young, H.D. and R.A. Freedman, University Physics, 9th Ed., (addison wesley), 1996.
18. Kroto, H.W., et al., *C60: Buckminsterfullerene*. Nature, 1985. 318(6042): p. 162-163.
19. Kroto, H., *Symmetry, space, stars and C₆₀*. Reviews of Modern Physics, 1997. 69(3): p. 703.
20. Smalley, R.E., *Discovering the fullerenes*. Reviews of Modern Physics, 1997. 69(3): p. 723.
21. Kratschmer, W., et al., *Solid C60: a new form of carbon*. Nature, 1990. 347(6291): p. 354-358.
22. Iijima, S., *Helical microtubules of graphitic carbon*. Nature, 1991. 354(6348): p. 56-58.
23. Iijima, S. and T. Ichihashi, *Single-shell carbon nanotubes of 1-nm diameter*. 1993. 363(6430): p. 603-605.
24. Bethune, D.S., et al., *Cobalt-catalysed growth of carbon nanotubes with single-atomic-layer walls*. Nature, 1993. 363(6430): p. 605-607.
25. Radushkevich, L.V. and V.M. Lukyanovich, Zurn Fisic Chim, 1952. 26: p. 88.
26. Oberlin, A., M. Endo, and T. Koyama, *Filamentous growth of carbon through benzene decomposition*. Journal of Crystal Growth, 1976. 32(3): p. 335-349.
27. Zheng, X., et al., *Ultralong single-wall carbon nanotubes*. 2004. 3: p. 673.
28. Tománek, D. and T. Adams. *The Nanotube site*, www.pa.msu.edu/cmp/csc/NTSite/nanopage.html. 2000 [cited].
29. Wilder, J.W.G., et al., *Electronic structure of atomically resolved carbon nanotubes*. Nature, 1998. 391(6662): p. 59-62.
30. Marcoux, P., *Réactivité et manipulation de nanotubes de carbone monocouches : fonctionnalisation de surface par greffage covalent et mise en œuvre comme agent structurant*. 2002, ÉCOLE DOCTORALE D'ANGERS: Anger.
31. Hamada, N., S.-i. Sawada, and A. Oshiyama, *New one-dimensional conductors: Graphitic microtubules*. Physical Review Letters, 1992. 68(10): p. 1579.
32. Mintmire, J.W., B.I. Dunlap, and C.T. White, *Are fullerene tubules metallic?* Physical Review Letters, 1992. 68(5): p. 631.
33. Saito, R., et al., *Electronic structure of chiral graphene tubules*. Applied Physics Letters, 1992. 60(18): p. 2204-2206.
34. Mintmire, J.W., D.H. Robertson, and C.T. White, *Properties of fullerene nanotubules*. Journal of Physics and Chemistry of Solids, 1993. 54(12): p. 1835-1840.
35. Dresselhaus, M.S., G. Dresselhaus, and P.C. Eklund, *Science of fullerenes and Carbon Nanotubes*, ed. A.P. INC. 1996, San Diego.
36. Wei, B.Q., R. Vajtai, and P.M. Ajayan, *Reliability and current carrying capacity of carbon nanotubes*. Applied Physics Letters, 2001. 79(8): p. 1172-1174.
37. Thostenson, E.T., Z. Ren, and T.-W. Chou, *Advances in the science and technology of carbon nanotubes and their composites: a review*. Composites Science and Technology, 2001. 61(13): p. 1899-1912.

38. Kim, B.M. and M.S. Fuher, *Properties and applications of high-mobility semiconducting nanotubes*. Journal of Physics: Condensed Matter, 2004. 16(18): p. R553.
39. Tang, Z.K., et al., *Superconductivity in 4 Angstrom Single-Walled Carbon Nanotubes*. Science, 2001. 292(5526): p. 2462-2465.
40. Kave, G.W.C. and T.H. Laby, *Tables of physical and chemical constants*. 16th ed., Longman, London, 1995.
41. Ruoff, R.S. and D.C. Lorents, *Mechanical and thermal properties of carbon nanotubes*. Carbon, 1995. 33(7): p. 925-930.
42. Hone, J., M. Whitney, and A. Zettl, *Thermal conductivity of single-walled carbon nanotubes*. Synthetic Metals, 1999. 103(1-3): p. 2498-2499.
43. Hone, J., *Phonons and Thermal Properties of Carbon Nanotubes*. Applied Physics 2001. 80: p. 273-286.
44. Berber, S., Y. Kwon, and D. Tománek, *Unusually High Thermal Conductivity of Carbon Nanotubes*. Physical Review Letters, 2000. 84(20): p. 4613-4616.
45. Osman, M.A. and D. Srivastava, *Temperature dependence of the thermal conductivity of single-wall carbon nanotubes*. Nanotechnology, 2001. 12(1): p. 21-24.
46. Kim, P., et al., *Thermal transport measurements of individual multiwalled nanotubes*. Physical Review Letters, 2001. 8721(21).
47. Kelly, B.T., *Physics of graphite*. Applied science, London,, 1981.
48. Overney, G., W. Zhong, and D. Tomanek, *Structural rigidity and low-frequency vibrational-modes of long carbon tubules*. Zeitschrift fur physik D-Atoms molecules and clusters, 1993. 27(1): p. 93-96.
49. Lu, J.P., *Elastic properties of single and multilayered nanotubes*. Journal of Physics and Chemistry of Solids, 1997. 58(11): p. 1649-1652.
50. Wong, E.W., P.E. Sheehan, and C.M. Lieber, *Nanobeam Mechanics: Elasticity, Strength, and Toughness of Nanorods and Nanotubes*. Science, 1997. 277: p. 1971-1975.
51. Salvetat, J.P., et al., *Elastic modulus of ordered and disordered multiwalled carbon nanotubes*. Advanced Materials, 1999. 11(2): p. 161-165.
52. Salvetat, J.P., et al., *Mechanical properties of carbon nanotubes*. Applied Physics A, 1999. 69(3): p. 255.
53. Yu, M., et al., *Strength and Breaking Mechanism of Multiwalled Carbon Nanotubes Under Tensile Load*. Science, 2000. 287: p. 637-640.
54. Coleman, J.N., et al., *Small but strong: A review of the mechanical properties of carbon nanotube-polymer composites*. Carbon, 2006. 44(9): p. 1624-1652.
55. Salvetat, J.P., et al., *Elastic and shear moduli of single-walled carbon nanotube ropes*. Physical Review Letters, 1999. 82(5): p. 944-947.
56. Yu, M.-F., et al., *Tensile Loading of Ropes of Single Wall Carbon Nanotubes and their Mechanical Properties*. Physical Review Letters, 2000. 84(24): p. 5552.
57. Falvo, M.R., *Bending and buckling of carbon nanotubes under large strain*. Nature, 1997. 389: p. 582-584.
58. Ebbesen, T.W. and P.M. Ajayan, *Large-scale synthesis of carbon nanotubes*. Nature, 1992. 358(6383): p. 220-222.
59. Cadek, M., et al., *Optimisation of the arc-discharge production of multi-walled carbon nanotubes*. Carbon, 2002. 40(6): p. 923-928.
60. Cadek, M., *Mechanical reinforcement effects of carbon nanotube polymer composites, in School of physics*. 2004, Trinity College Dublin: Dublin.

61. Guo, T., et al., *Catalytic growth of single-walled nanotubes by laser vaporization*. Chemical Physics Letters, 1995. 243(1-2): p. 49-54.
62. Guo, T., et al., *Self-Assembly of Tubular Fullerenes*. J. Phys. Chem., 1995. 99: p. 10694.
63. Yakobson, B.I. and R.E. Smalley, *Fullerene nanotubes: C-1000000 and beyond*. American Scientist, 1997. 85(4): p. 324-337.
64. Jose-Yacaman, M., et al., *Catalytic growth of carbon microtubules with fullerene structure*. Applied Physics Letters, 1993. 62(2): p. 202-204.
65. Kim, W., et al., *Synthesis of Ultralong and High Percentage of Semiconducting Single-walled Carbon Nanotubes*. Nano Lett., 2002. 2(7): p. 703-708.
66. Chris, B., et al., *Plasma-induced alignment of carbon nanotubes*. Applied Physics Letters, 2000. 77(6): p. 830-832.
67. Kumar, C., *Nanomaterials for Medical Diagnosis and Therapy*. 2006: Wiley-VCH.
68. Donaldson, K., et al., *Nanotoxicology*, . Occupational and Environmental Medicine., 2004. 61: p. 727-728.
69. Tran, C.L., et al., *Inhalation of poorly soluble particles. II. Influence of particule surface area on inflammation and clearance*. Inhalation Toxicology, 2000. 12: p. 113-126.
70. Sayes, C.M., et al., *Functionalization density dependence of single walled carbon nanotubes cytotoxicity in vitro*. Toxicology letters, 2006. 161: p. 135-142.
71. Sato, Y., et al., *Influence of length on cytotoxicity of multi walled carbon nanotubes against human acute monocytic leukemia cell line THP-1 in vitro and subcutaneous tissue of rats in vivo*. molecular Biosystems, 2005. 1: p. 176-182.
72. Smart, S.K., et al., *The biocompatibility of carbon nanotubes*. Carbon, 2006. 44: p. 1034-1047.
73. McKenzie, J.L., et al., *Decreased functions of astrocytes on carbon nanofibre materials*. Biomaterials, 2004. 25: p. 1309-1317.
74. Correa-Duarte, M.A., et al., *Fabrication and biocompatibility of carbon nanotube-based 3D networks as scaffolds for cell seeding and growth*. Nano Lett., 2004. 116: p. 1166-1169.
75. Naguib, N.N., et al., *Effect of carbon nanotube structure on the binding of antibodies*. Nanotechnology, 2005. 16: p. 567-571.
76. Ajayan, P.M., et al., *Aligned Carbon Nanotube Arrays Formed by Cutting a Polymer Resin--Nanotube Composite*. Science, 1994. 265(5176): p. 1212-1214.
77. Colbert, D.T., et al., *Growth and Sintering of Fullerene Nanotubes*. Science, 1994. 266: p. 1218-1222.
78. Chang, H. and A. Bard, *Scanning Tunneling Microscopy Studies of Carbon Oxygen Reactions on Highly Orientated Pyrolytic Graphite*. J. Am. Chem. Soc., 1991. 113: p. 5588-5596.
79. Dillon, A.C., et al., *A simple and Complete Purification of Single-Walled Carbon Nanotubes Materials*. Advanced Materials, 1999. 11(16): p. 1354-1358.
80. Yu, R., et al., *Platinum Deposition on Carbon Nanotubes via Chemical Modification*. Chemistry of Materials, 1988. 10: p. 718-722.
81. Hiura, H., T.W. Ebbesen, and K. Tanigaki, *opening and purification of carbon nanotubes in high yields*. Advanced materials, 1995. 7: p. 275-276.
82. Sun, Y.P., et al., *Preparation and Optical Properties of Dye-Linked Carbon Nanotubes*. Proceedings of the Electrochemical Society, 2000. 2000: p. 282-290.
83. Chen, J., et al., *Solution Properties of Single-Walled Carbon Nanotubes*. Science, 1998. 282: p. 95-98.

84. Hamon, M.A., et al., *Dissolution of Single-Walled Carbon Nanotubes*. *Advanced Materials*, 2004. 11(10): p. 834-840.
85. Riggs, J.E., et al., *Strong Luminescence of Solubilised Carbon Nanotubes*. *Journal of the American Chemical Society*, 2000. 122: p. 5879-5880.
86. Czerw, R., et al., *Organization of Polymers onto Carbon Nanotubes: A route to nanoscale Assembly*. *Nano Lett.*, 2001. 1: p. 423-427.
87. Nakajima, T., S. Kasamatsu, and Y. Matsuo, *Synthesis and characterization of fluorinated carbon nanotube*. *European Journal of Solid State and Inorganic Chemistry*, 1996. 33(14): p. 831-840.
88. Grenier, E., et al., *Synthesis of Poly(L-lactide)-Functionalized Multiwalled Carbon Nanotubes by Ring-Opening Polymerization*. *Macromolecular Chemistry and Physics*, 2001. 123: p. 3838-3840.
89. Star, A., et al., *Preparation and Properties of Polymer-Wrapped Single-Walled Carbon Nanotubes*. *Angewandte Chemie International Edition*, 2001. 41: p. 1721-1725.
90. Harris, P.J.F., *Carbon nanotube composites*. *International Materials Reviews*, 2004. 49(1): p. 31-43.
91. Sandler, J., et al., *Development of a dispersion process for carbon nanotubes in an epoxy matrix and the resulting electrical properties*. *Polymer*, 1999. 40(21): p. 5967-5971.
92. Baughman, R.H., A.A. Zakhidov, and W.A. de Heer, *Carbon nanotubes - the route toward applications*. *Science*, 2002. 297(5582): p. 787-792.
93. Muñoz, E., et al., *Highly Conducting Carbon Nanotube/Polyethyleneimine Composite Fibers*. *Advanced Materials*, 2005. 17(8): p. 1064-1067.
94. Ajayan, P.M., et al., *Single-Walled Carbon Nanotube-Polymer Composites: Strength and Weakness*. *Advanced Materials*, 2000. 12(10): p. 750-753.
95. Manchado, M.A.L., et al., *Thermal and mechanical properties of single-walled carbon nanotubes-polypropylene composites prepared by melt processing*. *Carbon*, 2005. 43(7): p. 1499-1505.
96. Wagner, H.D., et al., *Stress-induced fragmentation of multiwall carbon nanotubes in a polymer matrix*. *Applied Physics Letters*, 1998. 72(2): p. 188-190.
97. Cooper, C.A., et al., *Detachment of nanotubes from a polymer matrix*. *Applied Physics Letters*, 2002. 81(20): p. 3873-3875.
98. Barber, A.H., S.R. Cohen, and H.D. Wagner, *Measurement of carbon nanotube--polymer interfacial strength*. *Applied Physics Letters*, 2003. 82(23): p. 4140-4142.
99. Yang, M., V. Koutsos, and M. Zaiser, *Interactions between Polymers and Carbon Nanotubes: A Molecular Dynamics Study*. *J. Phys. Chem. B*, 2005. 109(20): p. 10009-10014.
100. McCarthy, B., et al., *A Microscopic and Spectroscopic Study of Interactions between Carbon Nanotubes and a Conjugated Polymer*. *J. Phys. Chem. B*, 2002. 106(9): p. 2210-2216.
101. McCarthy, B., et al., *Observation of site selective binding in a polymer nanotube composite*. *Journal of Materials Science Letters*, 2000. 19(24): p. 2239-2241.
102. Sandler, J., et al., *Crystallization of carbon nanotube and nanofiber polypropylene composites*. *Journal of Macromolecular Science-Physics*, 2003. B42(3-4): p. 479-488.
103. Grady, B.P., et al., *Nucleation of Polypropylene Crystallization by Single-Walled Carbon Nanotubes*. *J. Phys. Chem. B*, 2002. 106(23): p. 5852-5858.

104. Coleman, J.N., et al., *High Performance Nanotube-Reinforced Plastics: Understanding the Mechanism of Strength Increase*. *Advanced Functional Materials*, 2004. 14(8): p. 791-798.
105. Blake, R., et al., *A Generic Organometallic Approach toward Ultra-Strong Carbon Nanotube Polymer Composites*. *J. Am. Chem. Soc.*, 2004. 126(33): p. 10226-10227.
106. Nerie, W., et al., *Surfactant-Free Spinning of Composite Carbon Nanotube Fibers*. *Macromolecular Rapid communications*, 2006. 27(6042): p. 1035-1038.

Chapter 3: Composite Processing & Characterisation Methods.

3.1 Introduction.

In the previous chapter, the properties of the materials investigated in this thesis were introduced. Carbon nanotubes were described in detail along with the various polymer hosts which were used to produce CNT composites. Several processing techniques can be used in order to achieve a good dispersion of CNTs in a chosen matrix. Each technique has particular advantages and may be suitable only for a specific type of polymer. The most common techniques are solution processing, melt processing, and in situ polymerisation processing [1]. More recently, film and fibre composites have been produced using novel techniques such as Buchner filtration to make Buckypaper paper [2], chemical vapour deposition [3], coagulation spinning [4] and electrospinning [5].

In this chapter, the processing techniques used to make our composite materials are introduced. The techniques performed to characterise our composites will also be explained. Finally, a number of theoretical models for the mechanical reinforcement of carbon nanotube-polymer composites are discussed.

3.2 Composites Processing.

A number of techniques were used to synthesise CNTs-polymer composites. Each technique used was chosen to optimise the dispersion of CNTs in each host biopolymer matrix used in this thesis. Mechanical reinforcement is dependent on the uniformity of this CNT dispersion. With this in mind, PMMA/carbon nanotubes composites were fabricated by polymerisation of the MMA monomer in the presence of the carbon nanotubes, followed by solution processing with a second batch (or polymerised PMMA). PLLA and Biosteel composites were both fabricated by solution processing. Finally, we used electrospinning processing to make PVA composites.

3.2.1 In Situ Polymerisation.

In situ polymerisation has been investigated over the last 8 years for the preparation of polymer grafted nanotubes. These modified CNTs can then be processed to make a polymer composite. This technique is particularly useful for the preparation of polymers which are insoluble and/or thermally unstable. The process can be applied to the preparation of almost any polymer composite. Of particular advantage is that CNTs can be strongly attached to the polymer matrix, either covalently or non-covalently. Non-covalent binding between the polymer and nanotube involves adsorption and wrapping of the polymer around the nanotube. This occurs due to Van der Waals interactions and π - π interactions. Covalent binding occurs when an initiator is attached onto the surface of the nanotubes. The monomers can then be polymerised from this point. This results in the attachment of polymer molecules to the nanotube. Another advantage of in situ polymerisation is that it allows the preparation of composites with high CNT contents and good miscibility with almost any polymer. Radical, chain transfer, anionic and ring-opening polymerisations can be used for in situ polymerisation process.

In 1999, Jia et al were the first to use this technique in order to obtain PMMA/MWNT composites. To achieve this goal, they used radical in situ polymerisation with 2,2-azobisisobutyronitrile (AIBN) [6]. Further work on PMMA was subsequently done using carboxyl functionalised MWNTs [7] and SWNTs [8] with AIBN and radical in situ polymerisation. Other polymer composites were also successfully made by this process. For example, Poly(p-phenylene benzobisoxadazole) / SWNTs composites [9] and Polyamide 6 / MWNTs [10].

3.2.2 Solution Processing.

This technique is probably the most common method to produce polymer CNT composites. Solution processing consists simply of mixing nanotubes with the desired matrix in a suitable solvent. The process is straightforward and the equipment required is

inexpensive. Solution processing steps can vary depending on the polymer/nanotube system used. However, a general procedure can be described as follows.

First, nanotubes are dispersed in either a solvent or a polymer solution by energetic agitation. If nanotubes are first dispersed in a solvent, the desired concentration of polymer is then added followed by extra energetic agitation. Agitation can be provided by shear mixing, magnetic stirring, reflux or ultrasonication. The benefit of the agitation is that it allows for de-aggregation of the nanotubes. The time and mode of agitation can fluctuate dramatically depending on to the polymer and nanotubes concentrations, the solvent and the type of nanotubes used, i.e. SWNTs, MWNTs or functionalised CNTs. Other, CNT dispersions are not stable in polymer solutions. Different approaches can be used to address this problem. For example, MWNTs were mixed with Poly(m-phenylenevinylene-co-2,5dioctoxy-p-phenylenevinylene) (Pmpv) in toluene by ultrasonication. This suspension was stable over an indefinite period [11] due to the ability of the Pmpv to wrap around the nanotube. Coleman et al. also achieved indefinitely stable suspensions using catalytic MWNTS in PVA/H₂O solution [12]. Polymers which are unable to wrap around nanotubes cannot hold them in suspension and in this case all carbon material will settle out of the solution [13]. Recently Giordani et al. have shown that for a low loading level of 0.02 mg/mL in a solution of N-methyl-2-pyrrolidone, CNTs can behave as if they are soluble [14]. An alternative method to achieve a good dispersion of CNTs in solvents is to use surfactants to disperse nanotubes before mixing with the polymer [15]. The most common choice of surfactants are derivatives of sodium dodecylsulfate (SDS). After dispersing, well dispersed polymer/CNT solution can be evaporated to produce composite films. Alternatively, the solution can be drop cast or spin coated. Control over evaporation can be achieved by adjusting the temperature, the vacuum and the amount of solution deposited. For spin coating the thickness of the film can be adjusted by changing the rotation speed.

3.2.3 Electrospinning Processing.

3.2.3.1 Introduction.

The final technique we used to produce polymer carbon nanotube composites in this thesis is electrospinning. The first electrospun polymer/CNT composites were produced in 2003 [5]. This process, first patented in 1934 [16], allows production of polymeric nanofibres with diameters ranging from 3nm to over 1 μ m [17]. Production of nanofibres can also be achieved by techniques such as drawing, template synthesis, phase separation and self-assembly. However, over the last 10 years the electrospinning technique has started to generate a lot of interest in many fields because of processing advantages compared to other techniques (Table 3.1).

Process	Technological advances	Ease of processing	Advantages	Limitations
Drawing	Laboratory	Easy	Minimum equipment required	Discontinuous process & limited to few polymers
Template synthesis	Laboratory	Moderately easy	Good control of nanofibres diameters	Limited to few polymers
Phase separation	Laboratory	Easy	Minimum equipment required	Limited to few polymers
Self assembly	Laboratory	Difficult	Good to achieve small nanofibres	Complex process
Electrospinning	Laboratory Potential for industry	Moderately easy	Cost effective, long continuous nanofibres & large variety of polymer	Jet instability

Table 3.1: Comparison of processing techniques for synthesising polymeric nanofibres [18].

Electrospinning has been investigated and developed by a number of researchers [17, 19-24]. In its simplest form, this technique is based on three major components (fig: 3.1). First, a high-voltage power supply is used to generate an electric field (the voltage range is usually from 1kV up to 30 kV). Second, a capillary tube or metallic needle of small diameter (spinneret) is connected to a syringe in which the polymer solution (or melt) is hosted. The solution can be fed through the spinneret at a constant and controllable rate using a syringe pump. The third component is the collector (grounded conductor). Different types of collectors

have been developed for nanofibre deposition. The most common one is a simple metallic plate where the nanofibres are deposited randomly. However, more complex collectors have been engineered to align nanofibres or to develop more complex nanofibre patterns. These include cylinder collector [25], a knife edge disk [26] and a parallel conducting collector [27].

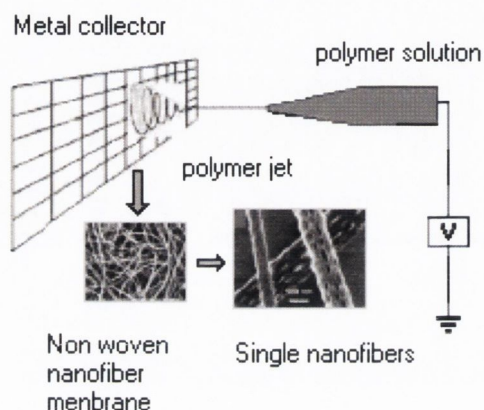


Figure 3.1: Schematic of electrospinning set up to produce polymeric nanofibres [17].

3.2.3.2 Electrospinning process.

Although nanofibre production is relatively simple using the electrospinning technique, the spinning mechanism is rather complicated. Electrospinning involves complex electro-fluid-mechanical issues. The theory is not yet fully understood and is still under investigation. Several researchers have presented theoretical models to describe the mechanism of formation for nanofibres [24, 28-31]. However, a general description of the electrospinning process can be described in three stages. The first includes the jet initiation and the extension of the jet along a straight line. When, a high voltage is applied to a polymer fluid (polymer solution or melt) which is held in a syringe. Direct current (DC) power supplies are usually used although the use of alternative current (AC) potentials is also feasible [32]. As a consequence, the polymer fluid is charged either negatively or positively according to the high voltage supply connections. The pendent drop of polymer solution at the nozzle of the spinneret will become highly electrified and the induced charges are eventually distributed over the surface. As a result, the drop will experience two major types of electrostatic forces the electrostatic repulsion between the surface charge and the Coulombic force induced by the external electric field. At a maximum instability of the liquid surface induced by the electrical forces, the liquid drop will experience the formation of fine threads. It was shown that a viscous liquid exists in equilibrium in an electric field when it has the form of a cone with a semi-vertical angle

$\phi=49.3^\circ$ [33]. In other words, a fluid jet is developed when a semi-vertical cone angle attains $\phi=49.3^\circ$. such a cone is now well know as Taylor's cone [34]. The Taylor's cone angle has been independently verified by various groups who experimentally observed that the semi-vertical cone angle just before jet formation is about 50° [20-22]. It is noted that relatively recent publication pointed out that Taylor's cone angle should be 33.5° instead of 49.3° [35].

Another issue related with the initiation of the jet is the strength of the electrostatic field required. It was shown that the critical voltage V_c (in kV) at which the maximum jet fluid instability develops is given by[33]:

$$V_c^2 = 4 \frac{H^2}{L^2} \left(\ln \frac{2L}{R} - 1.5 \right) (0.177 \pi R \gamma) \quad \text{Equation: 3.1}$$

where H is the distance between the electrodes (the needle and the collecting screen), L is the length of the needle, R is the radius of the needle and γ is the surface tension of the fluid.

After its initiation, the jet follows a straight pathway for a short distance depending on the electrospinning parameters and solutions properties.

The thinning and the growth of whipping instability of the jet are not yet complete. From the conventional point of view, when the electric jet fluid accelerates and thins along its trajectory, the radial charge repulsion results in splitting of the primary jet into multiple sub-jets in a process known as "splaying". The final fibre size seemed to be mainly determined by the number of subsidiary jets developed. Recent studies, however, have demonstrated that the key role in reducing the jet diameter from a micrometer to a nanometer is played by a non-axisymmetric or whipping instability, which causes bending and stretching of the jet in very high frequencies [24, 29, 36-38]. Shin et al investigated the stability of electrospinning of polyethylene oxide (PEO) jet using a technique of asymptotic expansion for the equations of electrohydrodynamics in powers of the aspect ratio of the perturbation quantity, which was the radius of the jet and assumed to be small [36-38]. After solving the governing equations thus obtained, they found that the possibility for these three types of instabilities exists. The first is the classical Rayleigh instability, which is axisymmetric with respect to the jet centreline. The second is again an axisymmetric instability, which may be referred to as the second axisymmetric on stability. The third is a non-axisymmetric instability, called "whipping"

instability, mainly by the bending force. Keeping all the other parameters unchanged, the electric field strength will be proportional to the instability level. Namely, when the field is lowest, the Rayleigh instability occurs, whereas the bending (or the whipping) instability corresponds to the highest field [38]. Shin et al. have also experimentally observed that the phenomenon of so-called "inverse cone" in which the primary jet was thought to be split into multiple jets is actually caused by the bending instability. At higher resolution and with shorter electronic camera exposure time, the inverse cone is not due to splitting but as a consequence of small lateral fluctuations in the centreline of the jet. Some similar phenomena were recognised earlier by Reneker et al through their theoretical and experimental work[24].

However, as the jet fluid driven by the electric forces is unstable during its trajectory towards the collector, branching and/or splitting from the primary jet should be possible. In fact, using more advanced experimental set-ups, the phenomena of branching and splitting have been re-realised by various research groups [39, 40]. Shkadov et al. theoretically investigated the excitation conditions of both axisymmetric and non-axisymmetric perturbations of an electrically charged jet [41]. The linearised problem was analysed in terms of the surface frozen charge approximation. Their solutions indicate that there is a possibility of stability control of a moving electrified jet in the longitudinal electric field. By adjusting electrical intensity and liquid properties, the axisymmetric mode instability usually causing the jet decay on drops can be reduced considerably, and the increments of non-axisymmetric modes $m=1$ and $m=2$ are increased where m is the azimuthal wave number. They showed that the non-axisymmetric mode could lead to the longitudinal splitting into two of the initial jet. Regarding the fluid jet diameter, Baumgarten et al. noticed that as the viscosity of the polymer solvent increased, the spinning drop changed from approximately hemispherical to conical. By using equi-potential line approximation calculation, Baumgarten obtained an expression to calculate the radius r_0 of a spherical drop (jet) as follows:

$$r_0^3 = \frac{4\epsilon m_0}{k\pi\sigma\rho} \quad \text{Equation: 3.2}$$

where ϵ is the permittivity of the fluid, m_0 is the mass flow rate at the moment where r_0 is to be calculated, k is a dimensionless parameter related with the electric currents, σ is the electrical conductivity and ρ is the density.

Spivak et al. formulated an electrohydrodynamic model of steady state electrospinning in a single jet, taking into account inertial, hydrostatic, viscous, electric, and surface tension forces [42]. A one-dimensional differential equation for the jet radius, as a function of the distance from the jet tip towards the collecting plat, was derived by averaging physical quantities over the jet cross-section. They compared their theoretical jet radii at various distances up to 60% of the whole jet trajectory with their measured results. Reasonably good agreement was reported.

The jet solidification was investigated by Yarin et al. where they derived a quasi-one dimensional equation to describe the mass decrease and volume variation of the fluid jet due to evaporation and solidification, by assuming that there is no branching or splitting from the primary jet [28]. With an initial weight concentration of 6% and other processing parameters, they calculated that the cross-sectional radius of the dry fibre was 1.31×10^{-3} times of that of the initial fluid jet. Although the solidification rate varied with polymer concentration was implemented, the other issues such as how this rate varies with electrostatic field, gap distance, and how to control the porous dimension and distribution during the solidification have not been clearly addressed.

A brief summarise of the electrospinning process can be describes as follow. The Taylor cone is created by the electrostatic repulsion between the surface charge and the Coulombic force induced by the external electric field. The jet initiation occurs when electrostatic forces overcome the surface tension of the polymer fluid. The jet can be divided in two portions, a straight jet portion and a spiralling jet portion (whipping). A straight jet portion occurs at initiation for a short distance (few cm) depending on the electrospinning parameters and solutions properties. Then the jet undergoes bending instability because of the interaction between the electric field and the surface tension of the jet. As a consequence, the jet starts to stretch and whip and/or branch. Under this process, jet diameter can be greatly reduced from hundred of micrometers to as small as tens of nanometers. In the mean time, the solvent of the polymer solution starts to evaporate which leads to the formation of nanofibres. Finally, nanofibres are deposited onto a grounded collector since the jet is electrically charged (fig: 3.2).

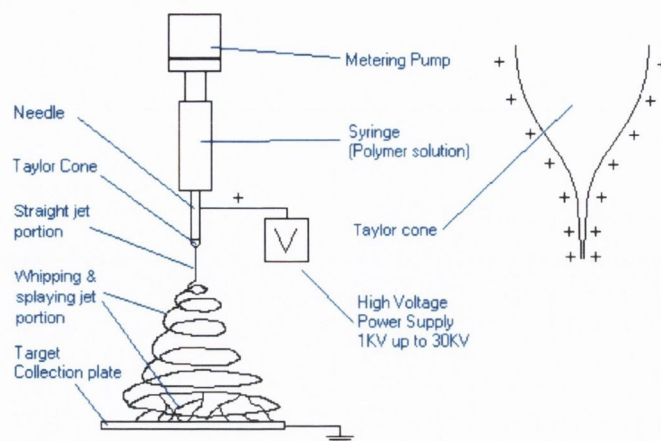


Figure 3.2: Schematic of the electrified jet path and the Taylor cone in the electrospinning process.

3.2.3.3 Electrospinning Parameters.

Many parameters influence the formation and morphology of nanofibres produced by electrospinning. They can be classified in two main categories: polymer solution parameters and processing conditions.

The properties of the polymer solution have the most significant influence on the resulting nanofibres. For example, the molecular weight of the polymer is one of the most critical parameters. For a polymer solution, viscosity is greatly affected by the molecular weight of the polymer. When the electrospinning jet is initiated, it starts to stretch. It is the entanglement of the molecule chains that prevents the jet breaking up. Therefore a low viscosity polymer solution results in droplets rather than nanofibres [43]. If the viscosity is too high, it is more difficult for the solution to pass through the needle. Also, when the viscosity is too high, the solution may dry at the tip of the needle before electrospinning can start [44]. One other effect of the viscosity is the formation of beads along the fibre. As shown in Figure 3.3, a low viscosity results in the presence of many beads. By increasing gradually the viscosity (or the concentration) of the solution, the shape of the beads change from spherical to spindle like until a smooth fibre is obtained [45]. This change in viscosity also results in an increase in the diameter of the nanofibre. High viscosity also discourages secondary jets from spaying from the main jet. Therefore the diameter distribution of nanofibre is more homogenous.

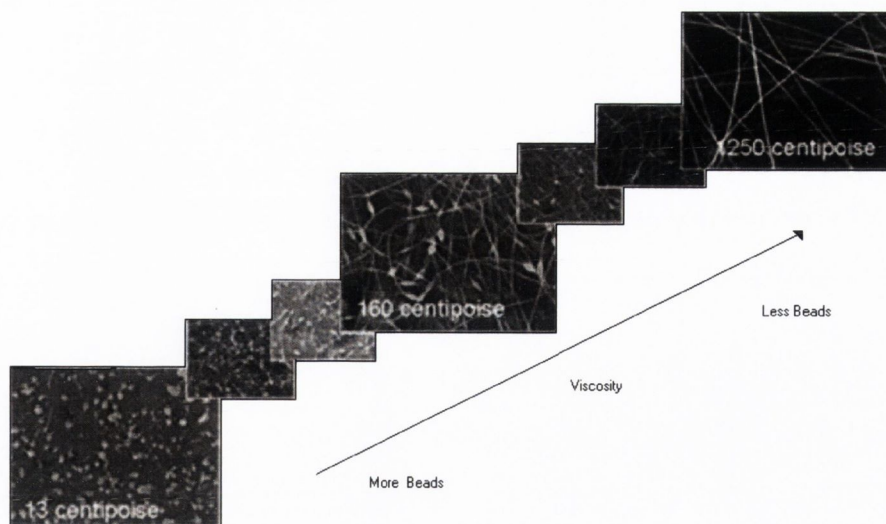


Figure 3.3: SEM of electrospun nanofibres from different polymer concentration solutions [17].

Surface tension is also a critical parameter since the charged solution has to overcome its surface tension to induce the jet formation. Surface tension is also related to the viscosity in the formation of beads along the nanofibres. Surface tension affects the surface area per unit mass of a fluid. At high concentrations, free solvent molecules have a tendency to congregate and adopt a spherical shape due to surface tension. As the viscosity increases, the interactions between the solvent and the polymer also increase. Therefore, during stretching of the jet, solvent molecules tend to spread over the entangled polymer molecules. As a consequence, solvent molecules have less tendency to aggregate under the influence of surface tension (fig: 3.4).

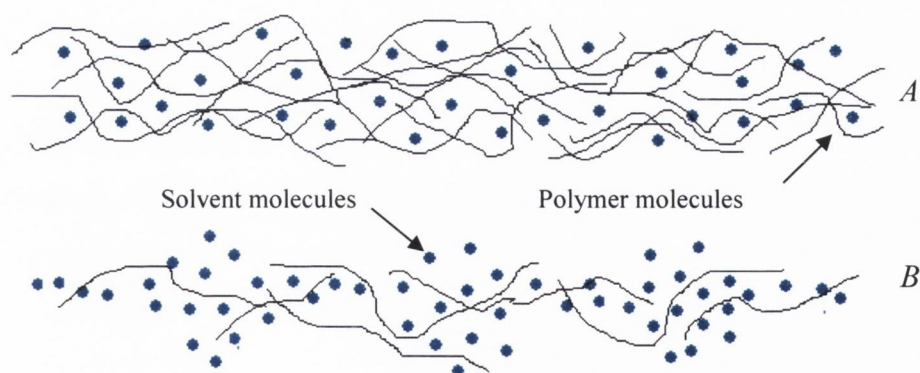
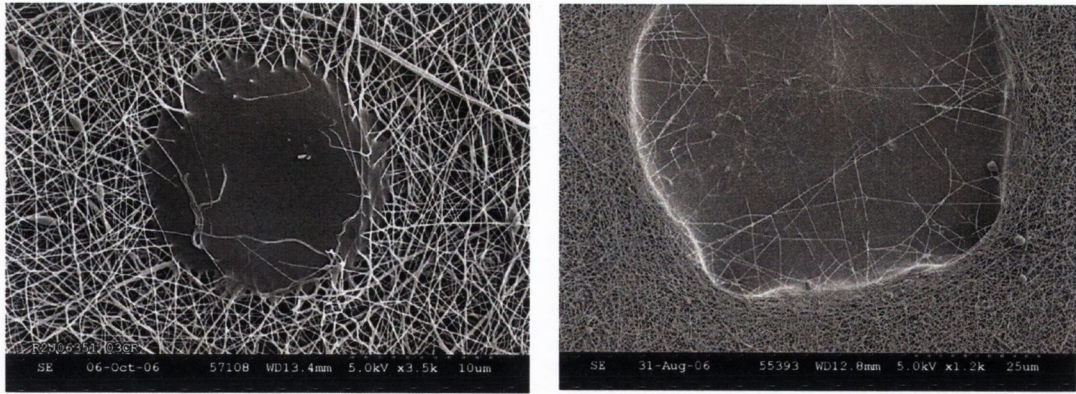


Figure 3.4: Schematic distribution of solvents molecules in high (A) and low (B) polymer viscosity solution [46]

In order to get smoother fibres, solvents such as ethanol can be used to decrease the surface tension of the solvent. Adding surfactant to a solution also improves the reduction of the surface tension [47].

The solution conductivity can also induce major changes in the nanofibre morphology, since stretching of the solution is caused by repulsion of the charges at its surface. Therefore by increasing the solution conductivity, the nanofibre diameter is narrowed. Moreover this increase also leads to smoother fibres since the bead formation occurs when the jet is not fully stretched. A higher conductivity can be achieved by adding small amounts of salt (polyelectrolyte) or by using a solvent with a high dielectric constant (e.g. N,N Dimethylformamide, DMF). However, if a solvent with a very high dielectric constant is added, the solubility of the polymer may also decrease resulting in bead formation [48]. Another effect of increased conductivity in the solution is a greater bending instability. This induces a longer jet path resulting in finer fibres. However, there is a limit to the reduction in the fibre diameter because viscoelastic forces act against the Coulombic forces of the charges for very small diameters [49].

Processing parameters include voltage applied, feed rate, distance between the collector and the needle, needle diameter and type of collector used. However, these parameters have a less significant impact than the solutions parameters mentioned above. Applied voltage and feed rate are closely related for producing nanofibres. This is because it is necessary to generate a stable Taylor cone during the electrospinning process. The applied voltage has to be sufficient to induce charges in the solution to overcome the surface tension and create the Taylor cone. But if the voltage is too high, the jet is accelerated and a greater volume of polymer solution is drawn away from the needle. This can result in a smaller and less stable Taylor cone [44]. Under these conditions, the Taylor cone can also recede into the needle. Therefore, controlling the feed rate of the pump according to the applied voltage is crucial to keep the Taylor cone stable. By increasing the feed rate and keeping the voltage at a constant value, more solution will be drawn away. As a result, the fibre diameter and the bead size will increase. If the feed rate is too fast, nanofibres may not have enough time to evaporate. Therefore, residual solvents may cause fibres to fuse together when deposited onto the collector. A fast rate can even result in droplet formation (fig: 3.5).



a)

b)

Figure 3.5: A fast feed rate results in droplet formation on PVA (a) and PLLA (b) electrospun nanofibres.

The applied voltage also has an effect on the nanofibre morphology. The higher the voltage, the stronger the Coulombic forces in the jet and so the jet solution is more stretched. This results in a decrease in nanofibre diameter [50]. High voltage also increases the rate of evaporation of the solvent and tends to the formation of secondary jets (splaying effect). It has also been reported that at high voltages there is a greater tendency for bead formation [44]. This may be a result of increased instability of the jet as the Taylor cone recedes into the needle.

Depending on the type of collector used, changes can occur in the morphology of the electrospun nanofibre film. Most electrospinning set-ups use a grounded conductive collector. However, non conductive collectors can also be employed. Using a non conductive collector, the charges on the electrospun jet quickly accumulate on the collector. This results in lower packing density fibres compared to those deposited on a conductive collector [32, 51]. A porous collector also decreases the packing density of the deposited nanofibres compared with smooth surface collector. This can be attributed to the diffusion, and rate of evaporation of residual solvent on the fibres. For porous collectors, residual solvent will evaporate at a faster rate due to a higher surface area. A smooth surface may cause an accumulation of solvents around the fibres due to a slower rate of evaporation. As a consequence, the fibres may be pulled together which increases the density of the nanofibre film [51]. Also, the type of collector used can change the morphology of the electrospun film. Using a rotating drum can increase alignment of the nanofibres and decrease the nanofibre diameter because of the extra stretching produced by the rotation.

The internal diameter of the needle has an impact on the electrospinning process. Using a smaller needle diameter tends to reduce the clogging effect and bead formation [52]. Also, nanofibre diameter decreases by using a smaller needle diameter. However, if the needle is too small it may be difficult to extrude the polymer solution and to control the Taylor cone. The distance between the needle and collector has a direct influence on the flight time of the jet and the electric field strength therefore it will influence the morphology of the fibres. If this distance is too small, the electrical field will increase and so too will the speed of the jet. Therefore, the solvent will have less time to evaporate. As a result, excess solvent may cause fibres to merge together on the collector [53]. Another consequence of a small distance is the increase of fibre diameter because less stretching is occurring. Finally, as a small distance increases the electric field, this may also encourage bead formation because of the increase of the jet instability.

3.2.3.4 Electrospinning Potential Applications.

A lot of research is being done to improve and control the morphology and pattern deposition of nanofibres by electrospinning. The growing interest in electrospun nanofibres is based on their unique properties such as a very high surface area, low density (porous structure), and the variety of polymers which can be used. The most promising applications are for filter media, drug delivery, protective clothes and as a scaffold for tissue engineering. A larger exhaustive application list is presented in Figure 3.6.

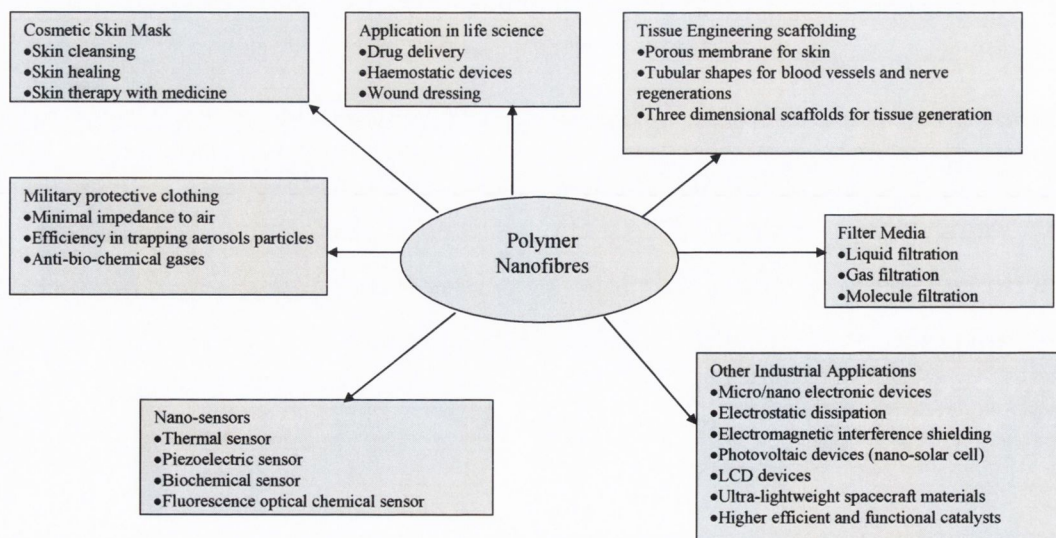


Figure 3.6: Potential applications for polymer electrospun nanofibres [17].

3.3 Techniques of Characterisation.

3.3.1. Fourier Transform Infrared Spectroscopy (FTIR).

Infrared spectrometry is a method which is extensively used for the investigation of polymer structure and the analysis of functional groups. This technique is capable of qualitative identification of unknown materials being investigated [54-57]. It is also capable of quantitative measurement of components in a complex mixture [54]. Infrared radiation covers the electromagnetic radiation between visible and microwaves regions (14000 cm^{-1} - 200 cm^{-1}). The infrared region (IR) can be divided into three: near infrared region (NIR, 14000 cm^{-1} - 4000 cm^{-1}), mid infrared region (4000 cm^{-1} - 700 cm^{-1}) and far infrared region (700 cm^{-1} - 200 cm^{-1}). However, mid IR is used more for polymer investigation because these are the wavelengths where the interatomic bonding of organic compounds absorb infrared radiation. This range is divided two parts, the group frequency region (4000 cm^{-1} - 1300 cm^{-1}) and the "fingerprint" region (1300 cm^{-1} - 700 cm^{-1}). The group frequency region includes the principle absorption bands which refer to vibration units of only two atoms of a molecule. These units are more or less dependent only on the functional group giving the absorption and not the complete molecular structure. The fingerprint region includes single bond stretching frequencies and bending vibrations of polyatomic systems, which involve motions of bonds linking a subsistent group to remainder of the molecule. However, two primary conditions must be fulfilled for infrared absorption to occur. First, the energy of the radiation must coincide with the energy difference between excited and ground states of the molecules. Radiant energy will be absorbed by the molecule, increasing its natural vibration. Second, the vibration must entail a change in the electrical dipole moment. Stretching vibrations involve changes in the inter-atomic distance along the bond axis, whereas other vibrations involve changes in the angle between two bonds. In addition to vibrations, interactions between vibrations can occur if the vibration bonds are joined to a single, central atom. This is called vibrational coupling. Studies of the chemical nature of polymers can be carried out with IR such as polymerisation kinetics cure studies [55-57], and average molecular weight determination [55, 57]. IR can also be used to assess physical properties of a polymer, such as crystallinity and molecular orientation [55-57]. The FTIR machine used in these studies was a Nicolet FTIR spectrometer.

3.3.2 Raman Spectrometry.

Raman spectroscopy is a form of vibrational spectroscopy discovered by Sir C.V. Raman [58]. This technique involves the illumination of a sample with a laser light. When the light is scattered from a molecule most photons are elastically scattered. The scattered photons have the same energy and wavelength as the incident photons. However, a small fraction of light (approximately 1 in 10^7 photons) is scattered at optical frequencies different from the frequency of the incident photons. This inelastic scattering is called the Raman effect. Raman scattering takes place with a change in vibrational, rotational or electronic energy of a molecule. The effect occurs when a photon interacts with the molecule's electric dipole. In quantum mechanics, the scattering is described as an excitation to a virtual state lower in energy than a real electronic transition with almost immediate de-excitation and a change in vibrational energy. Raman scattering can be further separated into Stokes and anti-Stokes radiation as shown in Figure 3.7.

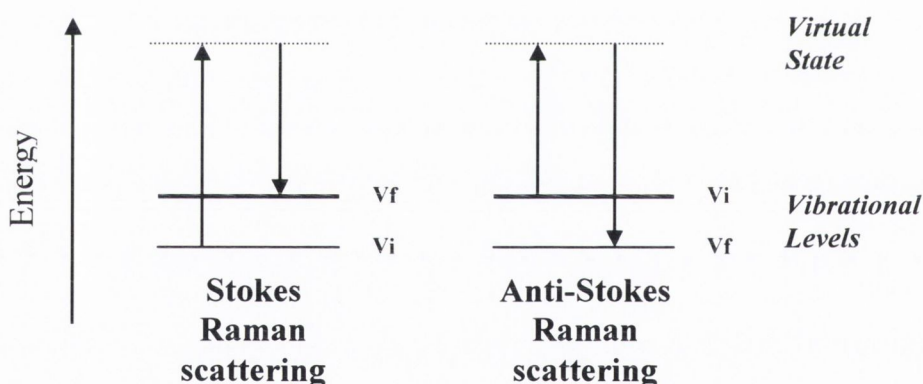


Figure 3.7: Energy level diagrams for Stokes Raman scattering and Anti-Stokes Raman scattering.

At room temperature the thermal population of excited vibrational states is very low. Therefore, the initial state is the ground state and scattered photons will have a lower energy than the exciting photon. This effect is known as Stokes Raman scattering. However, if the photon is scattered from an atom or a molecule in an excited state, its energy will be greater than the incident photon. This is known as anti-Stokes Raman scattering.

A Raman spectrum is a plot of the scattered light intensity versus the energy difference between the incident and scattered photons. Numerically, the energy difference between the initial and the final vibrational levels (ν), or Raman shift can be calculated as follows.

$$\nu = \frac{1}{\lambda_{\text{incident}}} - \frac{1}{\lambda_{\text{scattered}}} \text{ (cm}^{-1}\text{)} \quad \text{Equation: 3.3}$$

where $\lambda_{\text{incident}}$ and $\lambda_{\text{scattered}}$ are the wavelengths of the incident and Raman scattered photons, respectively. The Stokes Raman scattering intensity will generally be higher than anti Stokes Raman intensity at room temperature since the intensity is proportional to the population of the initial state of the illuminated molecules.

Raman spectroscopy is a non-destructive method which does not require any sample pre-treatment. Furthermore, Raman spectroscopy was used in this thesis because it is a useful tool for the characterisation of CNTs [59]. Indeed, Raman spectroscopy provides very distinctive and relatively simple spectra of carbon nanotubes. The Raman spectrum of CNTs shows three distinct regions. The first characteristic part of the spectrum called the Radial Breathing Modes (RBM) occurs between 100 and 400 cm^{-1} . The frequency of the RBM is directly linked to the reciprocal of the nanotube diameter (d). In the case of an isolated SWNT this relation can be described as follows [60, 61].

$$\omega = \frac{244}{d} \text{ (cm}^{-1}\text{)} \quad \text{Equation: 3.4}$$

The RBM region is not as defined for MWNTs due to the interference of concentric shells. The next two regions of interest are called the D band (disorder band) and G band (Graphitic band). These peaks occur between 1300 and 1360 cm^{-1} , and at 1580 cm^{-1} respectively. The D band comes from disorder in sp^3 systems and can be used as a guide to the amount of defects and impurities in the nanotube sample. The G band centred at $\sim 1580 \text{cm}^{-1}$ is due to the Raman active E_{2g_2} modes in sp^2 carbon systems, which corresponds to in-plane graphitic vibrations. The G band is actually composed of two separate bands, the G+ band, which is associated with vibrations along the CNT axis and the G- band which is associated with vibrations perpendicular to the axis. In the case of MWNTs the G+/G- splitting is weak due to the overlap of concentric shells. For SWNTs and thin MWNTs there is less interference from neighbouring shells and splitting is evident. The ratio of integrated areas under the D band and G band can be used as a qualitative method to measure the quality of nanotubes [62]. The smaller this ratio (I_G/I_D), the higher defects (or impurities) present in the CNT sample.

In the following chapters, Raman spectroscopy was used in order to assess the dispersion of nanotubes within various polymers matrices. These measurements were performed with a HORIBA Jobin Yvon Labram HR Raman spectrometer with a green laser light at 533 cm^{-1} .

3.3.3 Thermogravimetric Analysis.

Thermogravimetric Analysis (TGA) is a quantitative technique in which the mass of the sample is measured as a function of temperature. TGA can be done under either air or nitrogen purge. TGA measurements provide useful information about the materials under investigation such as:

- Compositional analysis of multi-component materials or blends
- Thermal stabilities
- Oxidative stabilities
- Estimation of product lifetimes
- Decomposition kinetics
- Effects of reactive atmospheres on materials
- Moisture and volatile content.

In this thesis, TGA curves were obtained by using a Pyris 1 thermogravimetric analyser from Perkin Elmer. The main aim was to assess how fillers like carbon nanotubes were able to induce changes in the thermal degradation of organic polymers investigated.

3.3.4 Differential Scanning Calorimetry.

Differential Scanning Calorimetry (DSC) curves reflect changes in the energy of the system under investigation. These changes may be either physical or chemical. DSC measures the heat required to maintain a constant temperature in the sample, versus an appropriate reference material. Enthalpy changes due to a change in the polymer state can be determined. A number of important physical changes in a polymer can also be characterised using DSC, including the glass transition temperature (T_g), the crystallisation temperature (T_c), the melt

temperature (T_m), and the degradation or decomposition temperature (T_D). A typical DSC trace showing these transitions is presented in the Figure 3.8.

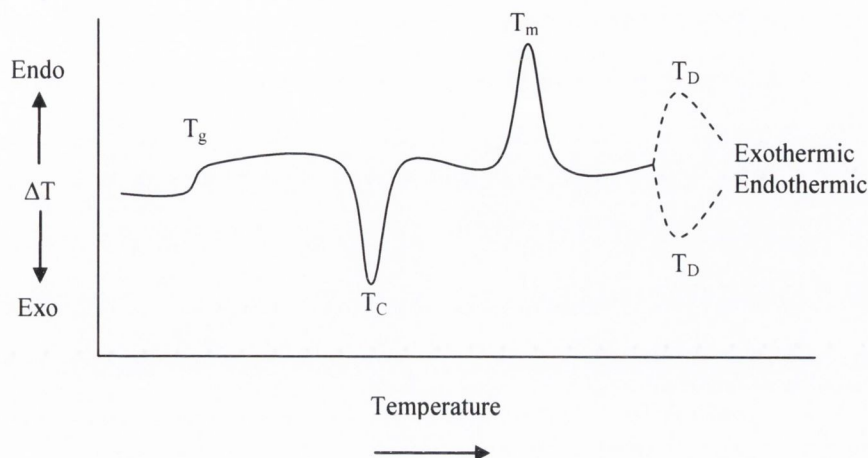


Figure 3.8: DSC curve showing several transition types.

Two different types of DSC machine are available: heat flux and power compensation. A Perkin Elmer Diamond DSC power compensation instrument was used in our studies. DSC contains two identical pans, one containing the material to be tested and the other acts as a reference pan. A schematic of the two systems is shown in the Figure 3.9.

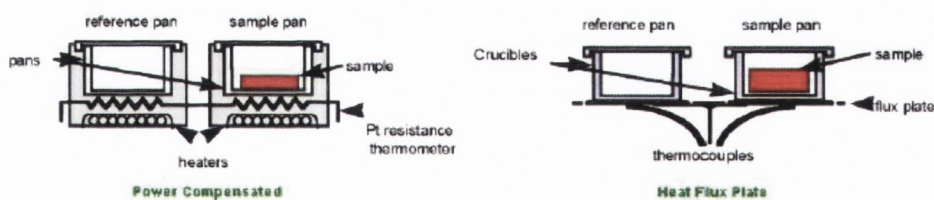


Figure 3.9: Illustration of the two types of DSC machines [63].

In the case of power compensation, both pans are heated slowly by separated coupled furnaces in order to keep the same temperature in each pan. The pan containing the sample requires a different amount of heat to maintain a constant temperature rise relative to the reference pan. This difference is directly related to the heat capacity, C_p of the sample. This is the amount of heat required to raise the temperature by one degree per unit mass.

For polymers, the first thermal transition T_g corresponds to the temperature at which the polymer chains of the amorphous regions undergo a transition from a glassy state to a rubbery state. This represents a second order transition with no transfer of heat between the polymer and the surroundings. However a variation of the heat capacity, ΔC_p occurs. For semi-crystalline polymers, two other thermal transitions occur which are represented by an exothermic and endothermic peaks. The exothermic peak, T_c is called a cold crystallisation peak. At this temperature, the system gains enough energy to allow polymer chains to organise themselves into ordered structural forms, i.e. crystalline structure. This involves a transfer of heat between the polymer and the surroundings. This transition appears in the DSC scan if the polymer has not been fully crystallised before the first heat step. As the temperature increases further, the polymer reaches its melting temperature (T_m). This transition requires energy and is characterised by an endothermic peak. If a quick cooling step, called quench cooling, takes place after T_m , this crystallisation will occur again during the following heat step. At the decomposition temperature, T_D , an irreversible change occurs where polymer chains start to degrade due to the breaking of the bonds of the side chains and the backbone chain.

The percentage of crystallinity of the polymer can be determined by considering the area of the T_c and T_m peaks. The enthalpy required to either melt (ΔH_m) or crystallise (ΔH_c) a sample can be calculated by the integration of the respective peaks. The crystalline fraction (χ) of a sample can then be calculated using the following equation (Eq 3.3). This equations assumes knowing the enthalpy of melting of a theoretical 100 % crystalline this sample, $\Delta H_{100\%}$.

$$\chi = 100 \times \frac{\Delta H_m}{\Delta H_{100\%}} \quad \text{Equation: 3.5}$$

3.3.5 Transmission Electron Microscopy (TEM).

Transmission Electron Microscopy uses an electron gun to produce a stream of electrons. The stream is then focused into a thin coherent beam using a pair of condenser lenses. The first lens determines the general spot size of the beam which is incident on the sample. The second lens actually changes the size of the spot on the sample. The spot size range goes from a wide dispersed spot to a pinpoint beam. The beam is restricted by a

condenser aperture which removes high angle electrons before they reach the sample. Part of the beam will be transmitted by the sample and this is then focused by an objective lens into an image. After the sample, optional objective and selected area apertures can be used to further restrict the beam. The aim of the optional objective aperture is to enhance contrast by blocking out high angle diffracted electrons. The selected area aperture is used for electron diffraction measurements. The image is then passed down the column through the intermediate and projector lenses and finally strikes CCD detector. This allows the user to see the image. The darker part of the image corresponds to the area of the sample where fewer electrons were transmitted. This is where the sample is thicker (or more dense). The lighter areas of the image represent portions where more electrons were transmitted because the sample was either thinner, or less dense.

3.3.6 Scanning Electronic Microscopy (SEM).

Similar to a TEM set up, a scanning electronic microscope uses an electron gun to produce a stream of electrons. The stream is then focused by a condenser lens to form the beam, and also to limit the amount of current in the beam. The beam is then constricted by a condenser aperture to eliminate high angle electrons. A second condenser lens focuses the electrons into a thin, tight, coherent beam. A user selectable objective aperture further eliminates high angle electrons from the beam. Subsequently, a set of coils “scan” or “sweep” the beam in a grid fashion, dwelling on points for a period of time determined by the scan speed. A final lens, the objective, focuses the scanning beam onto the sample. When the beam strikes the sample and dwell for few microseconds, interactions occur inside the sample. These interactions are detected. The number of electrons scattered by each point is proportional to the brightness of the pixel on the display.

In our work, all our samples were gold/palladium coated. Samples were investigated with an accelerating voltage of 5 kV and a beam current of $\sim 10 \mu\text{A}$. Gold coating is used to help prevent “charging” on surfaces that are not electrically conducting, such as silicon dioxide. This effect occurs when electrons from the microscope beam cannot be dissipated to earth, and thus “pool” on the nonconductive surface. This accumulated charge can then scatter lower energy secondary electrons, causing a loss in fine detail in the resultant image.

3.3.7 Tensile Testing.

One of the most popular techniques used to characterise the mechanical properties of a sample is the stress-strain in tension mode. With this technique, the specimen is elongated at a constant rate and the applied load is measured simultaneously. The resulting stress-strain plot shows many mechanical features of the tested specimen such as its elastic and/or plastic behaviour. For example, thermoplastic polymers present a large elastic behaviour followed by a small plastic deformation. Alternatively, elastomers show a small elastic behaviour followed by a large plastic deformation. Moreover, the elastic modulus or Young's modulus (Y) can also be determined from the stress-strain curves, as the slope of the initial region where the stress (σ) is linearly proportional the strain (ϵ). Other useful mechanical parameters are the ultimate tensile strength, strain-at-break and toughness. The ultimate tensile strength corresponds to the maximum stress that can be sustained by the sample in tension. Strain-at-break represents the maximum strain of the specimen before fracture. Toughness is a measure of the ability of the sample to absorb energy before fracture. Toughness is calculated from the area under the stress stain curve. All the tensile measurements achieved in this work were carried out using a Zwick tensile tester with a 100N load cell ($\pm 0.1N$) (fig 3.10). For all the studies, measurements were achieved on small rectangular samples structure. Dogbone structure was not used because of the composites film process (drop cast processing and electrospinning). Also in the thesis we used engineering stress and strain and only samples broken away from the grips and presenting no slippage were kept for analyses. All the mechanical parameters investigated in the following chapters are associated with their standard errors.

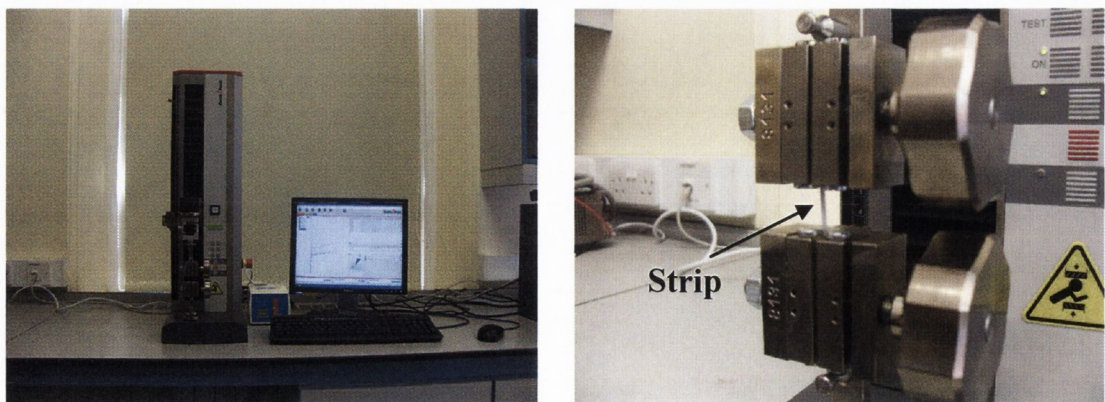


Figure 3.10: Composites tested using the Zwick tensile tester.

3.3.8 Atomic Force Microscopy (AFM).

Atomic force microscopy was used in this work in order to assess the mechanical properties of single nanofibres of PVA CNT composites. This technique was invented by Binnig, Quate and Gerber in 1986 [64]. AFM is a very high resolution technique which can reach the sub-nanometer scale. In AFM, a constant force is maintained between a probe and a sample while the probe is rastered across the surface of the sample. By monitoring the deflections of the probe as it is scanned across the surface, a three dimensional image of the surface is constructed. As shown in Figure 3.11, an AFM set-up consists of a sharp probe tip (around 20 nm at its apex) attached to a flexible cantilever. The investigated sample is attached to a piezoelectric scanner tube. Interatomic forces between the probe tip and the sample surface cause the cantilever to deflect as the sample's surface topography (or other properties) change. A laser light reflected from the back of the cantilever measures the deflection of the cantilever. This information is then fed back to a computer.

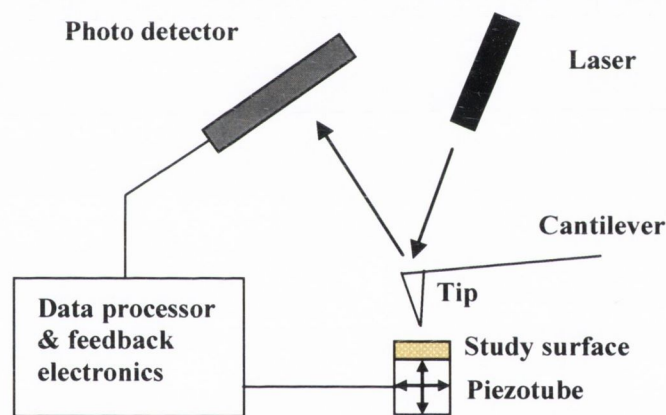


Figure 3.11: Diagram of an AFM set up.

The three main modes of interaction between the tip and the sample are contact mode, tapping mode and non-contact mode [65].

Lateral Force Microscopy Mode (LFM) was used to measure the mechanical properties of single nanofibres composites. During a scanning contact mode, a LFM uses a four quadrant photo-diode to enable measurement of the torsional deformation of the cantilever under X-Y-Z closed loop control. The lateral deformation depends on contact (lateral forces) acting on the tip.

Initially PVA CNT composite nanofibres were electrospun over trenches pre-patterned onto SiO₂ substrates (fig: 3.12). Trenches were fabricated by focused ion beam milling and were 5

μm wide and $0.5 \mu\text{m}$ deep [66]. The electrospinning parameters used for the deposition will be explained in more detail in chapter 6.

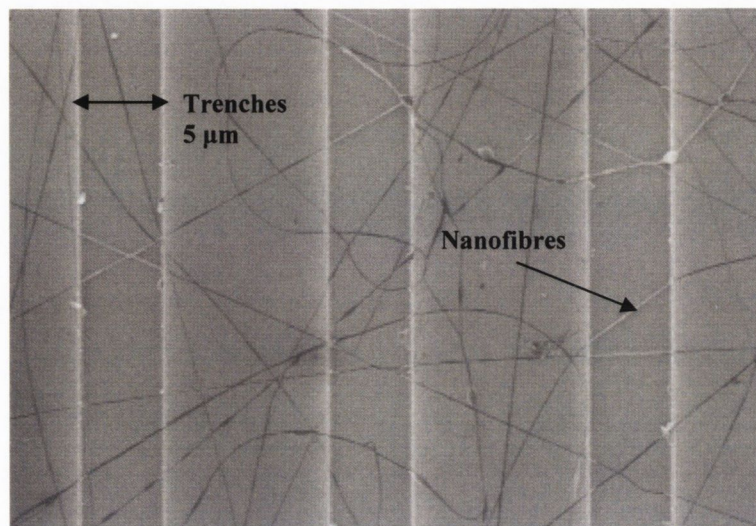


Figure 3.12: SEM image of nanofibres onto SiO_2 trenches.

Afterwards, nanofibres which span perpendicularly across trenches were mechanically fixed by electron beam induced deposition of platinum lines [66, 67]. The resulting structure was then subjected to lateral force microscopy loading. These measurements were carried out using a Digital Instrument Nanoman system with closed loop x-y-z scanner. The AFM tip was positioned 100- 300 nm below the plane of the substrate [66]. It was then programmed to sweep in the XY plane of the substrate with the axis of the cantilever aligned parallel to the nanofibre axis. The speed of the tip was typically 20 nm/s. During the manipulation of the tip, the lateral and normal deflections of the cantilever were monitored using a four-quadrant photodiode (fig: 3.13). The corresponding force – displacement was then recorded.

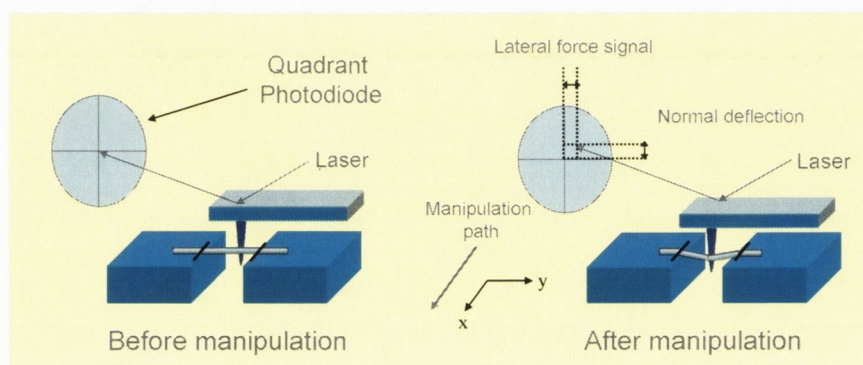


Figure 3.13: Schematic of a fixed nanofibre in a lateral test with AFM tip [68].

All measurements continued until failure of the nanofibre occurred. The AFM pictures below (fig 3.14) show the pinned nanofibres over a trench before and after manipulation with the tip.

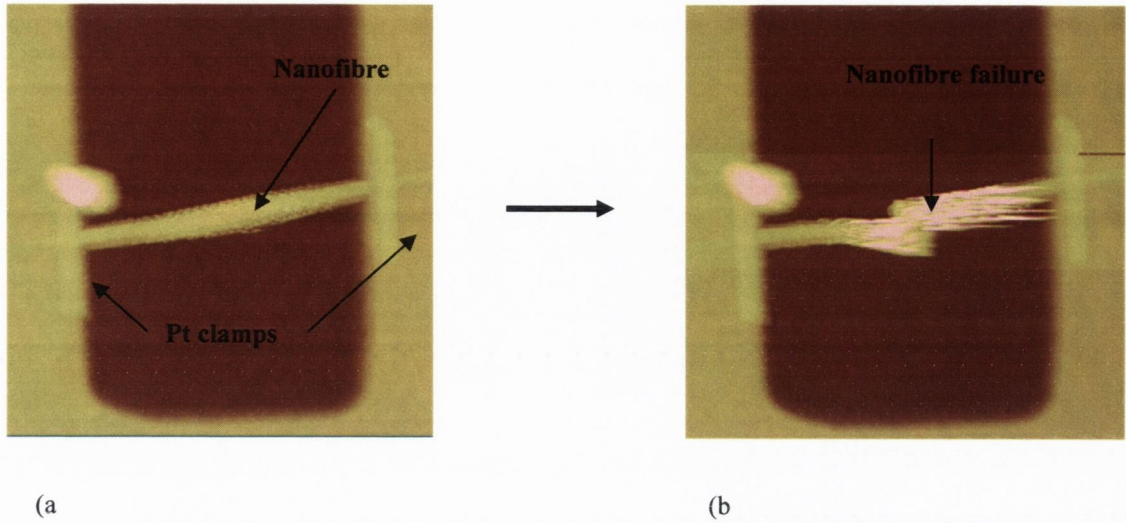


Figure 3.14: AFM pictures of the nanofibre before (a) and after lateral bending test (b).

The force-displacement curve for PVA nanofibre composites display a non linear elastic deformation followed by a brittle failure (Fig 3.15). This behaviour is typical for all the PVA nanofibres composites investigated by this technique.

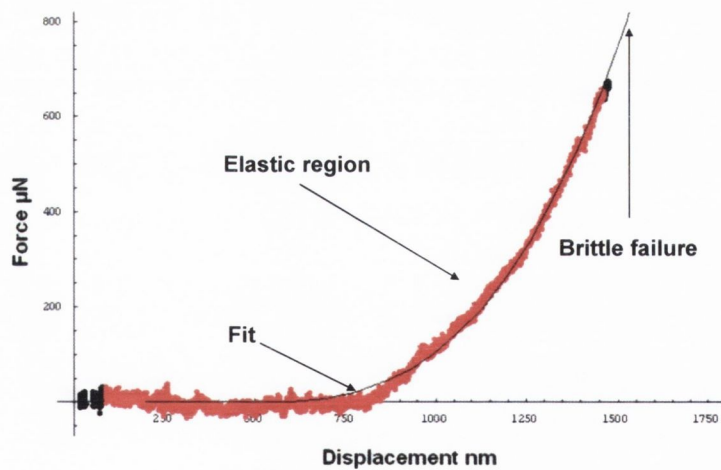


Figure 3.15: Force-displacement curve for a single nanofibre of PVA composite.

For this work, electrospun fibres deposition on SiO_2 substrates was achieved in our laboratory. All AFM preparations, measurements and calculations of Young's modulus and ultimate

tensile strength of single nanofibres were achieved by Dorothée Almecija from the Centre for Research on Adaptive Nanostructures and Nanodevices (CRANN) and the School of Chemistry in Trinity College of Dublin (IRELAND).

3.4 Mechanical Reinforcement of Composites Using Filler.

Many models have been developed to understand the mechanical reinforcement of composites using fibres [69]. In the case of composites based on polymers and carbon nanotubes, two models are commonly used in the literature because of their relative simplicity. These are the rule of mixtures [70] and the Halpin-Tsai model [71].

3.4.1 Rule of Mixtures.

In this model, it is assumed that the reinforcing fibres are aligned and span the full length of the composite. A second assumption is that the matrix and the fibres are very well bonded together. Hence, the Poisson's ratio and strain are equal for both the fibre and the matrix. Under these circumstances, the composite tensile modulus parallel, $Y_{c\parallel}$, and perpendicular $Y_{c\perp}$ to the fibre direction are:

$$Y_{c\parallel} = V_f Y_f + (1 - V_f) Y_m \quad Y_{c\perp} = \frac{Y_m Y_f}{V_f Y_m + (1 - V_f) Y_f} \quad \text{Equation: 3.6}$$

where Y_f is the fibre modulus, Y_m is the matrix modulus and V_f is the fibre volume fraction. This represents the well known rule of mixtures [70].

3.4.2 Shear-Lag Theory.

Shear-lag model was originally developed by Cox [72] for predicting the elastic strength of two-phase composites in which the strong phase (fibre) is embedded in a

continuous weak phase (matrix). This theory assumes that if no slip occurs on the phase interfaces, the presence of the fiber redistributes the stresses and strains within the composite material and has an effect of transferring load from the matrix to the fibre. This process has two corollaries: a shear stress occurs at the fiber-matrix interface, and the harder phase carries a comparatively greater part of the stress, while the soft phase tends to take the greater part of the strain (with reference to the volume fraction ratio). Like most analytical and numerical and numerical models on the mechanical properties of composite materials, the shear lag model is based on the idealized assumption that there is no slip on the phase interfaces. It means that the interface is a mathematical surface across which material properties change discontinuously, while stress and displacement are continuous across the interface. When perfect bonding between fibre and matrix is assumed, interface properties and structures are eliminated. Consequently, the mechanical properties are determined solely by the properties of the constituent materials. The interest of this model is that it can allow the calculation of the stress distribution in both the fibre and the matrix.

The rule of mixtures given in the previous section only applies where the fibres are as long as the matrix. Therefore, modification of the rule of mixtures is required to take into account fibres shorter than the matrix such as carbon nanotubes. In this case, the fibre-matrix stress transfer has to be considered with the shear lag theory. When the matrix is under stress, the maximum stress transferred to the fibre is described by the interfacial stress transfer, τ . The stress transferred scales with fibre length, l , until a critical length, l_c , the stress transfer will be high enough to break the fibre. For a hollow cylinder like CNTs, this critical length is given by:

$$l_c = \frac{\sigma_f D}{2\tau} \left(1 - \frac{D_i^2}{D^2} \right) \quad \text{Equation: 3.7}$$

where σ_f is the fibre strength, D and D_i are the fibre external and internal diameters, respectively [73]. Short fibres carry load less efficiently than long fibres. This consideration was first developed by Cox [72] to modify the rule of mixture using the shear lag analysis given by:

$$Y_c = Y_m(1 - V_f) + Y_f V_f \left(1 - \frac{\tanh \frac{\beta l}{2}}{\frac{\beta l}{2}} \right) \quad \text{Equation: 3.8}$$

where the last term in brackets is described as fibre length efficiency factor, l is the fibre length and β , which governs the rate of stress build up at the fibre ends, is:

$$\beta = \frac{l}{r} \left[\frac{Y_m}{Y_f (1 + \nu) \ln \left(\frac{R}{r} \right)} \right]^{1/2} \quad \text{Equation: 3.9}$$

where Y_m is the matrix modulus, ν is the Poisson's ratio, r is the fibre radius and $2R$ the mean inter-fibre spacing. For a square fibre packing system, the inter-fibre spacing is related to the volume fraction by:

$$R = r \sqrt{\frac{\pi}{4v_f}} \quad \text{Equation: 3.10}$$

So that β may be written as

$$\beta = \frac{1}{r} \sqrt{\frac{Y_m}{E_f (1 + \nu) \ln \sqrt{\frac{\pi}{4v_f}}}} \quad \text{Equation: 3.11}$$

Several assumptions were made. The fibre and the matrix remain elastic in their mechanical response. The interface between the fibre and the matrix is perfect and no axial force is transmitted through the fibre ends.

However, in many situations, the fibres may not be aligned. For randomly oriented fibres in the matrix, this model can be further modified using the Krenchel orientation efficiency factor [74]. In this case, the composite modulus for non-aligned short fibres is given by:

$$Y_c = (\eta_0 \eta_1 Y_f - Y_m)V_f + Y_m \quad \text{Equation: 3.12}$$

where η_0 is the Krenchel orientation efficiency factor defined in equation 3.12.

$$\eta_0 = \frac{\sum_n a_{fn} \cos^4 \alpha_n}{\sum_n a_{fn}} \quad \text{and} \quad \sum_n a_{fn} = 1 \quad \text{Equation: 3.13.}$$

For aligned, aligned in plane and randomly oriented fibres, the η_0 values are respectively 1, 3/8 and 1/5 [74] and a_{fn} is the ratio between the cross-sectional area presented by a group of fibres orientated at an angle α_n to the applied load direction and the total area of all the fibres at a given cross section of the composite. The number of groups are designated by $n=1,2,3,\dots,n$ [75].

The Krenchel model for short fibre composites has been employed in recent studies to describe the mechanism of reinforcement in various polymer matrixes with carbon nanotubes [12, 76-80].

3.4.3 Halpin-Tsai Theory.

This model, developed by Halpin and Tsai [81] for continuous fibre composites, is a further modification of the rule of mixtures [75]. It describes systems which take into account the orientation and the length of the fibres. For aligned fibres, the composites modulus is given by:

$$Y_c = Y_m \frac{(1 + \zeta \eta V_f)}{(1 - \eta V_f)} \quad \text{Equation: 3.14}$$

where $\zeta = 2l/D$ and $\eta = \frac{Y_f/Y_m - 1}{Y_f/Y_m + 1}$ Equation: 3.15

For randomly orientated fibres the composite modulus is expressed as:

$$Y_c = Y_m \left[\frac{3}{8} \left(\frac{1 + \zeta \eta_L V_f}{1 - \zeta \eta_L V_f} \right) + \frac{5}{8} \left(\frac{1 + 2\eta_T V_f}{1 - \eta_T V_f} \right) \right] \quad \text{Equation: 3.16}$$

$$\text{where } \eta_L = \frac{Y_f / Y_m - 1}{Y_f / Y_m + \zeta} \text{ and } \eta_T = \frac{Y_f / Y_m - 1}{Y_f / Y_m + 2} \quad \text{Equation: 3.17}$$

The Halpin-Tsai model has been successfully applied for various polymer matrices including carbon nanotubes [82, 83]. However, this model has some limitation since it fits data very well at low volume fractions of fillers, but underestimates the Young's modulus at high volume fractions [69].

In summary, both models can be used to predict the Young's modulus taking into account volume fraction, the aspect ratio and the orientations of the fibres. Furthermore, these models suggest a linear increase of the modulus for low volume fractions [1]. However, in reality the stress transfer is rarely very high between the filler and the matrix. As a consequence neither model applies in many cases. To overcome this issue, an interesting method to evaluate the reinforcement is to calculate dY_c/dV_f for a low content of filler material. This is a useful parameter since it takes in account both the magnitude of the increase in the Young's modulus and the amount of filler required to achieve this reinforcement. Finally, this also allows the comparison of results between various studies [1].

3.5 Summary.

In this chapter, various processing techniques have been presented to fabricate polymer carbon nanotubes composites which we characterised in this thesis. These are in situ polymerisation, solution mixing and electrospinning. We also presented the thermal, spectroscopical, morphological and mechanical techniques used to assess the impact of the carbon nanotubes included in the biopolymers.

3.6 References.

1. Coleman, J.N., et al., *Small but strong: A review of the mechanical properties of carbon nanotube-polymer composites*. Carbon, 2006. 44(9): p. 1624-1652.
2. Coleman, J.N., et al., *Improving the mechanical properties of single-walled carbon nanotube sheets by intercalation of polymeric adhesives*. Applied Physics Letters, 2003. 82(11): p. 1682-1684.
3. Lahiff, E., et al., *Selective Positioning and Density Control of Nanotubes within a Polymer Thin Film*. Nano Lett., 2003. 3(10): p. 1333-1337.
4. Vigolo, B., et al., *Macroscopic Fibers and Ribbons of Oriented Carbon Nanotubes*. Science, 2000. 290(5495): p. 1331-1334.
5. Ko, F., et al., *Electrospinning of continuous carbon nanotube-filled nanofiber yarns*. Advanced Materials, 2003. 15(14): p. 1161-+.
6. Jia, Z., et al., *Study on poly(methyl methacrylate)/carbon nanotube composites*. Materials Science and Engineering A, 1999. 271(1-2): p. 395-400.
7. Velasco-Santos, C., et al., *Improvement of Thermal and Mechanical Properties of Carbon Nanotube Composites through Chemical Functionalization*. Chem. Mater., 2003. 15(23): p. 4470-4475.
8. Putz, K.W., et al., *Elastic modulus of single-walled carbon nanotube/poly(methyl methacrylate) nanocomposites*. Journal of Polymer Science Part B: Polymer Physics, 2004. 42(12): p. 2286-2293.
9. Kumar, S., et al., *Synthesis, Structure, and Properties of PBO/SWNT Composites*. Macromolecules, 2002. 35(24): p. 9039-9043.
10. Zhao, C., et al., *Synthesis and characterization of multi-walled carbon nanotubes reinforced polyamide 6 via in situ polymerization*. Polymer, 2005. 46(14): p. 5125-5132.
11. Seamus A. Curran, et al., *A Composite from Poly(m-phenylenevinylene-co-2,5-dioctoxy-p-phenylenevinylene) and Carbon Nanotubes: A Novel Material for Molecular Optoelectronics*. Advanced Materials, 1998. 10(14): p. 1091-1093.
12. Coleman, J.N., et al., *High Performance Nanotube-Reinforced Plastics: Understanding the Mechanism of Strength Increase*. Advanced Functional Materials, 2004. 14(8): p. 791-798.
13. J. N. Coleman, et al., *Phase Separation of Carbon Nanotubes and Turbostratic Graphite Using a Functional Organic Polymer*. Advanced Materials, 2000. 12(3): p. 213-216.
14. Giordani, S., et al., *Debundling of single-walled nanotubes by dilution: Observation of large populations of individual nanotubes in amide solvent dispersions*. Journal of Physical Chemistry B, 2006. 110(32): p. 15708-15718.
15. Dalmas, F., et al., *Multiwalled carbon nanotube/polymer nanocomposites: Processing and properties*. Journal of Polymer Science Part B: Polymer Physics, 2005. 43(10): p. 1186-1197.
16. Formhals, A., *Process and apparatus for preparing artificial threads*, U.S. Patent, Editor. 1934: United States.
17. Huang, Z.-M., et al., *A review on polymer nanofibers by electrospinning and their applications in nanocomposites*. Composites Science and Technology, 2003. 63(15): p. 2223-2253.
18. Jayaraman, K., et al., *Recent Advances in Polymer Nanofibers*. Journal of Nanoscience and Nanotechnology., 2004. 4: p. 52-65.

19. Baumgarten, P.K., *Electrostatic spinning of acrylic microfibers*. Journal of Colloid and Interface Science, 1971. 36(1): p. 71-79.
20. L. Larrondo, R.S.J.M., *Electrostatic fiber spinning from polymer melts. I. Experimental observations on fiber formation and properties*. Journal of Polymer Science: Polymer Physics Edition, 1981. 19(6): p. 909-920.
21. L. Larrondo, R.S.J.M., *Electrostatic fiber spinning from polymer melts. II. Examination of the flow field in an electrically driven jet*. Journal of Polymer Science: Polymer Physics Edition, 1981. 19(6): p. 921-932.
22. L. Larrondo, R.S.J.M., *Electrostatic fiber spinning from polymer melts. III. Electrostatic deformation of a pendant drop of polymer melt*. Journal of Polymer Science: Polymer Physics Edition, 1981. 19(6): p. 933-940.
23. Reneker, D.H. and I. Chung, *Nanometre diameter fibres of polymer, produced by electrospinning*. Nanotechnology, 1996. 7: p. 216-223.
24. Reneker, D.H., et al., *Bending instability of electrically charged liquid jets of polymer solutions in electrospinning*. Journal of Applied Physics 2000. 87(9): p. 4531-4547
25. Boland, E.D., et al., *Tailoring tissue engineering scaffolds using electrostatic processing techniques: a study of poly(glycolic acid) electrospinning*. Journal of Macromolecular Science, Part A, 2001. 38(12): p. 1231 - 1243.
26. Theron, A., E. Zussman, and A.L. Yarin, *Electrostatic field-assisted alignment of electrospun nanofibres*. NANOTECHNOLOGY, 2001. 12: p. 384-390.
27. Li, D., Y. Wang, and Y. Xia, *Electrospinning of Polymeric and Ceramic Nanofibers as Uniaxially Aligned Arrays* Nano Lett., 2003. 3(8): p. 1167-1171.
28. Yarin, A.L., S. Koombhongse, and D.H. Reneker, *Bending instability in electrospinning of nanofibers*. Journal of Applied Physics, 2001. 89(5): p. 3018-3026.
29. Shin, Y.M., et al., *Experimental characterization of electrospinning: the electrically forced jet and instabilities*. Polymer, 2001. 42(25): p. 9955-9967.
30. Fridrikh, S.V., et al., *Controlling the Fiber Diameter during Electrospinning*. Physical Review Letters, 2003. 90(14): p. 144502.
31. Yarin, A.L., W. Kataphinan, and D.H. Reneker, *Branching in electrospinning of nanofibers*. Journal of Applied Physics, 2005. 98(6): p. 064501.
32. Kessick, R., J. Fenn, and G. Tepper, *The use of AC potentials in electro spraying and electrospinning processes*. Polymer, 2004. 45(9): p. 2981-2984.
33. Taylor, G.I., *Electrically driven jets*. Proceedings of the Royal Society of London. Series A, Mathematical and Physical Sciences 1969. 313: p. 453-475.
34. Taylor, G.I., *Disintegration of water drops in an electrical field*. Proceedings of the Royal Society of London. Series A, Mathematical and Physical Sciences 1964. 258: p. 383.
35. Yarin, A.L., S. Koombhongse, and D.H. Reneker, *Taylor cone and jetting from liquid droplets in electrospinning of nanofibers*. Journal of Applied Physics, 2001. 90(9): p. 4836-4846.
36. Hohman, M.M., M. Shin, and G. Rutledge, *Electrospinning and electrically forced jets. I. Stability theory*. Physics of fluids, 2001. 13: p. 2201-2222.
37. Hohman, M.M., et al., *Electrospinning and electrically forced jets. II. Applications*. Physics of Fluids, 2001. 13: p. 2221-2236.
38. Shin, Y.M., et al., *Electrospinning : A whipping fluid jet generates submicron polymer fibers*. Appl. Phys. Lett., 2001. 78: p. 1149-1151.
39. Dietzel, J.M., et al., *The effect of processing variables on the morphology of electrospun nanofibers and textiles*. Polymers, 2001. 42: p. 261-272.

40. Koombhongse, S. and D.H. Reneker, *Branched and split fiber from electrospinning process*. Book of abstracts, New Frontiers in Fiber Science, Spring meeting, 2001.
41. Shkadov, V.Y. and A.A. Shutov, *Disintegration of charged viscous jet in high electric field*. Fluid Dynamics Research, 2001. 28: p. 23-29.
42. Spivak, A.F., Y.A. Dzenis, and D.H. Reneker, *A model of steady state jet in the electrospinning process*. Mechanics of Research Communications, 2000. 27: p. 37-42.
43. Shenoy, S.L., et al., *Role of chain entanglements on fiber formation during electrospinning of polymer solutions: good solvent, non-specific polymer-polymer interaction limit*. Polymer, 2005. 46(10): p. 3372-3384.
44. Zhong, X., et al., *Structure and process relationship of electrospun bioabsorbable nanofiber membranes*. Polymer, 2002. 43(16): p. 4403-4412.
45. Fong, H., I. Chun, and D.H. Reneker, *Beaded nanofibers formed during electrospinning*. Polymer, 1999. 40(16): p. 4585-4592.
46. Ramakrishna, S., et al., *An Introduction Electrospinning and Nanofibers*. 2005: World Scientific.
47. Zeng, J., et al., *Biodegradable electrospun fibers for drug delivery*. Journal of Controlled Release, 2003. 92(3): p. 227-231.
48. Ladawan Wannatong, A.S.P.S., *Effects of solvents on electrospun polymeric fibers: preliminary study on polystyrene*. Polymer International, 2004. 53(11): p. 1851-1859.
49. Choi, J.S., et al., *Effect of organosoluble salts on the nanofibrous structure of electrospun poly(3-hydroxybutyrate-co-3-hydroxyvalerate)*. International Journal of Biological Macromolecules, 2004. 34(4): p. 249-256.
50. Lee, K.H., et al., *The change of bead morphology formed on electrospun polystyrene fibers*. Polymer, 2003. 44(14): p. 4029-4034.
51. Haiqing Liu, Y.-L.H., *Ultrafine fibrous cellulose membranes from electrospinning of cellulose acetate*. Journal of Polymer Science Part B: Polymer Physics, 2002. 40(18): p. 2119-2129.
52. Mo, X.M., et al., *Electrospun P(LLA-CL) nanofiber: a biomimetic extracellular matrix for smooth muscle cell and endothelial cell proliferation*. Biomaterials, 2004. 25(10): p. 1883-1890.
53. Buchko, C.J., et al., *Processing and microstructural characterization of porous biocompatible protein polymer thin films*. Polymer, 1999. 40(26): p. 7397-7407.
54. Sherman, C.P., *Handbook of Instrumental Techniques for Analytical Chemistry*. Settle, F. eds., 1997. Chap 15.
55. Bekalis, N.M., *Characterisation of polymers: Encyclopedia Reprints*". Wiley-interscience, 1971: p. 125-148.
56. Chalmers, J.M. and N.J. Overall, *Polymer Characterisation* Hunt, B. J. and James, M. I. eds.), 1993: p. Chap 4.
57. Hsu, S.L., *Comprehensive Polymer Science: The synthesis, Characterisation, Reactions and Applications of Polymers*. G. Allen and J. C. Bevington, eds, 1989. 1(chap 20).
58. Raman, C.V. and K.S. Krishnan, *A new type of secondary radiation*. Nature, 1928. 121: p. 501-502.
59. Dresselhaus, M.S., et al., *Raman spectroscopy of carbon nanotubes*. Physics Reports, 2005. 409(2): p. 47-99.
60. Rao, A.M., et al., *Effect of van der Waals Interactions on the Raman Modes in Single Walled Carbon Nanotubes*. Physical Review Letters, 2001. 86(17): p. 3895.
61. Weber, W. and R. Merlin, *Raman Scattering in Materials Science*. Springer, 2000. Berlin.

62. Doorn, S.K., et al., *Raman Spectroscopy and Imaging of Ultralong Carbon Nanotubes*. J. Phys. Chem. B, 2005. 109(9): p. 3751-3758.
63. National Physical Laboratory. *Materials Solutions*, www.materias.npl.co.uk/matsol/thermal.html. [cited.
64. Binnig, G., C.F. Quate, and C. Gerber, *Atomic Force Microscope*. Physical Review Letters, 1986. 56(9): p. 930-933.
65. *Atomic Force Microscopy Overview*. <http://www.nanoscience.com/education/AFM.html>, 2007.
66. Wu, B., A. Heidelberg, and J.J. Boland, *Mechanical properties of ultrahigh-strength gold nanowires*. Nat Mater, 2005. 4(7): p. 525-529.
67. Kooops, H.W.P., A. Kaya, and M. Weber. *Fabrication and characterization of platinum nanocrystalline material grown by electron-beam induced deposition*. 1995: AVS.
68. Heidelberg, A., et al., *A Generalized Description of the Elastic Properties of Nanowires*. Nano Lett., 2006. 6(6): p. 1101-1106.
69. Tucker Iii, C.L. and E. Liang, *Stiffness predictions for unidirectional short-fiber composites: Review and evaluation*. Composites Science and Technology, 1999. 59(5): p. 655-671.
70. Callister, W.D., *Materials Science and Engineering, an Introduction*. 2003, New York: Wiley.
71. J. C. Halpin Affdl, J.L.K., *The Halpin-Tsai equations: A review*. Polymer Engineering & Science, 1976. 16(5): p. 344-352.
72. Cox, H.L., *The Elasticity and Strength of Paper and Other Fibrous Materials*. British Journal of Applied Physics, 1952. 3(MAR): p. 72-79.
73. Kelly, A. and W.R. Tyson, *Tensile Properties of Fibre-Reinforced Metals - Copper/Tungsten and Copper/Molybdenum*. Journal of the Mechanics and Physics of Solids, 1965. 13(6): p. 329-&.
74. Krenchel, H., *Fibre reinforcement*.: 1964, Copenhagen: Akademisk Forlag.
75. O'Regan, M.D.F., Akay, and B. Meenan, *A comparison of Young's modulus predictions in fibre-reinforced-polyamide injection mouldings*. Composites Science and Technology, 1999. 59(3): p. 419-427.
76. Sandler, J., et al., *Carbon-nanofibre-reinforced poly(ether ether ketone) composites*. Composites Part A: Applied Science and Manufacturing, 2002. 33(8): p. 1033-1039.
77. Sandler, J., et al., *Carbon-nanofibre-reinforced poly(ether ether ketone) fibres*. Journal of Materials Science, 2003. 38(10): p. 2135-2141.
78. Sandler, J.K.W., et al., *A comparative study of melt spun polyamide-12 fibres reinforced with carbon nanotubes and nanofibres*. Polymer, 2004. 45(6): p. 2001-2015.
79. Coleman, J.N., et al., *Reinforcement of polymers with carbon nanotubes. The role of an ordered polymer interfacial region. Experiment and modeling*. Polymer, 2006. 47(26): p. 8556-8561.
80. D. Blond, et al., *Enhancement of Modulus, Strength, and Toughness in Poly(methyl methacrylate)-Based Composites by the Incorporation of Poly(methyl methacrylate)-Functionalized Nanotubes*. Advanced Functional Materials, 2006. 16(12): p. 1608-1614.
81. Halpin, J.C. and J.L. Kardos, *The Halpin-Tsai equations: A review*. Polymer Engineering & Science, 1976. 16(5): p. 344-352.
82. Qian, D., et al., *Load transfer and deformation mechanisms in carbon nanotube-polystyrene composites*. Applied Physics Letters, 2000. 76(20): p. 2868-2870.

83. Cadek, M., et al., *Morphological and mechanical properties of carbon-nanotube-reinforced semicrystalline and amorphous polymer composites*. Applied Physics Letters, 2002. 81(27): p. 5123-5125.

Chapter 4: Properties of PMMA Reinforced With Carbon Nanotubes.

4.1 Introduction.

This chapter presents the mechanical properties of composite films fabricated by in situ polymerisation of amorphous poly(methyl methacrylate) (PMMA) in the presence of purified chemical vapour deposition (CVD)-produced –OH functionalised MWNTs to give a PMMA–CNT blend. We also used models to fit the mechanical reinforcement observed in these composites and also to understand the mechanism of the stress transfer between the nanotubes and the polymer.

4.2 Background and Motivation.

Poly (methyl methacrylate)/CNTs composites cannot be achieved by solution processing. This is because carbon nanotubes can not dispersed in a PMMA solutions. As a result, carbon nanotubes aggregate and subsequently sedimentation occurs. In other words the nanotubes-PMMA interaction are too weak to allow a good dispersion and suspension of nanotube in PMMA solutions. This results in a poor stress transfer between both the nanotube and the matrix. As a result, the mechanical reinforcement is highly compromised. For example, the figure below (fig: 4.1) shows PMMA/nanotubes drop-cast films. Samples A was made by solution mixing of commercial PMMA with –OH functionalised MWNTs using ultrasonication. Samples B was made by radical in situ polymerisation with MMA monomers and the very same nanotubes. In both case, the solution composites have the same concentration of PMMA (30g/l) and the same loading level of nanotubes (1 wt % of the PMMA mass). It quite clear that solution processing is highly ineffective.



Figure 4.1: Drop cast films of PMMA/CNTs composites, a) by solution mixing processing b) by in situ polymerisation processing.

However, several methods have been reported to produce amorphous polymer-nanotube composites with good dispersion. For example, Gorga et al used extrusion processing method to achieved PMMA composites with a content of MWNTs up to 10 wt % [1]. Melt processing has also been reported. With this method Haggemueller et al enhanced mechanical and electrical properties of PMMA/SWNTs films [2]. Films were made by first by solution mixing and drop casting method. Then the films were broken into pieces and stacked between two polished metal plates. The stack was then hot pressed at 180°C for 3 minutes. The resulting product was broken, stacked and hot pressed again. This produce was repeated as many as 25 times to ensure a homogenous dispersion. Many authors have also reported the use of functionalised CNTs to improve the mechanical properties in polymer-CNT composites [3-5]. Using this method Hwang et al grafted MWNTs to PMMA via an emulsion reaction. The PMMA-grafted MWNTs significantly improved connection between the MWNTs and the PMMA matrix resulting in a uniform dispersion of the MWNTs in the matrix[6].

Another method involves in situ polymerisation in the presence of pristine nanotubes which can result in covalent attachment of nanotubes to the polymer. Consequently, better dispersion and stronger interface between the nanotubes and the polymer matrix is achieved [7-12]. Using this process with pristine carbon nanotubes, Jia et al. [13] have suggested that during the polymerisation, the initiator could open the π bonds of the CNTs and therefore lead to a strong interaction between the nanotubes and the polymer. However, in situ polymerisation in the presence of functionalised nanotubes is even more promising owing to the superior dispersion of functionalised nanotubes in solvents and potential for chemical reactions between the initiator and the functional group. This results in more complete polymerisation and more effective crosslinking of the polymer with the nanotubes and so increases the mechanical properties.

4.3 Films Preparation.

PMMA–CNT composites were synthesised using an in situ radical polymerisation method. In a typical procedure, MMA monomer (99 %,Aldrich) was distilled twice to remove any impurities. The free-radical initiator azobisisobutyronitrile 2,2 (AIBN, Aldrich) was mixed with 1 g of purified MMA and -OH functionalized thin MWNTs (www.nanocyl.be). The solution was sonicated for 5 min in a sonic bath to remove any trapped air. The quantities of CNTs and AIBN relative to MMA were 1 wt% and 0.25 wt %, respectively. The solution was then stirred and heated to 90 °C for 2 h [13]. Consequently, a homogenous solid PMMA/CNT composite was formed (fig: 4.2), which was subsequently cured for 12 h at 90 °C.

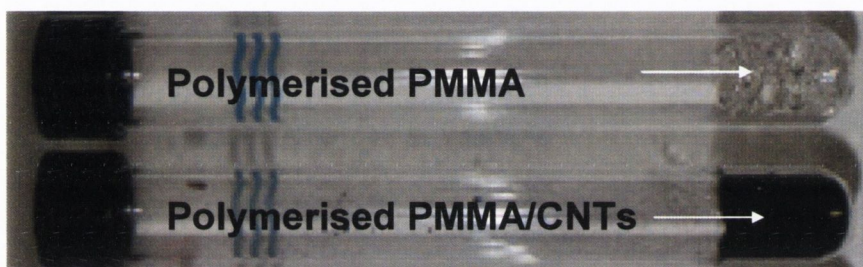


Figure 4.2: Homogenous solid of polymerised PMMA and PMMA/CNTs.

To prepare a range of composite mass fractions, the polymerised sample was dissolved in toluene at a concentration of 30 g/l. To achieve a good dispersion, the solution was sonicated for 5 min using a high-power sonic tip (120 W, 60 kHz) followed by a mild sonication for 3 h in a sonic bath, followed by further high-power sonication for an additional 5 min. Afterwards, the primary solution was blended with pure PMMA solution polymerised under the same conditions to produce a range of various mass fractions of up to 1wt %. Another batch was also produce by blending the primary solution with commercial PMMA from Aldrich. After blending, an extra sonication process was carried out on each sample by using the high-power sonic tip and sonic bath for the same time periods as before. Freestanding films were fabricated by dropping 1 mL of each solution onto a polished Teflon square that was then placed in an oven at 60 °C to allow the evaporation of the solvent. This procedure was repeated four times in order to obtain an average film thickness of 75 ± 5 μm (fig: 4.3) containing a homogenous dispersion of carbon nanotubes. It should be pointed out

that this technique does not allow a total evaporation of the solvent within the films. About 10wt% of solvent was still trapped in the composites.

For each sample, nanotube mass fractions were converted into volume fraction using the following equation 4.1:

$$V_f = \left[1 + \left(\frac{\rho_{NT}}{\rho_{Pol}} \right) \times \left(\frac{1 - m_f}{m_f} \right) \right]^{-1} \quad \text{Equation: 4.1}$$

Where V_f stands for the volume fraction ($V_f = V_{NT} / (V_{NT} + V_{Pol})$) and m_f for the mass fraction ($m_f = m_{NT} / (m_{NT} + m_{Pol})$) of CNTs present in the polymer. ρ_{NT} and ρ_{Pol} are respectively the densities of the CNTs and the polymer matrix. Densities of 2150 kgm^{-3} and 1300 kgm^{-3} were used for nanotubes and polymer respectively [14]

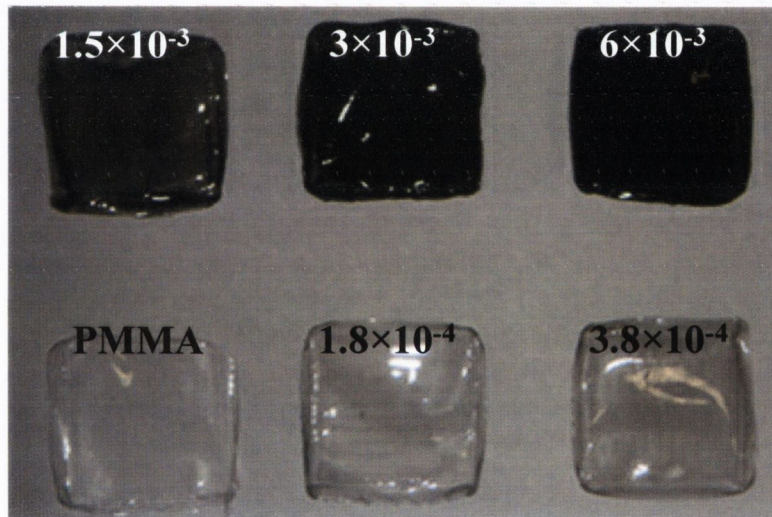


Figure 4.3: Drop-cast PMMA composite films with range of volume fraction of nanotubes from 1.8×10^{-4} to 6×10^{-3} .

4.4 FTIR Characterisations.

It is important to determine whether or not functional groups have been covalently attached to the nanotubes. Infrared spectrometry was carried out in the mid-infrared ($4000\text{-}5000\text{cm}^{-1}$) region using a Nicolet FTIR spectrometer. Spectra were taken for polymerised PMMA and compared with commercial PMMA spectra in order to confirm the integrity of the polymerisation reaction. Figure 4.4 represents the infrared spectrum of CNTs that have reacted

with the PMMA during the polymerisation (reacted CNTs) compared to unreacted, pristine CNTs.

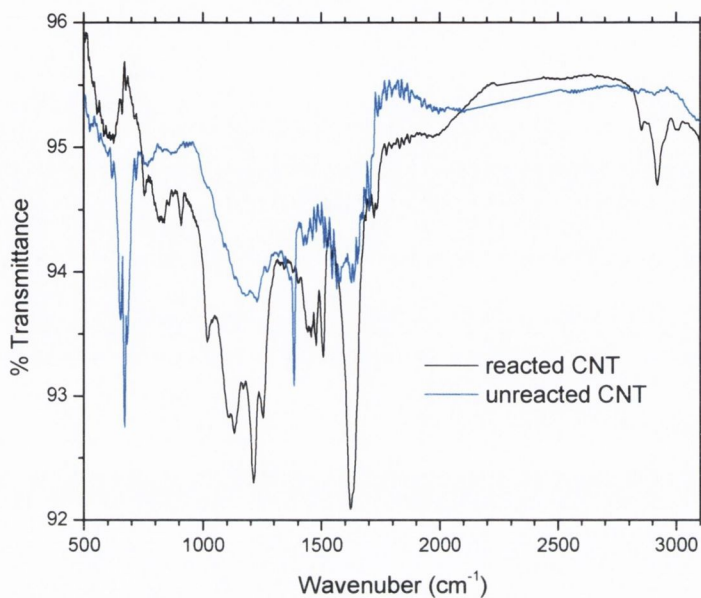


Figure 4.4: FTIR spectra of reacted and unreacted carbon nanotubes.

Samples were prepared first by dissolving polymerized PMMA/CNTs in toluene. Then, the solution was washed five times through a filter paper (pore size 0.22 μm) to remove PMMA chains that had not reacted with CNTs. The residue was then scraped from the filter paper, dried, and mixed with potassium bromide to obtain thin semitransparent films. Raw CNTs were also mixed with KBr for comparative analysis. In addition, infrared spectroscopy was performed on both pure toluene and each filtrate. While initial filtrates showed evidence of PMMA, the spectra for the final filtrate and toluene were identical, showing that all excess unbounded PMMA had been washed from the nanotubes after five washes. This strongly suggests that any species appearing in the reacted spectra are covalently attached to the nanotubes.

The first three peaks in the reacted spectrum at 3010, 2921 and 2853 cm^{-1} are characteristic of PMMA, and they are not present on the unreacted spectrum. Also the peak at 1721 cm^{-1} could represent an esteric group which is present in the PMMA structure. The peak at 1622 cm^{-1} is present only in the reacted spectrum. It corresponds to the C=O vibration of the side chain of PMMA. Moreover the intense peak in the unreacted spectrum at 1383 cm^{-1} represents the vibration of an alcohol groups (-OH) associated with the original functionality. After the polymerisation reaction, this peak was absent from the reacted spectrum suggesting that bonding occurs between functionalised groups and PMMA. The nature of the peak at 681

cm^{-1} is unclear at present time; however this peak had completely disappeared in the reacted spectra. As a whole this FTIR data strongly suggest that at least some of the PMMA chains are covalently attached to the nanotubes. The main peaks observed are summarised in the Table 4.1.

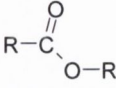
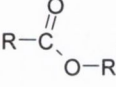
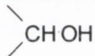
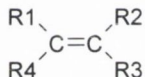
Fragment of reacted CNT	Wavenumber (cm^{-1})
$-\text{CH}_2-$ (acyclic)	2921.19
$-\text{O}-\text{CH}_3$, $-\text{CH}_2-$ (acyclic)	2853.25
	1721.84
$\text{C}=\text{C}, \text{C}=\text{O}$	1622.73
 , $-\text{O}-$	1131.7, 1104.93
$-\text{O}-$	1018.42, 910.33, 838.21
Fragment of unreacted CNT	Wavenumber (cm^{-1})
	1383.95
	681.19, 671.16

Table 4.1: IR frequencies of the different compounds of the reacted and unreacted carbon nanotubes.

4.5 Mechanical Characterisations.

Tensile measurements were carried out using a Zwick tensile tester with a 100N load cell and a cross head speed of $0.5 \text{ mm}\cdot\text{min}^{-1}$. To determine the mechanical properties of the PMMA composite films, five measurements on five different strips were performed on each sample for statistical accuracy. The dimensions of the strips were $10 \text{ mm} \times 2.5 \text{ mm} \times 75 \mu\text{m}$. Shown in Figure 4.5 and 4.6 are representative stress–strain curves for some of the composites studied in this work. The first stress-strain curve represents the composites film blended with polymerised PMMA (Composites *A*). The second curve represents the composites film blended with commercial PMMA (Composites *B*). The strain, ϵ , represents the fractional elongation while the stress, σ , is the force divided by the cross-sectional area of the unloaded sample.

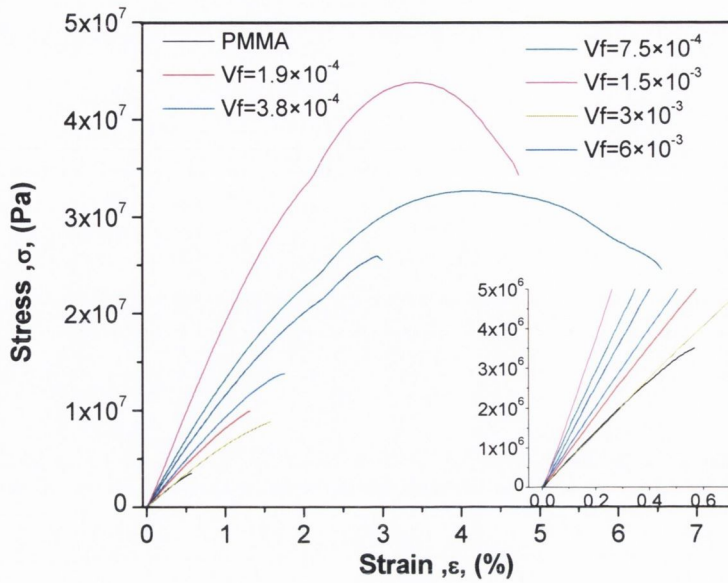


Figure 4.5: Representative Stress-Strain curves for Composites *A* for a range of volume of nanotubes. The inset is a magnification at low strain.

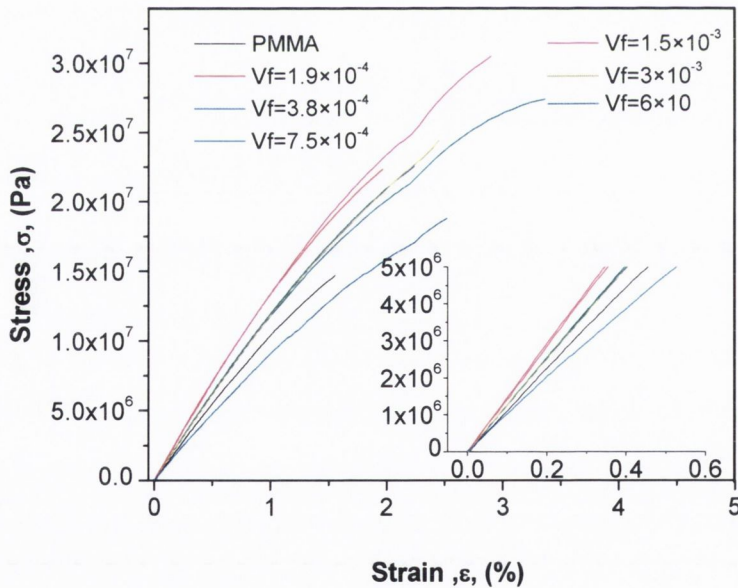


Figure 4.6: Representative stress-strain curves for Composites *B* for a range of volume fractions of nanotubes. The inset is a magnification at low strain.

In the case of the composites blended with polymerised PMMA, the pristine polymer displays elastic behaviour up to a yield point of $\varepsilon = 0.2\%$, followed by a small deformation before fracture occurs at a strain-to-break of $\varepsilon_B = 0.57\%$. This low value of strain-to-break is typical for low-molecular-weight polymers such as this material [15]. Dramatic changes in the

stress–strain curves can be observed on the addition of CNTs. As the nanotube content is increased, the yield point increases to approximately $\varepsilon = 0.66\%$ for the sample with a volume fraction (V_f) of 7.5×10^{-4} . In addition, significant plastic deformation is observed for mid-range nanotube-loading levels. The strain-to-break increases steadily with nanotube volume fraction reaching $\varepsilon_B = 6.53\%$ for the $V_f = 7.5 \times 10^{-4}$ sample. This is unusual, as most polymer–nanotube composites become brittle on the addition of even small amounts of nanotubes. However, above this volume fraction the strain-to-break does indeed fall off and the material becomes more brittle as more nanotubes are added. This trend is shown in Figure 4.7.

For composites blended with commercial PMMA, the pristine polymer also display an elastic behaviour up to a yield point of $\varepsilon = 0.37\%$ which is followed by a small deformation before fracture occurs at a strain-to-break of $\varepsilon_B = 1.57\%$. However, by adding small content of carbon, changes in the stress strain curves are less significant compare to composite *A*. Linear increase in ε_B is observed only up to 2.24% for a nanotubes volume fraction of 7.5×10^{-4} . At higher content of nanotubes ε_B also fall off (fig: 4.7). Moreover, for the highest ε_B , the plastic deformation is less impressive compare to composite *A* at the same volume fraction.

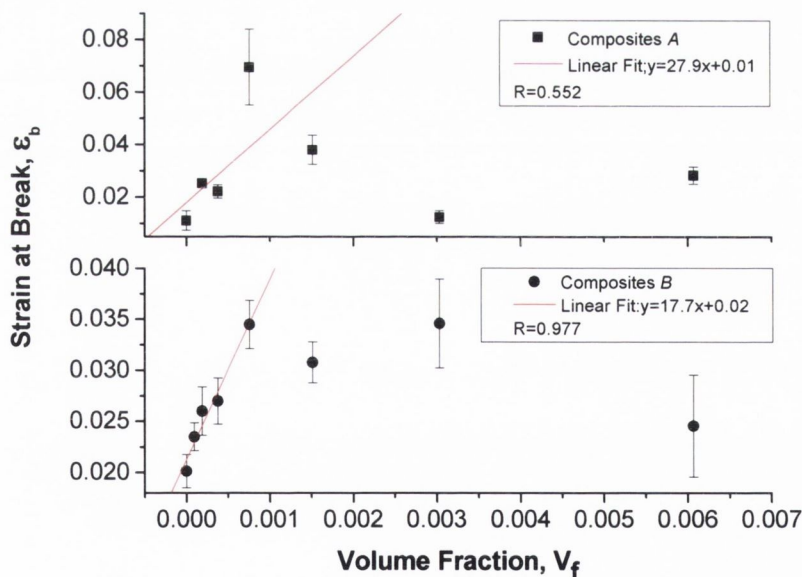


Figure 4.7: Strain at break of Composites *A* and *B* as a function of volume fraction of carbon nanotubes with the corresponding standard error.

More importantly, for low CNT contents, a remarkable increase in stiffness, strength, and toughness is clearly visible for both composites *A* and *B*. Figure 4.8 shows the Young’s

moduli as a function of the volume fraction of CNTs for all composites studies. The Young's modulus was calculated from the linear elastic deformation from each stress-strain curve of all the composites studied. In the case of composites *A*, it can be clearly seen that the Young's modulus increases linearly with volume fraction before falling off at higher volume fractions. This linear increase occurs up to an optimum loading level of $V_f = 1.5 \times 10^{-3}$. This represents an increase of $\times 1.9$, from 0.71 GPa to 1.38 GPa. The enhancement of the Young's modulus, dY/dV_f , which is the fit of the linear increase of the Young's modulus was found to be 586 ± 89 GPa in this case. For composites *B*, increase of the Young's modulus was also observed. However, this increase was not as linear as for composites *A*. Nevertheless, optimum loading level occurs at volume fraction of $V_f = 1.5 \times 10^{-3}$ which represents an increase of $\times 1.23$ from 1.04 GPa to 1.28 GPa. Despite an approximate fitting, dY/dV_f was calculated to be 80 ± 1.8 GPa for low volume fractions of nanotubes. It should be pointed out that at a loading level of 6×10^{-3} V_f of CNTs the Young's modulus of this composite is about 0.88 GPa. This represents a lower value than the pristine PMMA (1.04 GPa). This clearly shows that above a certain loading level, carbon nanotubes aggregation occurs and as a consequence it compromises the reinforcement. It is also interesting to notice the difference in value between the pristine PMMA from composite *A* and *B* (0.71 and 1.04 GPa). This can be attributed to the difference in the molecular weight between *A* and *B* which are respectively 3500 gmol^{-1} and 50000 gmol^{-1} .

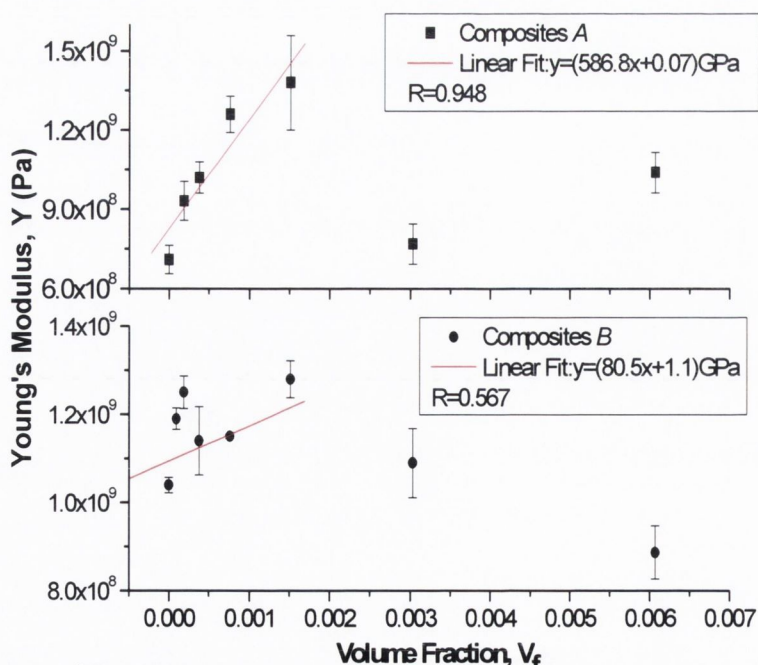


Figure 4.8: Young's Modulus for composites *A* and *B* as a function of volume fraction of carbon nanotubes with the corresponding standard error.

Previous work [12] preparing PMMA–functionalised-CNT composites by in situ polymerisation has shown an increase in the storage modulus of 81% by adding 0.009 volume fraction of CNTs by thermal mechanical analysis at 40 °C. In this case dY/dV_f was equal to ~ 146 GPa. A dramatic increase in the storage modulus at 20 °C from 2.5 GPa for pure PMMA to 31 GPa for a composite containing $V_f = 0.13$ PMMA-grafted MWNTs made by emulsion polymerisation was also reported [6] By this method, dY/dV_f was equal to ~ 203 GPa. In both cases, these results were obtained using dynamic mechanical analysis (DMA). It should be pointed out that the dY/dV_f values presented here are significantly higher than those appearing in the literature for comparable composites. However, due to saturation at relatively low V_f we have not achieved moduli comparable to those discussed by Hwang et al [6].

Young's modulus data can be analysed using the models described in the previous chapter. These are namely the Krenchel's rule of mixtures for short fibres composites [16] and the Halpin-Tsai equations [17]. The Krenchel's rule of mixtures is given by:

$$Y_c = (\eta_0 \eta_1 Y_{NT} - Y_p) V_f + Y_p \quad \text{Equation: 4.2}$$

Where Y_c , Y_{NT} , and Y_p are the composite, nanotube, and polymer moduli, V_f is the nanotube volume fraction, and η_0 and η_1 are efficiency factors related to fiber orientation [16] and length [18] We assume a preferential orientation of the nanotubes in the plane of the film, in analogy with the situation for PVA–nanotube films also made by drop casting processing on similar conditions [19]. In this case, η_0 can be chosen to be equal to 3/8 [16, 19, 20]. Previous work based on PVA composites has shown that it is very difficult to separate the contributions of η_1 and Y_{NT} when using small data sets [20]. Therefore, an effective nanotube modulus can be defined by :

$$Y_{Eff} = \eta_1 Y_{NT} \quad \text{Equation 4.3}$$

The modulus values for catalytic nanotubes, lie in the region of 10 to 500 GPa [21]. Combining equations 4.2 and 4.3 and taking Y_{Eff} equal to 10 and 500 GPa we found a average value for dY_c/dV_f and its standard error to be equal respectively to 94.91 ± 92.15 GPa and 94.6 ± 92.15 GPa using the pristine PMMA from composites *A* and *B*. This model clearly does

not fit the dY_c/dV_f observed in the linear increase in composites *A* (586 ± 89 GPa). The model fit the enhancement Young's modulus obtained for composites *B* (80 ± 1.8 GPa). However, this fit agrees with experimental data because of the fit linear we choose for to measure the reinforcement. If we would have chosen the best linear fit, the experimental dY_c/dV_f would have been about 1.23 ± 0.2 TPa. This suggest that Krenchel's rule does not always apply well to nanotubes-based composites [22, 23].

Using the alternative Halpin-Tsai model for random orientation fillers given by:

$$Y_c = Y_p \left[\frac{3}{8} \left(\frac{1 + \zeta \eta_L V_f}{1 - \zeta \eta_L V_f} \right) + \frac{5}{8} \left(\frac{1 + 2\eta_T V_f}{1 - \eta_T V_f} \right) \right] \quad \text{Equation 4.4}$$

The enhancement Young's modulus can be then be expressed as:

$$\frac{dY_c}{dV_f} \approx \frac{3}{8} Y_p \eta_L (\zeta + 1) + \frac{15}{8} Y_p \quad \text{Equation 4.5}$$

Where η_L and η_T have been defined in the pervious chapter and $\zeta = 2l/D$ with l and D the length and the diameter of the fibre respectively. This approximation is valid as $V_f \rightarrow 0$ and for stiff fibres where $Y_f \gg Y_p$ [24].

We carried out Transmission Electro Microscopy (TEM) in order to measure the length and the diameter of the nanotubes used in this study (Fig 4.9). After carefully measuring over 100 nanotubes average value for the length and the diameters were respectively 1225 ± 592 nm and 16.65 ± 3.97 nm. Therefore we estimated a value for ζ to be equal to 147 ± 105 .

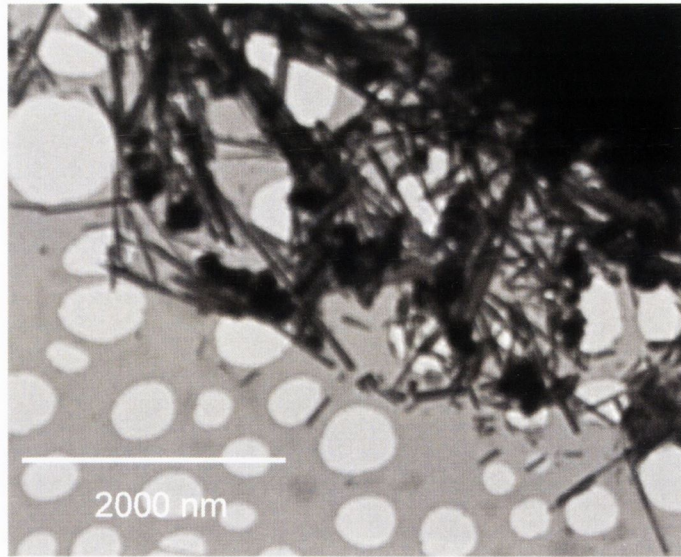


Figure 4.9: TEM picture of OH functionalized MWNTs.

Taking Y_f equal to 10GPa and 500GPa, the calculated dY_c/dV_f is then found to be 19.2 ± 14.7 GPa and 25.7 ± 20.6 GPa using pristine PMMA of composites *A* and *B*, respectively. In both case, the Halpin-Tsai model does not fit the enhancement Young's modulus estimated from the experimental data.

Therefore both models cannot be applied to fit the reinforcement observed for low loading level of nanotubes for PMMA composites blended with polymerised PMMA and commercial PMMA. This suggest than another model is required to express the stress transfer which occur between the nanotubes and the polymer.

The breaking strength, σ_B , and ultimate tensile strength, σ_C , are represented in Figure 4.10 for composites *A* and *B*. σ_B corresponds to the stress at which fracture occurs. σ_C represents the maximum stress value applied to the material. In general, for viscoelastic materials there is a clear difference between σ_C and σ_B , with $\sigma_C \geq \sigma_B$.

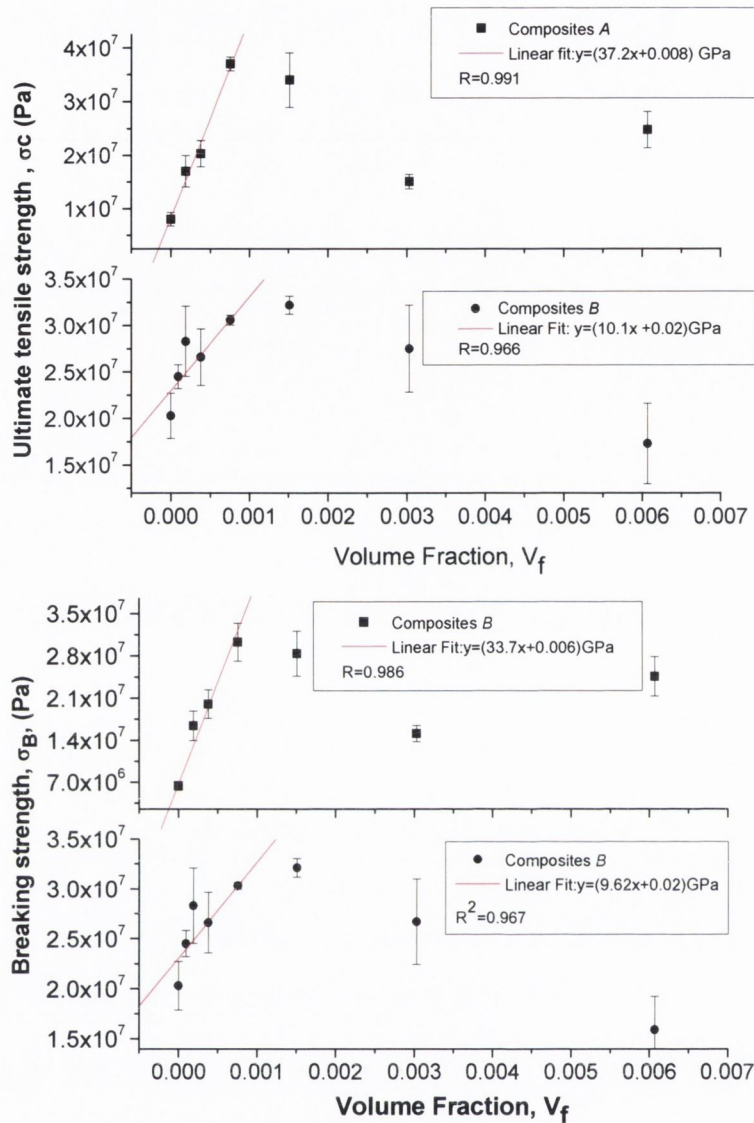


Figure 4.10: Ultimate tensile strength and breaking strength for PMMA composites blended with polymerised PMMA and commercial PMMA as a function of volume fraction of carbon nanotubes with the corresponding standard error.

However, when the material has a very small plastic deformation, the two parameters can be very similar, or in some cases identical. This is the case for our low-volume-fraction composites, resulting in similar trends for the two parameters. In both cases a linear increase in strength was observed followed by a fall off. For the composites blended with polymerised PMMA, a dramatic increase in σ_C from 8.03 MPa to 37 MPa was observed by adding less than $7.5 \times 10^{-4} V_f$ of nanotubes. Similarly, an increase in σ_B from 6.4 MPa for the polymer to 30.3 MPa for the $7.5 \times 10^{-4} V_f$ sample was recorded. The slopes for these linear increases were calculated to be $d\sigma_C/dV_f=38 \pm 2.4$ GPa and $d\sigma_B/dV_f=33.7 \pm 3.6$ GPa. It should be pointed out

that the low strength of the pure polymer is due to its relatively low molecular weight of 3500 g mol⁻¹, which corresponds to approximately 67 repeat units. Similarly, the composites blended with commercial PMMA show increase in σ_C from 20.3 MPa to 30.6 MPa was observed by adding less than $7.5 \times 10^{-4} V_f$ of nanotube. Breaking strength also increase from 20.3 GPa up to 30.3 GPa for a loading level of nanotubes of $7.5 \times 10^{-4} V_f$. These linear increases gives values of 10.1 ± 1.78 GPa and 9.62 ± 1.66 GPa for $d\sigma_C/dV_f$ and $d\sigma_B/dV_f$ respectively.

Jia et al [13] also noticed strength enhancement when using unfunctionalised MWNTs in PMMA composites fabricated by in situ polymerisation. Reinforcement of up to 30% in σ_B was achieved by adding 0.03 volume fraction of CNTs. Velasco- Santos et al. [12] have reported an increase of 75% in σ_B by using functionalised MWNTs with a volume fraction of $V_f = 0.009$ and a 41% increase by adding $V_f = 0.006$ unfunctionalised MWNTs.

The strength of fiber-reinforced composites can be described by the rule of mixtures. In the framework of this model, if the fibres are longer than the so-called critical length, the rule of mixtures can be expressed by [15]

$$\sigma_B = \left[\left(1 - \frac{lc}{2l} \right) \sigma_{NT} - \sigma_P \right] V_f + \sigma_P \quad \text{Equation 4.6}$$

where σ_B , σ_{NT} , and σ_P are the composite, the nanotube, and the polymer strengths, respectively (σ_P is measured from the breaking strength of the polymer, referred to earlier as σ_B). The nanotube length is described by l while lc represents the critical length. This is the nanotube length below which the polymer can no longer transfer enough stress to break the nanotube. The expression of lc given in the previous chapter can approximated as follows

$$lc = \frac{\sigma_{NT} D}{2\tau} \left[1 - \frac{d^2}{D^2} \right] \approx \frac{\sigma_{NT} D}{2\tau} \quad \text{Equation 4.7}$$

where D is the nanotube outer diameter, d is the diameter of the inner channel, and τ is the interfacial shear strength (IFSS). The approximation is valid for large-diameter nanotubes with narrow inner channels, as we have here. Combining Equations 4.6 and 4.7 (neglecting σ_P ,

which is relatively small), differentiating with respect to V_f , and re-arranging gives a quadratic equation for the nanotube strength. The solution to this equation is:

$$\sigma_{NT} = \tau \frac{2l}{D} \left[1 \pm \sqrt{1 - \frac{D}{l} \frac{d\sigma_B}{dV_f}} \right] \quad \text{Equation 4.8}$$

The validity of this expression can easily be checked by showing that in the limit where the nanotube length approaches infinity, $\sigma_{NT} \rightarrow d\sigma_B/dV_f$, as expected from Equation 4.6 (taking the minus sign). For σ_{NT} to be real, the following condition must be imposed

$$\tau \geq \frac{D}{l} \frac{d\sigma_B}{dV_f} \quad \text{Equation 4.9}$$

Taking $d\sigma_B/dV_f$ equal to 33.7 ± 3.6 GPa and 9.6 ± 1.6 GPa for composites *A* and *B* and applying Equation 4.9, τ was calculated to be $\geq 470 \pm 400$ MPa for composites *A* and $\geq 133 \pm 121$ MPa for composites *B*. The highest values ever suggested to our knowledge is $\tau = 500$ MPa [25]. However, it is unlikely that this figure is realistic. Literature values quote that τ should be in the range of 50-100 MPa [25-29]. However, it is more likely that τ is close to the value for the polymer shear strength, which is in turn probably close to the polymer tensile strength (pristine *A*=6.4 MPa and pristine *B*=20.3 MPa). Thus if this model may apply for composites blended with commercial PMMA, it also suggest than Equation 4.9 is not valid to fit experimental data from composites blended with polymerised PMMA. In this case, the average nanotube length is actually less than the critical length in our samples, which means that Equation 4.6 actually cannot be used here.

The fact that Equation 4.6 does not apply can be further emphasised by calculating the nanotube strength implied by Equation 4.8. If we assume Equations 4.8 and 4.9 apply in this case then the minimum possible value for the nanotube strength can be found to be $\sigma_{NT} \geq 2d\sigma_B/dV_f$, that is $\sigma_{NT} \geq 67.4 \pm 7.2$ GPa. Given that the highest strength ever recorded for perfectly graphitised nanotubes was $\sigma_{NT} = 63$ GPa [30], this is unlikely. In fact, owing to their high defect content, catalytic MWNTs such as those used in this work tend to have strengths of the order of a few gigapascals [31] Thus, it is extremely unlikely that the model described by Equation 4.6 is appropriate in this case of composites blended with polymerised PMMA.

An alternative model describes the situation when the nanotube length is less than the critical length. In this case, the nanotubes do not break when a stress is applied to the material. In fact, failure occurs at the polymer/nanotube interface, generally by debonding of the polymer from the nanotube. The following equation represents a tensile-strength model for short-fiber composites under these circumstances[15]:

$$\sigma_c = \left(\frac{l_{NT}}{2R} \tau - \sigma_p \right) V_f + \sigma_p \quad \text{Equation 4.10}$$

where σ_p is the polymer breaking strength, and R the radius of the nanotubes. By fitting this equation with the data from Figure 4.10 we obtained a value for the interfacial stress transfer of 456 ± 378 MPa. This means that the shear strength lies in the range of $78 \leq \tau \leq 834$ MPa. As discussed previously, the interfacial shear strength is expected to lie in the 50–100 MPa range. Thus, while our calculated τ is within the possible range, it is unlikely that the IFSS is so high, even for covalently functionalized nanotubes. To unambiguously test the applicability of this model, it is necessary to confirm that debonding actually occurs at the polymer/nanotube interface.

In order to test this, scanning electron microscopy (SEM) studies have been carried out on the composites used for mechanical testing. Shown in Figure 4.11 is an SEM image of a crack in the composite film blended with polymerised PMMA.

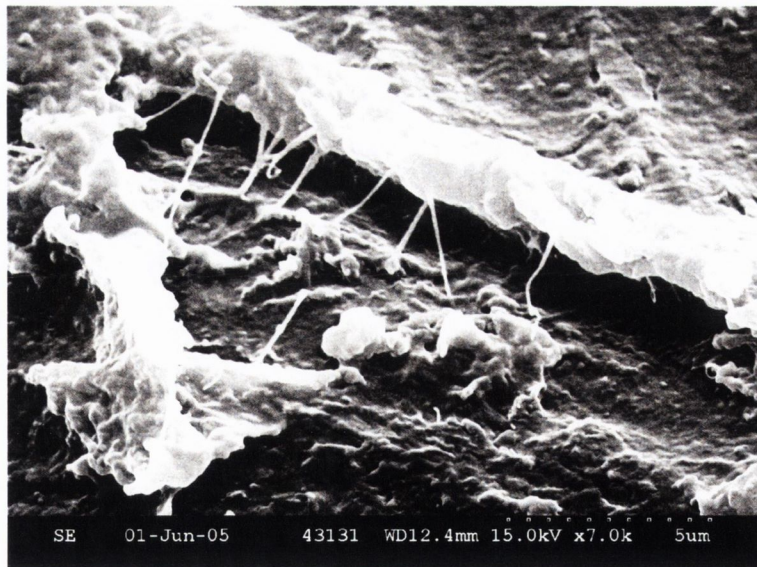


Figure 4.11: SEM picture of Polymer-covered nanotubes bridging a crack in a composite blended with polymerised PMMA.

A number of 1D objects are observed bridging the crack. While these objects are clearly nanotubes, detailed measurements of their average diameter show it to be much larger than that measured for pristine nanotubes by TEM. The measured average diameter of the objects observed by SEM was 111 nm, which can be compared with the average pristine nanotube diameter of 16 nm. Assuming a thickness for the gold coating of 15 nm, this means the nanotubes are covered with some sort of coating of thickness of 33 nm. We suggest that this coating is a very well adhered polymer layer. This layer probably consists of polymer strands that have entangled with the covalently attached functional groups to form a mechanically strong interfacial region. This means that the fracture is unlikely to occur at the polymer/nanotube interface but must occur at the edge of the interfacial region. Therefore, another model is needed. Such a model would take into consideration that the break occurs at a polymer/polymer interface displaced from the polymer/nanotube interface. It can be described by the following equation [20]:

$$\sigma_C = \left(1 + \frac{b}{R}\right) \left[\frac{l_{NT}}{2R} \sigma_{shear} - \left(1 + \frac{b}{R}\right) \sigma_p \right] V_f + \sigma_p \quad \text{Equation 4.11}$$

where b is the thickness of the polymer coating around the nanotubes and σ_p the breaking strength of the bulk polymer.[9] Here, σ_{shear} is the shear strength of the polymer/polymer interface at the edge of the interfacial region. Applying this model σ_{shear} was found to be 88 ± 115 MPa, meaning the shear strength is within a range of $0 < \sigma_{shear} \leq 203$ MPa. While the error is very large, the region of uncertainty does in fact encompass the polymer breaking strength, $\sigma_p = 6.4$ MPa. This confirms that this model may, in fact, be the correct one to fit data from composites blended with polymerised PMMA. This means that the covalently attached polymer strands play a dual reinforcement role. They act to increase the polymer/nanotube IFSS as originally expected. However, in addition, they increase the composite strength by entangling with the matrix polymer to create a high-strength interfacial region. This behavior has been observed before for chlorinated polypropylene-functionalized- nanotube composites [20]. In addition, Barber et al. have observed polymer interfacial regions with anomalously high shear strength in pullout measurements [27]. This may explain the high value of σ_{shear} calculated using Equation 4.9. One might even speculate that this interfacial region is stiffer than the bulk amorphous polymer. It could then act as an extra component of reinforcement,

analogous to the role played by crystalline coatings in Poly(vinyl alcohol)-based composites [20], resulting in higher than expected dY/dV_f values.

The toughness, as shown in Figure 4.12, is the energy needed to break the composite, and can be calculated from the area under the stress–strain curve. It shows a dramatic linear increase of 1282% from 0.069 MJm^{-3} to 0.95 MJm^{-3} by adding $1.5 \times 10^{-3} V_f$ of CNTs for composites *A*. The slope, dT/dV_f , of this linear increase was calculated to be $6.1 \pm 1.38 \times 10^8 \text{ Jm}^{-3}$. It should be pointed out that the linear fit did not take in account the data for $V_f=7.5 \times 10^{-4}$ because of its very high value. Similarly, composites *B* show a linear increase of 200% from 0.26 MJ/m^{-3} up to 0.79 MJ/m^{-3} by adding $1.5 \times 10^{-3} V_f$ of nanotubes. The calculated dT/dV_f is then equal to $6.74 \pm 1.55 \times 10^8 \text{ Jm}^{-3}$. In comparison, Jia et al. [13] obtained an increase of 2.7% by adding 0.03 V_f of treated CNTs and a dT/dV_f value equal to 1281 Jm^{-3} . Similarly, an increase of 74.6% was observed by adding $V_f = 0.009$ of functionalised CNTs [12].

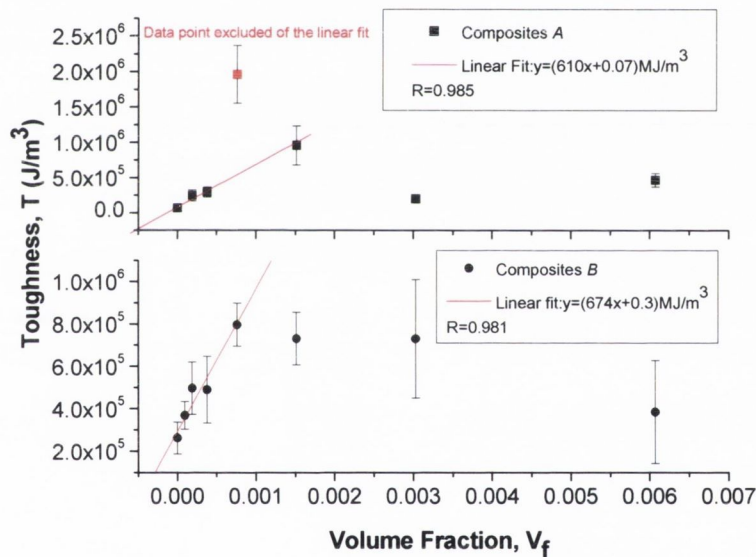


Figure 4.12: Toughness for PMMA composites blended with polymerised PMMA and commercial PMMA as a function of volume fraction of carbon nanotubes with the corresponding standard error.

All mechanical parameters, modulus, strength, and toughness display an approximately linear increase with volume fraction followed by saturation. This results in an optimal nanotube volume fraction for mechanical reinforcement that is extremely low compared to previous measurements. The decrease in mechanical parameters at higher volume fraction can be explained by nanotube aggregation at higher loading levels, resulting in the formation of

stress-concentration centers. This clearly illustrates the importance of good nanotube dispersion at low volume fractions. However, it also shows that the maximum reinforcement is limited by the maximum achievable volume fraction where good dispersion can be maintained. In the future it will be important to try to increase this maximum volume fraction, possibly through careful chemical engineering of the functionalities. Also, the preparation of drop cast film involves a reasonable amount of residual solvent trapped in the films (~10wt%). Therefore, the solvent may act as a plasticizer which may lead to a decrease of the Young's modulus and the strength. Future work needs to be addressed to minimize the present of residual solvent .All the mechanical results are summarised in Table 4.2.

Composite A	Value	Increase	Saturated point, V_f
$dY/dV_f, (\text{Pa})$	$(5.8 \pm 0.9) \times 10^{11}$	94% 0.71GPa→1.38GPa	1.5×10^{-3} vol%
$d\sigma_c/dV_f, (\text{Pa})$	$(3.8 \pm 0.2) \times 10^{10}$	360% 8.03MPa→37MPa	7.5×10^{-4} vol%
$d\sigma_B/dV_f, (\text{Pa})$	$(3.3 \pm 0.3) \times 10^{10}$	373% 6.4MPa→30.3MPa	7.5×10^{-4} vol%
$dT/dV_f, \text{J/m}^3$	$(6.1 \pm 1.3) \times 10^8$	1282% 0.069 MJ/m ³ → 0.95 MJ/m ³	1.5×10^{-3} vol%
$d\epsilon_p/dV_f$	27.9 ± 10.4	526% 0.011 → 0.0695	7.5×10^{-4} vol%
Composite B	Value	Increase	Saturated point, V_f
$dY/dV_f, (\text{Pa})$	$(8 \pm 0.2) \times 10^{10}$	23% 1.04GPa → 1.28 GPa	1.5×10^{-3} vol%
$d\sigma_c/dV_f, (\text{Pa})$	$(1 \pm 0.1) \times 10^{10}$	50% 20.3 MPa→30.6 MPa	7.5×10^{-4} vol%
$d\sigma_B/dV_f, (\text{Pa})$	$(9.6 \pm 1.6) \times 10^9$	49.6% 20.3 GPa→30.3 GPa	7.5×10^{-4} vol%
$dT/dV_f, \text{J/m}^3$	$(6.7 \pm 1.5) \times 10^8$	200% 0.26MJ/m ³ → 0.79MJ/m ³	7.5×10^{-4} vol%
$d\epsilon_p/dV_f$	17.7 ± 3.5	70% 0.02→0.034	7.5×10^{-4} vol%

Table 4.2: Summarisation of the main mechanical results.

4.5 Conclusion.

Polymer composites have been fabricated using PMMA and OH-functionalized MWNTs by in situ polymerization. FTIR studies suggested that bonding between carbon nanotubes and PMMA may occur at the –OH functionality, and also at the outer layer of the CNTs. More analysis needs to be done to confirm these results. Mechanical properties have shown an increase in all the parameters investigated for a low content of carbon nanotubes in both systems i.e. PMMA composites blended with commercial PMMA and polymerised PMMA. Using Krenchel's rule of mixtures and Halpin-Tsai to calculate the theoretical enhancement Young's modulus failed to fit the experimental dY/dV_f for the composite blended with polymerised PMMA. Shear stress, τ , was calculated with two different models. The first model gave an unreasonably high value of 470 ± 400 MPa for composite *A* compared to the expected value 50–100 MPa. However this model gave a more acceptable value of 133 ± 121 MPa for composites *B*. Therefore the second model, which takes into account the microscopy studies, was used to fit the experimental data of composites *A*. In this case the calculated polymer shear strength was found to be 88 ± 115 MPa. While this is much higher than the expected value of approximately 6.4 MPa it is an acceptable value within the error. Also, the range of the error can be explained by the large variations of length of the nanotubes in the TEM studies. Finally, at higher mass fractions, the mechanical properties tend to fall off. This is probably due to aggregation effects at high concentration.

4.6 References.

1. Gorga, R.E. and R.E. Cohen, *Toughness enhancements in poly(methyl methacrylate) by addition of oriented multiwall carbon nanotubes*. Journal of Polymer Science Part B: Polymer Physics, 2004. **42**(14): p. 2690-2702.
2. Haggenueller, R., et al., *Aligned single-wall carbon nanotubes in composites by melt processing methods*. Chemical Physics Letters, 2000. **330**(3-4): p. 219-225.
3. Blake, R., et al., *A Generic Organometallic Approach toward Ultra-Strong Carbon Nanotube Polymer Composites*. J. Am. Chem. Soc., 2004. **126**(33): p. 10226-10227.

4. Hsiao, C.C., et al., *The Nanomechanical Properties of Polystyrene Thin Films Embedded with Surface-grafted Multiwalled Carbon Nanotubes*. *Macromolecules*, 2005. **38**(11): p. 4811-4818.
5. Liu, L., et al., *Mechanical Properties of Functionalized Single-Walled Carbon-Nanotube/Poly(vinyl alcohol) Nanocomposites*. *Advanced Functional Materials*, 2005. **15**(6): p. 975-980.
6. Hwang, G.L., Y.-T. Shieh, and K.C. Hwang, *Efficient Load Transfer to Polymer-Grafted Multiwalled Carbon Nanotubes in Polymer Composites*. *Advanced Functional Materials*, 2004. **14**(5): p. 487-491.
7. Zhao, C., et al., *Synthesis and characterization of multi-walled carbon nanotubes reinforced polyamide 6 via in situ polymerization*. *Polymer*, 2005. **46**(14): p. 5125-5132.
8. Gao, J., et al., *Continuous Spinning of a Single-Walled Carbon Nanotube-Nylon Composite Fiber*. *J. Am. Chem. Soc.*, 2005. **127**(11): p. 3847-3854.
9. Putz, K.W., et al., *Elastic modulus of single-walled carbon nanotube/poly(methyl methacrylate) nanocomposites*. *Journal of Polymer Science Part B: Polymer Physics*, 2004. **42**(12): p. 2286-2293.
10. Kumar, S., et al., *Synthesis, Structure, and Properties of PBO/SWNT Composites*. *Macromolecules*, 2002. **35**(24): p. 9039-9043.
11. Park, C., et al., *Dispersion of single wall carbon nanotubes by in situ polymerization under sonication*. *Chemical Physics Letters*, 2002. **364**(3-4): p. 303-308.
12. Velasco-Santos, C., et al., *Improvement of Thermal and Mechanical Properties of Carbon Nanotube Composites through Chemical Functionalization*. *Chem. Mater.*, 2003. **15**(23): p. 4470-4475.
13. Jia, Z., et al., *Study on poly(methyl methacrylate)/carbon nanotube composites*. *Materials Science and Engineering A*, 1999. **271**(1-2): p. 395-400.
14. Qian, D., et al., *Load transfer and deformation mechanisms in carbon nanotube-polystyrene composites*. *Applied Physics Letters*, 2000. **76**(20): p. 2868-2870.
15. Callister, W.D., *Materials Science and Engineering, an Introduction*. 2003, New York: Wiley.
16. Krenchel, H., *Fibre reinforcement*. 1964, Copenhagen: Akademisk Forlag.
17. Halpin, J.C. and J.L. Kardos, *The Halpin-Tsai equations: A review*. *Polymer Engineering & Science*, 1976. **16**(5): p. 344-352.
18. Cox, H.L., *The Elasticity and Strength of Paper and Other Fibrous Materials*. *British Journal of Applied Physics*, 1952. **3**(MAR): p. 72-79.
19. Shaffer, M.S.P. and A.H. Windle, *Fabrication and Characterization of Carbon Nanotube/Poly(vinyl alcohol) Composites*. *Advanced Materials*, 1999. **11**(11): p. 937-941.
20. Coleman, J.N., et al., *High Performance Nanotube-Reinforced Plastics: Understanding the Mechanism of Strength Increase*. *Advanced Functional Materials*, 2004. **14**(8): p. 791-798.
21. Salvétat, J.P., et al., *Elastic modulus of ordered and disordered multiwalled carbon nanotubes*. *Advanced Materials*, 1999. **11**(2): p. 161-165.
22. Cadek, M., et al., *Reinforcement of Polymers with Carbon Nanotubes: The Role of Nanotube Surface Area*. *Nano Lett.*, 2004. **4**(2): p. 353-356.
23. Bai, J., *Evidence of the reinforcement role of chemical vapour deposition multi-walled carbon nanotubes in a polymer matrix*. *Carbon*, 2003. **41**(6): p. 1325-1328.
24. Coleman, J.N., et al., *Small but strong: A review of the mechanical properties of carbon nanotube-polymer composites*. *Carbon*, 2006. **44**(9): p. 1624-1652.

25. Wagner, H.D., et al., *Stress-induced fragmentation of multiwall carbon nanotubes in a polymer matrix*. Applied Physics Letters, 1998. **72**(2): p. 188-190.
26. Cooper, C.A., et al., *Detachment of nanotubes from a polymer matrix*. Applied Physics Letters, 2002. **81**(20): p. 3873-3875.
27. Barber, A.H., S.R. Cohen, and H.D. Wagner, *Measurement of carbon nanotube--polymer interfacial strength*. Applied Physics Letters, 2003. **82**(23): p. 4140-4142.
28. Liao, K. and S. Li, *Interfacial characteristics of a carbon nanotube--polystyrene composite system*. Applied Physics Letters, 2001. **79**(25): p. 4225-4227.
29. Wong, M., et al., *Physical interactions at carbon nanotube-polymer interface*. Polymer, 2003. **44**(25): p. 7757-7764.
30. Yu, M., et al., *Strength and Breaking Mechanism of Multiwalled Carbon Nanotubes Under Tensile Load*. Science, 2000. **287**: p. 637-640.
31. Xie, S., et al., *Mechanical and physical properties on carbon nanotube*. Journal of Physics and Chemistry of Solids, 2000. **61**(7): p. 1153-1158.

Chapter 5: Properties of PLLA and Biosteel Reinforced With Carbon Nanotubes.

5.1 Introduction.

This chapter presents the properties of two biomaterials reinforced with carbon nanotubes fabricated by solution processing. The first part will present the mechanical and thermal properties of Poly (L lactic acid) (PLLA) reinforced with two different types of nanotubes. These are OH functionalised MWNTs and SWNTs functionalised with octadecylamine. The second part of this chapter focuses on the mechanical reinforcement of engineered spider silk (Biosteel) with SWNTs functionalised with octadecylamine.

5.2 PLLA Composites Studies.

5.2.1 Background and Motivations.

Among all biopolymers, PLLA is of special interest. Because of the presence of ester groups, this polymer is susceptible to enzymatic and hydrolytic degradation to form L-Lactid acid, a naturally occurring metabolite in the human body. Additionally, PLLA is U.S Food and Drug Administration approved and available commercially in a variety of grade. In the biomedical field, PLLA has widespread applications in sutures, drug delivery devices, prosthetics, vascular grafts, bone screws, pins, and plates for temporary internal fixation [1, 2]. Good mechanical properties and degradation into non toxic products[3] are the main reasons for such an array of applications. Another factor contributing to the use of PLLA in biomedical applications is its ability to be copolymerised and blended to obtain product with desirable properties. However, its use has been limited because of the cost of production. Recent progress on the production process opened PLLA to new potential applications[4]. One of them is to use PLLA as a scaffold for tissue engineering. The polymer has an in vivo

degradation time of several weeks which gives enough time for the tissue being repaired to regain its structural integrity and function. Adding carbon nanotubes to such a polymer can furthermore help the tissue to regenerate or stimulate cell growth. For example, Supronowicz et al successfully improved osteoblast cells proliferation by electrical stimulation using Polylactic acid CNT composites[5]. Mechanical stimulation using a bioreactor is also necessary to stimulate and improve the properties for tissue engineering[6]. Therefore, the mechanical properties of CNTs can also help the scaffold to sustain the mechanical stimulation. With this in mind, we assessed the potential mechanical reinforcement of PLLA using carbon nanotubes as fillers.

5.2.2 Film Preparations.

Two types of PLLA were used in this study. The first PLLA investigated was purchased from Sigma Aldrich (Mw 100,000-150,000). The second PLLA batch was kindly offered by Purac® (Mw 360,000-365,000 g/mol). These polymers will be referred as PLLA LMW (Low Molecular Weight) and PLLA HMW (High Molecular Weight) for the following presented work. In both cases, polymers were first dissolved in chloroform at a concentration of 30g/l. Then, 1wt% of OH functionalised MWNTs (www.nanocyl.be) were added to the polymer solutions. We used the same batch of nanotubes for this study and the PMMA study. In order to disperse these CNTs, solutions were sonicated by using an ultra high power sonic tip for 1 min. Subsequently, solutions were placed for 2 hours into a low power sonic bath. This was followed by an additional sonication for 1 min using a sonic tip. Solutions were then left undisturbed for 48 hours in order to allow impurities to form a sediment at the bottom of the sample bottle. The resulting solutions, rich in nanotubes, were then decanted while the sediment containing impurities remained at the bottom of the sample bottle.

Solutions were then blended with a PLLA LMW / CHCl₃ and PLLA HWM / CHCl₃ at 30g/l to produce a range of mass fractions. In order to optimise dispersion, every sample bottle with different mass fractions was sonicated for an extra 30 seconds with the sonic tip. 2ml of the various solutions were dropped onto polished Teflon squares and placed into a fume hood at room temperature to allow the solvent to evaporate and form the composite films (fig: 5.1). Due to solvent effects, only 2 layers were produced. More layers would have resulted in a less homogenous film. The samples were then peeled off the Teflon squares and placed in a high

vacuum oven at 900 mbar for 24 hours to remove any solvent which might be trapped in the composites. However, further analysis show 10wt% of residual solvents in the composites films as it will be discussed in this chapter.

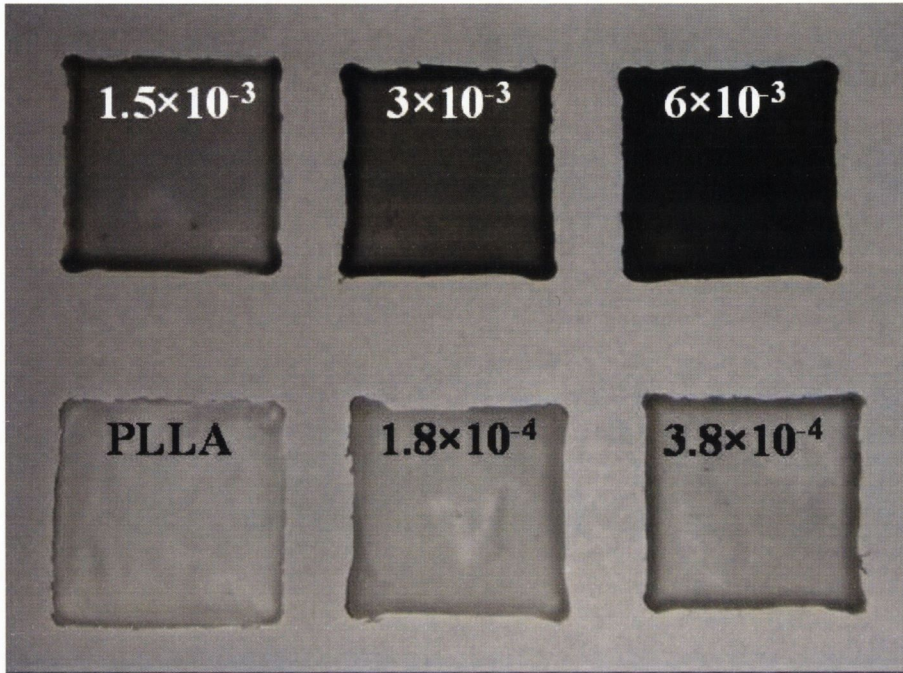


Figure 5.1: Drop-casting PLLA LMW composite films with range of volume fraction of OH functionalised MWNTs from 1.8×10^{-4} to 6×10^{-3} .

The same procedure was used to fabricate PLLA HMW composites with SWNTs functionalised with octadecylamine (www.carbonsolution.com) in chloroform. We chose this alternative batch of nanotubes because, thanks to their functionality, they are well dispersed in organic solvents[7]. Figure 5.2 shows the synthesis of these functionalised SWNTs. These nanotubes will be referred to as P5-SWNTs for the following presented work.

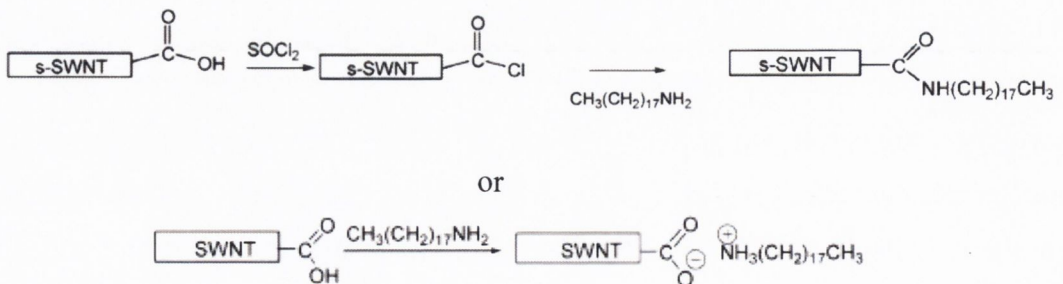
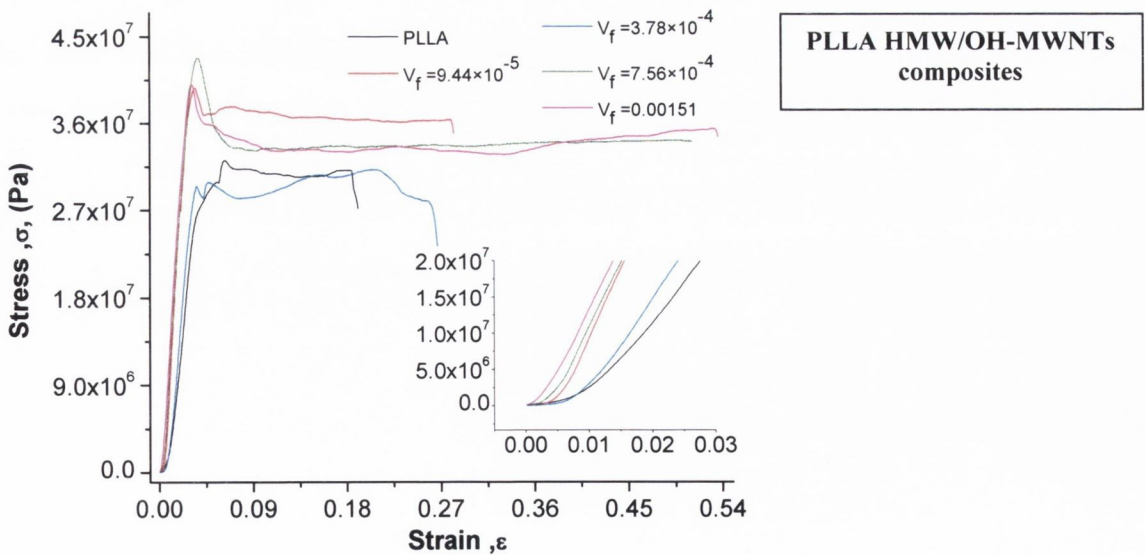
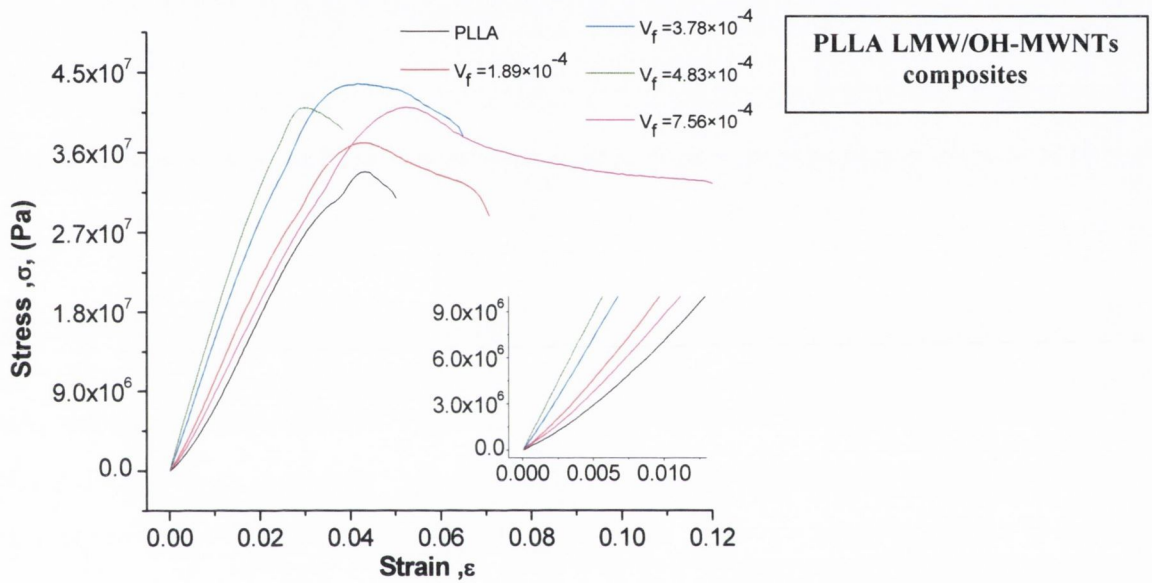


Figure 5.2: Synthesis of SWNTs P5 [7].

5.2.3 Mechanical Characterisations.

Similarly to the PMMA composites, tensile measurements were carried out on PLLA composites by using a Zwick tensile tester Z100. The test conditions were the same as for the PMMA samples (cross head speed $0.5 \text{ mm}\cdot\text{min}^{-1}$). For each volume fraction, and for pristine PLLA, five measurements were performed on five strips ($12 \text{ mm} \times 2.5 \times \text{mm } 60 \mu\text{m}$). Figure 5.3 shows the stress-strain curves of the PLLA composites reinforced with OH-MWNTs and P5-SWNTs respectively. To calculate the volume fraction of nanotubes presented in the following results, densities of 2150 kgm^{-3} , 1500 kgm^{-3} and 1300kgm^{-3} were used for OH-MWNTs, P5-SWNTs and polymer respectively[8].



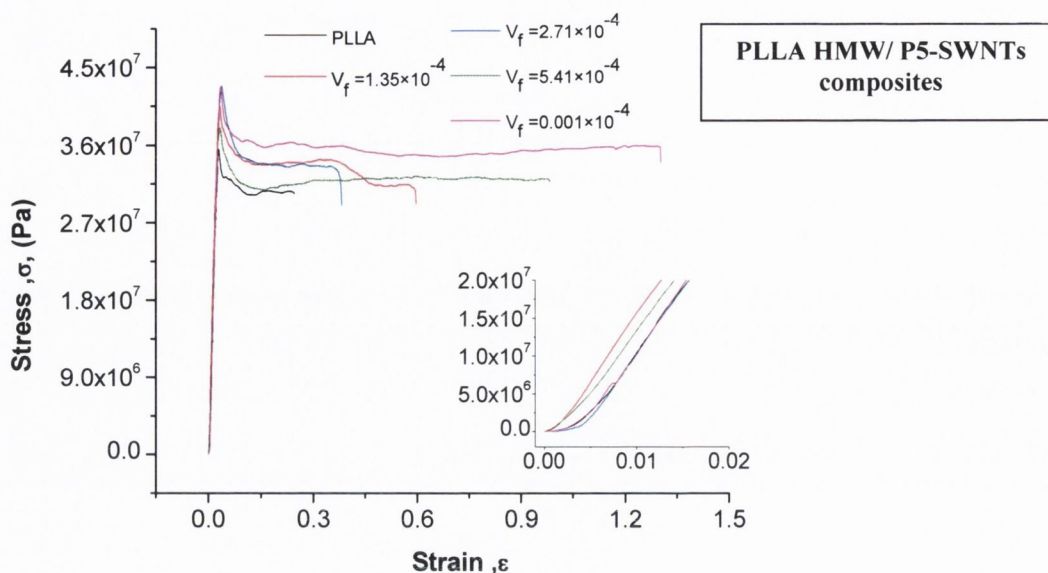


Figure 5.3: Representative stress-strain curves for PLLA/CNTs composites for a range of volume fractions of nanotubes.

Both PLLA LMW and PLLA HMW composites exhibit typical viscoelastic behaviour of semi-crystalline materials. However, they present some dramatic changes in their plastic deformations. For example, average strain at break ϵ_B calculated from Pristine PLLA LMW and PLLA HMW gives a value of ϵ_B equal to 4.4 ± 2.4 % and 45 ± 21 % respectively. Furthermore, adding CNTs also increases ϵ_B dramatically in each case investigated. For a loading level of $1.5 \times 10^{-3} V_f$ of OH-MWNTs into PLLA LMW, ϵ_B undergoes an almost linear increase up to 12 % strain. This represents an increase of 177%. With the PLLA HMW matrix, this increase is 69 % by adding $7.5 \times 10^{-4} V_f$ of OH-MWNTs and 264% by adding $2.1 \times 10^{-3} V_f$ of P5-SWNTs (fig: 5.4). It should be pointed out that the reds line from figure 4 are not fits but guide to eye to show the trend of the increase.

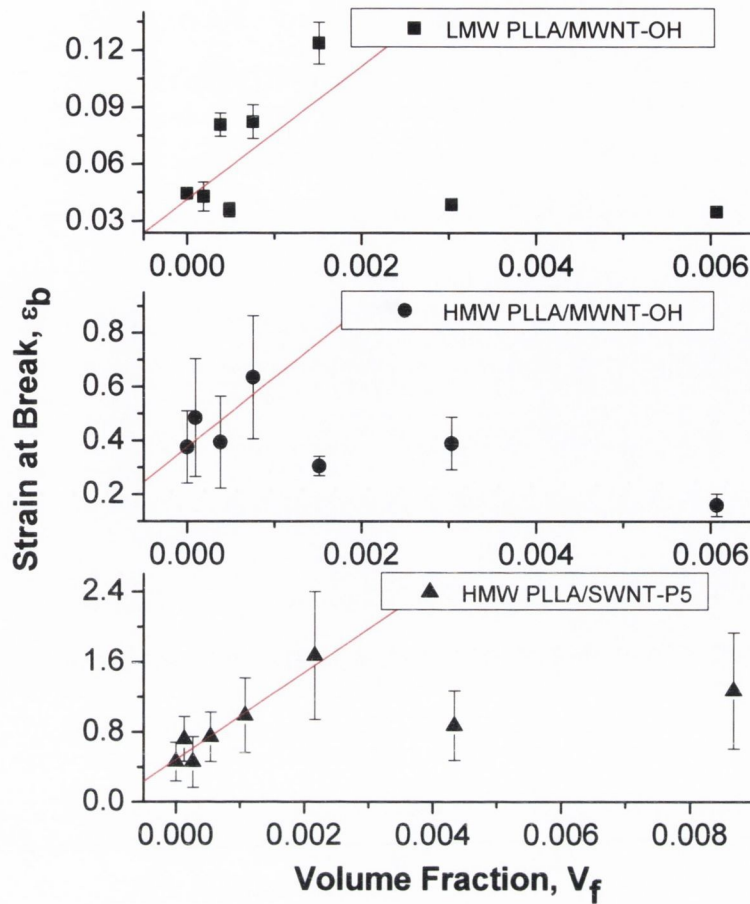


Figure 5.4: Strain at break of PLLA/CNTs composites as a function of volume fraction of carbon nanotubes with the corresponding standard error.

Khan et al used the same batch of P5-SWNTs to make Polyvinyl chloride (PVC) composites by solution mixing and drop-cast techniques[9]. With this system, they also recorded a dramatic increase of 178% for ϵ_B by adding a volume fraction of 2.38×10^{-5} .

The Young's modulus increases linearly by more than 45% from 1.08 ± 0.006 GPa for the pristine PLLA LMW up to 1.57 ± 0.44 GPa with a volume fraction of OH-MWNTs of 4.8×10^{-4} . This increase corresponds to a dY/dV_f of 841 ± 72 GPa. Chen et al. also used PLLA (Mw 160,000) with OH-MWNTs. In this study, they prepared two types of composites, PLLA/OH-MWNTs and PLLA mixed with OH-MWNTs grafted PLLA (OH-MWNTs-g-PLLA). In both cases, films were made by hot pressed sheets processing [10]. By adding 0.006 V_f of OH-MWNTs and OH-MWNTs-g-PLLA, the Young's modulus improved by 14% and 51% respectively. This corresponds to a dY/dV_f of 81 GPa and 375 GPa.

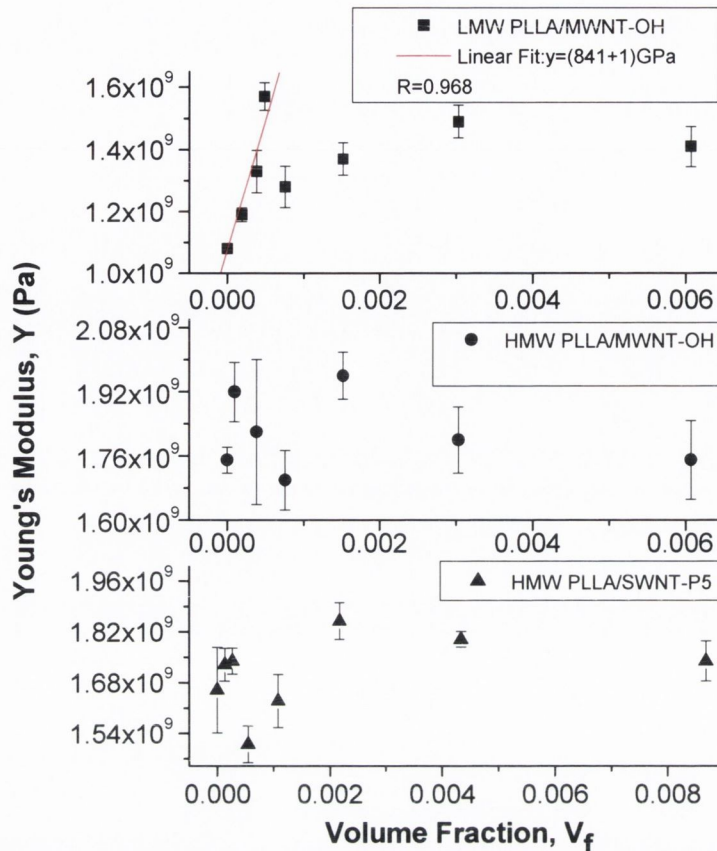


Figure 5.5 Young's Modulus for PLLA/CNTs composites as a function of volume fraction of carbon nanotubes with the corresponding standard error.

No linear increases were observed for PLLA HMW/CNTs composites as seen in Figure 5.5. This could be due to the long molecular weight of the polymer. As a result, the system may be highly entangled with a lower CNTs dispersion. However, both P5-SWNTs and OH-MWNTS PLLA films present a small increase in the stiffness of 11% and 12 % respectively. For pristine PLLA LMW and PLLA HMW, Y is 1.08 ± 0.006 GPa and 1.66 ± 1.18 GPa respectively. Moon et al. also investigated the mechanical properties of PLLA HMW ($M_w 300000 \text{ gmol}^{-1}$) composites[11]. They prepared composite films by solution mixing and drop-casting of PLLA with catalytic MWNTs. After being folded and broken, cast films were hot pressed. By adding $0.018V_f$ of MWNTs they improved the Young's modulus by 140% from 1GPa to 2.4GPa. Comparing with our results, it may suggest that a higher loading level of CNTs is required to improve mechanical reinforcement. Khan et al obtained a linear increase in PVC composites up to a volume fraction of 6.6×10^{-5} [9]. This also corresponds to a small increase of 35%. However, they obtained a dramatic dY/dV_f of 7 ± 3 TPa. This clearly shows that effective reinforcement can be achieved at very low content of CNTs.

Since a linear increase in the Young's modulus only occurred for PLLA LMW/CNTs composites, we used the Krenchel's rule of mixtures and Halpin-Tsai equations to fit our experimental values. Because PLLA films were fabricated by solution drop-casting we used the same theoretical parameters to calculate the enhancement of the Young's modulus of PMMA composites. Taking $Y_p=1.08$ GPa, dY/dV_f was found to be 94.5 ± 91.8 GPa using Krenchel's rule of mixtures (equations 4.2 4.3). Halpin-Tsai model (equations 4.5) gave a dY/dV_f of 26.3 ± 21.1 GPa. Comparing this results with our experimental value of $dY/dV_f = 841\pm 72$ GPa, it can be concluded than these models do not explain the strong increase in the elastic modulus observed at low volume fraction of nanotubes.

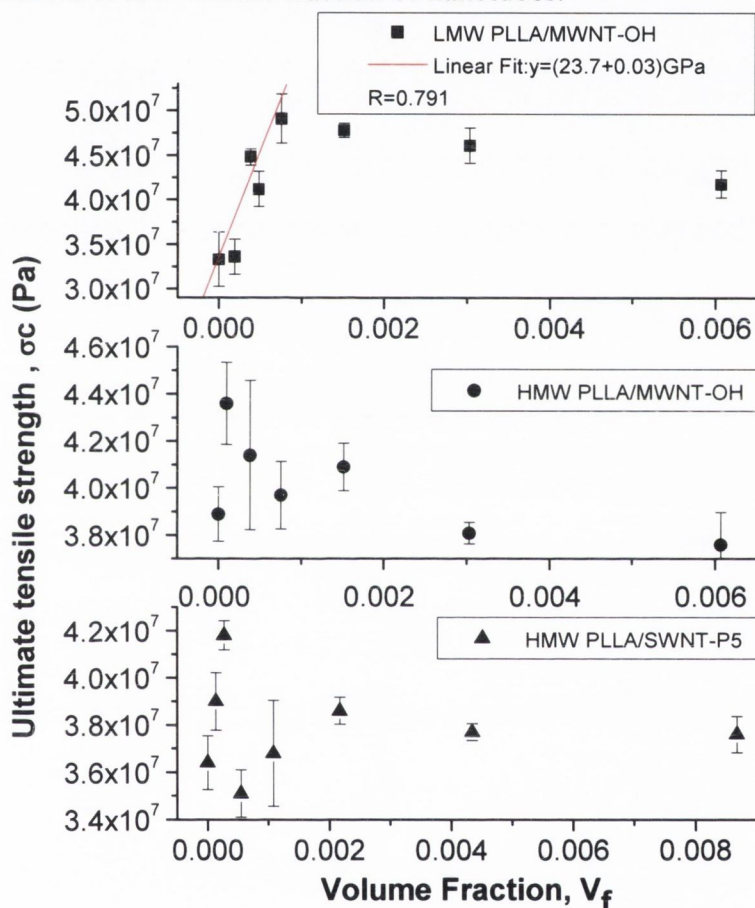


Figure 5.6: Ultimate tensile strength for PLLA/CNTs composites as a function of volume fraction of carbon nanotubes with the corresponding standard error.

Similarly, a linear increase was only observed in the ultimate tensile strength at low volume fraction of nanotubes in PLLA LMW composites up to a volume fraction of 4.8×10^{-4} V_f (fig: 5.6). Afterwards, the reinforcement decreased which may be attributed to nanotube aggregations. Up to this optimum volume fraction, σ_c increases by more than 47% from

33.3±3 MPa for pristine PLLA up to 49.1±2.7 MPa. This gives a $d\sigma_c/dV_f$ of 23.7±4.6 GPa. Chen et al, improved the tensile strength by 14 % and 51% adding 0.006 V_f of OH-MWNTs and OH-MWNTs-g-PLLA [10]. The corresponding $d\sigma_c/dV_f$ are 1.3GPa and 4.8GPa respectively. Using PLLA HMW, there is a small increase in σ_c by adding both types of P5 and OH functionalised nanotubes, however, no significant trend can be observed. With less than 2.7×10^{-4} V_f of P5-SWNTs, σ_c increases by 14% from 36.4 ±1.1 MPa. up to 41.8±0.6 MPa. Khan et al reported a linear increase of 13 % by adding up to 6.6×10^{-5} volume fraction of P5-SWNTs to PVC[9]. This corresponds to a $d\sigma_c/dV_f$ of 80±20 GPa. Using the OH-MWNTs batch, this increase is about 12% from 38.9±1.1 MPa up to 43.6±1.7 MPa with a volume fraction of 1.35×10^{-4} . In PLLA LMW/OH-MWNTs composites, the breaking strength, σ_B , also exhibits a linear increase up to an optimum volume fraction before decreasing (fig: 5.7). In this case, $d\sigma_B/dV_f$ was found be 12.5±3.4 GPa. This corresponds to an increase of 42% from 30.5±2.7 MPa to 43.4±1.5 MPa for a maximum CNT V_f of 0.003.

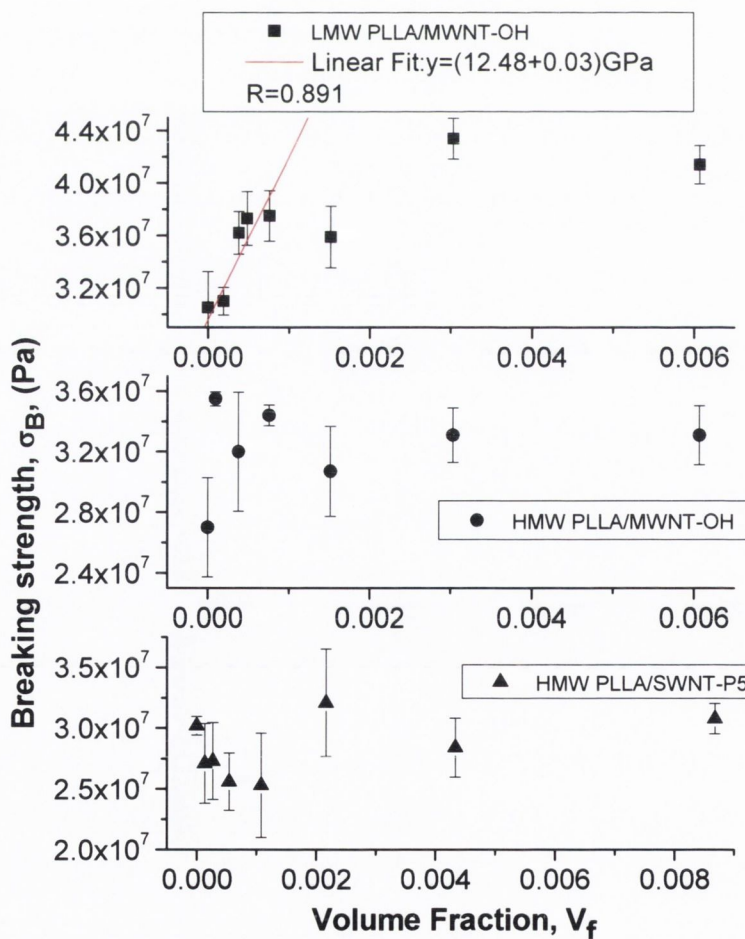


Figure 5.7: Breaking strength for PLLA/CNTs composites as a function of volume fraction of carbon nanotubes with the corresponding standard error.

With PLLA HMW/OH-MWNTs composites, σ_B only increases by 31% from 27 ± 3.2 GPa for pristine PLLA up to 35.5 ± 0.4 GPa with 9.45×10^{-5} V_f of nanotubes. An even smaller increase of 6% is observed with PLLA HMW/P5-SWNTs composites from 30.2 ± 0.7 to 32.1 ± 4.4 MPa with a volume fraction of 0.0021.

We used inequation 4.9 from the pervious chapter to fit the linear increase observed in the PLLA LMW/OH-MWNTs composites. The interfacial shear strength, τ , was found to be 169.6 ± 155.6 MPa. This is an interesting result because it falls in the expected range of values for catalytic nanotubes (50-100MPa). The calculated τ , within its error, also falls in the expected range of the polymer shear strength for PLLA LMW (30.5 MPa). This may suggest than the strength of fiber-reinforced composites described by the rule of mixtures (equation 4.6) is a valid model to fit our experimental data. This model could not be used for the PLLA high molecular weight composites because of the absence of linear increase in this investigated mechanical parameter.

There is a dramatic increase in the toughness of the composites upon the addition of CNTs. This is clearly visible from the stress strain curves where a small content of nanotubes induces a large plastic deformation when compared to pristine PLLA for both molecular weights (fig: 5.3). For example, the improvement in toughness was recorded to be more than 225 % by adding 2.1×10^{-3} V_f of P5-SWNTs to PLLA HMW as shown in Figure 5.8. Khan et al. reported an even higher increase of 384% in the toughness by adding $6.6 \times 10^{-5} \times 10^{-3}$ V_f of P5-SWNTs to PVC[9]. This may suggest that P5-SWNTs could act as plasticisers in thermoplastics polymers. This is underlined by the fact that stiffness and the tensile strength present a small increase in PLLA and PVC. OH-MWNTs also improve the toughness for both PLLA types investigated. However, this increase is much higher in the case of PLLA LMW than PLLA HMW (281% and 30% respectively). The reinforcement is achieved for a volume fraction of 1.5×10^{-3} and 9.4×10^{-5} for low and high molecular weight PLLA respectively. This is an unexpected result since we used the exactly same batch of CNTs.

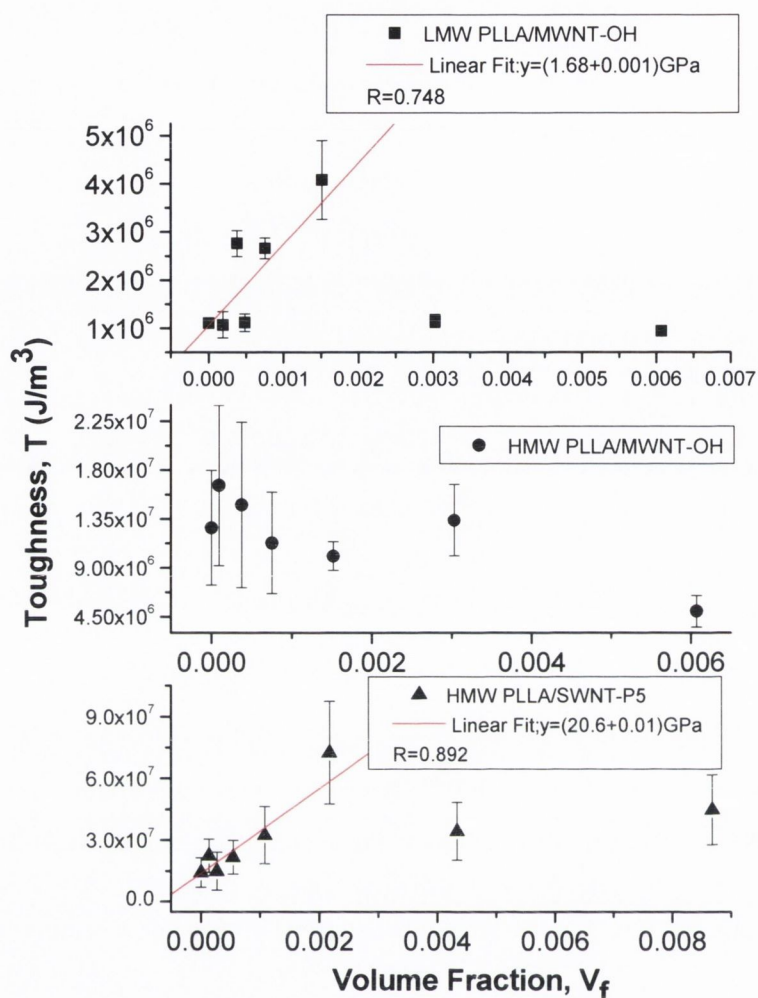


Figure 5.8: Toughness for PLLA/CNTs composites as a function of volume fraction of carbon nanotubes with the corresponding standard error.

5.2.4 Thermal Characterisations.

Thermal analysis using TGA and DSC were carried out on PLLA LMW composites to determine if the linear increase in the mechanical properties at low volume fraction of nanotubes also affects the thermal properties of these composites.

5.2.4.1 Thermogravimetric Analysis.

All TGA runs were achieved by heating 5 mg of each investigated sample from 30°C to 900°C at a heating rate of 10°C /min. This was performed under a constant air flow of 20

L/min. Figure 5.9 shows the decomposition behaviour of all the PLLA LMW composites and also of the OH-MWNTs.

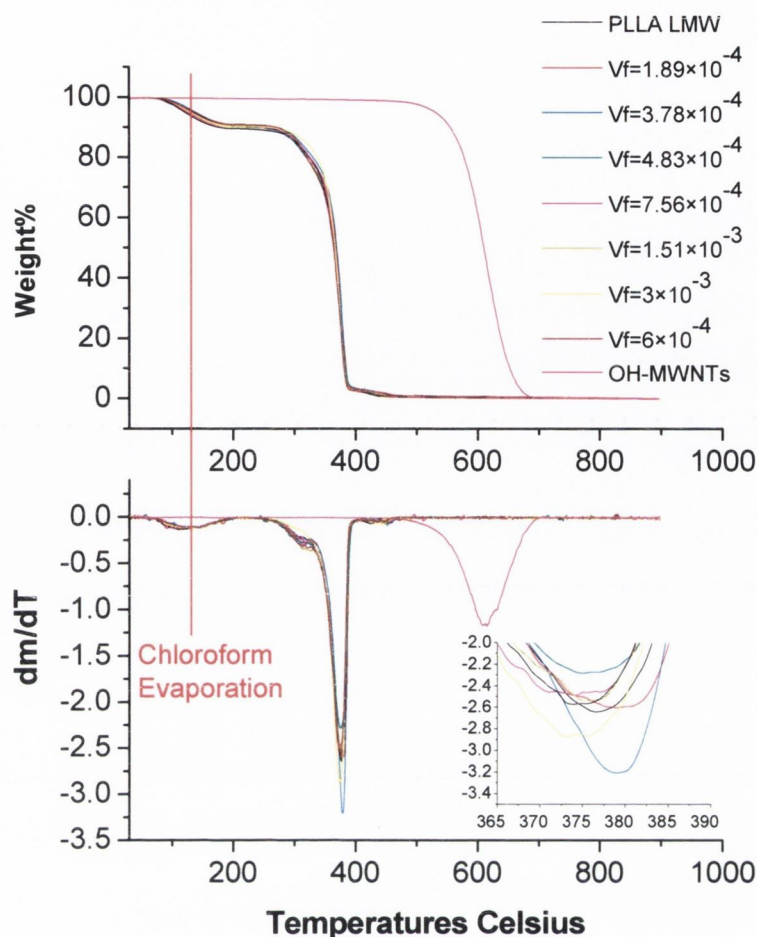


Figure 5.9: Weight loss versus temperature for PLLA LMW composites and OH-MWNTs and their first derivatives.

The first derivative curves of pristine PLLA and PLLA composites present their first peak around 125°C. This corresponds to the evaporation of the chloroform which remained in the PLLA drop-cast films. The mass of the solvent is about 10% of the total mass of the composite films. As discussed in the previous chapter, the presence of residual solvent may have an effect on the mechanical properties of the films. The second peak (~375°C) can be attributed to the thermal degradation of the PLLA. It is quite clear from the inset that adding CNTs does not change the thermal degradation of the polymer. The third peak seen in Figure 5.9 represents the thermal degradation of OH-MWNTs. The peak is not visible in the degradation curve of PLLA composites because of their very low nanotube content.

5.2.4.2 Differential Scanning Calorimetry Analysis.

DSC runs were performed on PLLA LMW/OH-MWNTs to assess changes in the glass transition and the percentage of crystallinity χ . Previous work has shown that the mechanical reinforcement in the thermoplastic polymer (PVA) was directly correlated to the increase in the crystallinity by adding a CNT filler [12, 13]. They show that CNTs were inducing a crystalline coating of PVA resulting in the maximisation of the interfacial stress transfer.

We used the following program to carry out DSC measurement:

- Two heat up scans from -0°C to 250°C at $10^{\circ}\text{C}/\text{min}$
- One cooling down scan from 250°C to 0°C at $100^{\circ}\text{C}/\text{min}$

Figure 5.10 displays curves of the 1st and the 2nd heat programme achieved on PLLA composites. We only represented the curves of the PLLA composites with $0.006 V_f$ since all samples investigated including the pristine PLLA present similar curves.

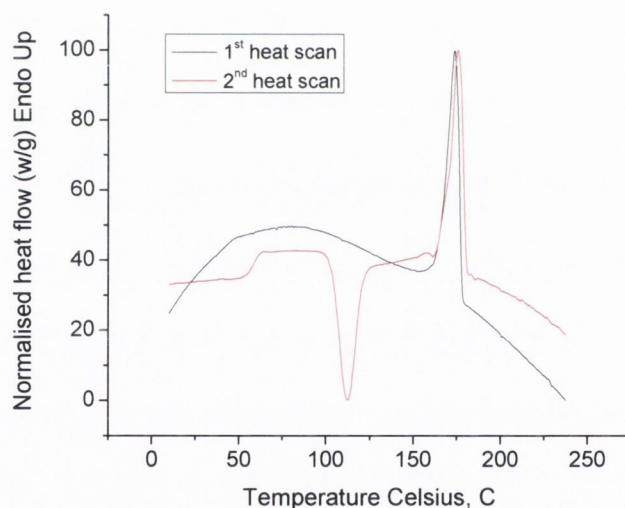


Figure 5.10: 1st and 2nd heat scan of PLLA LMW composites with 0.006 volume fraction of OH-MWNTs.

No glass transition is observed in the first heat scan. This can be explained by the fact that the evaporation of the chloroform trapped in the drop-cast films display a broad first transition (endothermic peak) which hides the second transition i.e. the T_g . No cold crystallisation is occurring also during the first run. This can be attributed to the chloroform evaporation which disables partial crystallisation of polymer chains above the glass transition. The peak at 170°C represents the melting temperature (T_m) where the crystalline regions of the polymer start to melt. The second scan displays a typical DSC curve for semi-crystalline polymer. T_g occurs at

approximately 55°C. This is followed by a cold crystallisation at around 110°C. T_m occurs at around 170°C.

Using equation 3.3 and taking $\Delta H_{100\%}$ at 93.7 J/g[14] we calculated the percentage crystallinity, χ , and the glass transition from the 1st DSC scan for all the PLLA LMW composites (fig: 5.11).

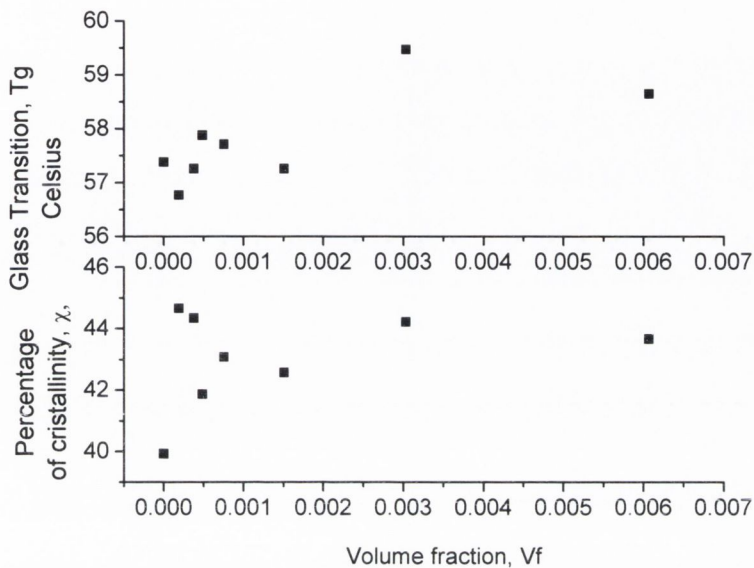


Figure 5.11: Glass transition and percentage crystallinity of PLLA LMW composites as a function of volume fraction of of OH-MWNTs.

From Figure 5.11, χ appears to increase by adding CNTs. However this increase is not linear and does not follow the linear increase observed in the Young's modulus (fig:5.5). The maximum increase recorded is only 11% by adding 1.8×10^{-4} volume fraction of CNTs. Coleman et al obtained a linear increase in the percentage crystallinity which matched the increase in the stiffness[12]. In this case the maximum increase obtained was ~240% for a volume fraction of 6×10^{-3} of catalytic thin MWNTs. This suggests that OH-MWNTs do not induce crystallisation of PLLA with the same magnitude as in the PVA study. This is not an unexpected result since the OH functionalisation must disable the capacity of the polymer to wrap around the nanotube to some extent.

T_g calculated from the DSC shows a general trend where the T_g increases with increasing nanotube content, but this increase is relatively small. The highest increase is obtained with 0.3vol % where the T_g only increases by 2°C.

5.2.5 Conclusion.

We successfully produced low and high molecular weight PLLA composites with OH-MWNTs and P5-SWNTs by solution mixing and drop-casting techniques. The best mechanical reinforcement was achieved with PLLA LMW/OH-MWNTs composites. In this case, all the mechanical parameters investigated (Y , σ_C , σ_B , ϵ_B , T) show a linear increase up to an optimum volume fraction of nanotubes before falling off due to aggregation effects. Using the strength of fibre-reinforced composites described by the rule of mixtures (equation 4.6) gives an acceptable value for τ (169.6 ± 155.6 MPa). This suggests that this model is valid for explaining the mechanical reinforcement. Thermal analysis has shown that nanotubes did not have an effect on the thermal degradation. Moreover, the glass transition and the percentage crystallinity did not undergo dramatic changes by adding CNTs. Using the same batch of OH-MWNTs with high molecular weight PLLA shows a lower mechanical reinforcement than the PLLA LMW composites. One possible explanation is that long molecular chains may decrease a good dispersion of CNTs resulting in poor mechanical reinforcement. Using P5 SWNTs with PLLA HMW also showed low reinforcement in the stiffness and the strength. However, strain at break and toughness exhibited a dramatic increase of 264% and 225% respectively by adding 0.21 V_f % of CNTs. Similar behaviour occurred using PVC as a matrix[9]. This suggests that the functionalisation of these nanotubes (ODA) may act as a plasticiser. All the mechanical properties investigated using a tensile tester are summarised in the table 5.1.

	PLLA LMW OH-MWNTs	PLLA HMW OH-MWNTs	PLLA HMW P5-MWNTs
Young's Modulus GPa	$dY/dV_f=841\pm72$ 45% increase from 1.08 to 1.57 $V_f=4.8\times10^{-4}$	12% increase from 1.75 to 1.96 $V_f=1.5\times10^{-3}$	11% increase from 1.66 to 1.85 $V_f=2.1\times10^{-3}$
Ultimate Tensile Strength GPa	$d\sigma_c/dV_f=23.7\pm4.6$ 47% increase from 0.033 to 0.049 $V_f=7.5\times10^{-4}$	12% increase from 0.038 to 0.043 $V_f=1.3\times10^{-4}$	14% increase from 0.036 to 0.041 $V_f=2.7\times10^{-4}$
Breaking Strength GPa	$d\sigma_B/dV_f=12.4\pm3.3$ 42% increase from 0.03 to 0.043 $V_f=3\times10^{-3}$	31% increase from 0.027 to 0.035 $V_f=9.4\times10^{-5}$	6% increase from 0.03 to 0.032 $V_f=2.1\times10^{-3}$
Toughness MJ/m³	$dT/dV_f=1680\pm248$ 281% increase from 1.07 to 4.08 $V_f=1.5\times10^{-3}$	30% increase from 12.7 to 1.66 $V_f=9.4\times10^{-5}$	225% increase from 22.3 to 72.5 $V_f=2.1\times10^{-3}$
Strain at Break	$d\varepsilon_B/dV_f=35\pm5.6$ 177% increase from 0.04 to 0.12 $V_f=1.5\times10^{-3}$	69% increase from 0.37 to 0.63 $V_f=7.5\times10^{-4}$	264% increase from 0.45 to 1.67 $V_f=2.1\times10^{-3}$

Table.5.1: Summary of the mechanical properties of PLLA/CNT composites.

5.3 Biosteel Composite Studies

5.3.1 Introduction.

Even in the twenty first century, spider silk remains one of the most impressive of structural materials. The product of 400 million years of evolution, spider silk is produced in a variety of forms, each extremely well adapted to the task for which that have been developed. For example, spider dragline silks display values of Young's modulus, strength and toughness of 10 GPa, ~1 GPa and 160 MJ/m³ respectively, perfectly suited for use as web frames, guy lines or tethers[15]. In contrast, viscid silks of the types used in the web spirals are strong and tough but extremely compliant, ideal for catching insects[16]. While spider silk would be ideal for a range of commercial and medical applications, native silk cannot be harvested due to our failure to domesticate spiders. Silkworm silk has traditionally been used as a substitute. However, its mechanical properties are generally inferior to spider silk[16]. Recently, a major breakthrough has been made with the demonstration of the production of silk via protein synthesis in mammalian cells[17]. This product, selling under the name of Biosteel®, can be dissolved and coagulation spun into fibres which display similar mechanical properties to natural spider dragline silk [17].

Progress toward strong, tough fibres has also been made by embedding carbon nanotubes in polymer matrices. Nanotubes are hollow nanoscale carbon cylinders that display immense strength (~60 GPa) and stiffness (~1 TPa)[18]. Coupled with their large aspect ratio, these mechanical properties make nanotubes ideal fillers for reinforcing polymers. By coagulation spinning fibres from polymer-nanotube composite dispersions, materials with strength of ~1GPa and a toughness approaching 731.9 MJ/m³ have been demonstrated [19, 20].

These nanotube based composite fibres share much in common with spider silk. The mechanisms behind the superlative mechanical properties are similar in both cases. In nanotube based composites, stress is transferred from the polymer matrix to the nanotubes. This, coupled with extensive reorganisation of the matrix at high applied stress results in high toughness. In silks the same mechanisms apply, with protein crystallites playing the role of the nanotubes and disordered regions acting as the matrix[15].

With this in mind, it seems obvious to attempt to incorporate nanotubes into a silk like material. For the silk-like material we chose the synthetic spider silk, Biosteel. Functionalised nanotubes were chosen. The nature of the functionality was determined by the requirement that both nanotubes and Biosteel should be soluble in the same solvent. We produced composites based on Biosteel with a range of nanotube mass fractions using a drop casting technique. Films formed were then investigated using tensile measurements to assess potential mechanical reinforcement.

5.3.2 Film Preparation.

For this study, composites were prepared using Biosteel powder[17] purchased from Nexia Biotechnologies Inc (www.nexiabiotech.com) and SWNTs functionalised with octadecylamine from Carbon Solutions Inc, (www.carbonsolution.com). Firstly, Biosteel powder was dispersed at a concentration of 30g.L^{-1} in 1,1,1,3,3,3-Hexafluoro-2-propanol using a high power sonic tip (120W, 60kHz) for two minutes followed by a mild sonication in a sonic bath for two hours. Then SWNTs were added at a mass fraction of 0.5 wt% of the biosteel mass and dispersed using an extra two minutes with a high power sonic tip followed by two hours in a sonic bath. Afterwards this primary solution was blended with a solution of Biosteel at 30g.L^{-1} to produce a range of mass fractions down to 0.031wt%. After blending, an extra sonication process was carried out on each sample with a high power sonic tip and sonic bath using the same time treatment as before. Free standing films were fabricated by dropping 1.5 mL of each solution onto a polished Teflon square which was placed in a vacuum oven for 24 hours to allow the evaporation of the solvent. This procedure was repeated three times in order to obtain an average film thickness of $75\ \mu\text{m}$ (fig: 5.12). The films were then peeled from the substrate and cut into strips of $10\text{mm}\times 2.5\text{mm}\times 75\mu\text{m}$. The width and thickness of each strip were measured using a low torque digital micrometer. For each sample, nanotube mass fractions were converted into volume fraction, V_f , using densities of $1500\ \text{kg/m}^3$ and $1100\ \text{kg/m}^3$ for nanotubes and Biosteel respectively.

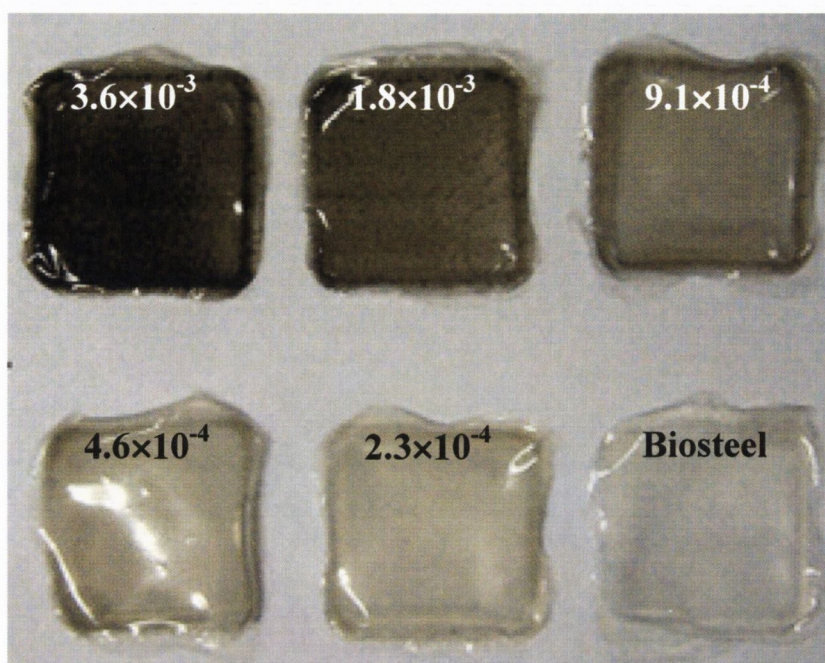


Figure 5.12.: Drop-casting Biosteel composite films with range of volume fractions of P5 functionalised SWNTs from 2.3×10^{-4} to 3.6×10^{-3} .

5.3.3 Mechanical Characterisations.

Mechanical tests were performed using a Zwick tensile tester Z100 using a 100N load cell with a cross-head speed of 1 mm min^{-1} . For each volume fraction, stress strain measurements were made on five strips. From each set of five curves, the Young's modulus (Y), tensile strength (σ_B), strain at break (ϵ_B) and toughness (T) were measured and the mean and standard error calculated.

Photographs of the films are shown in Figure 5.12. Biosteel appears as a transparent film. Addition of small amounts of nanotubes results in a darkening of the film without any loss of uniformity. However, above a volume fraction of 1.8×10^{-3} , small nanotube aggregates are clearly visible. At a volume fraction of 1.8×10^{-3} , the average nanotube centre to centre distance within the film is $\sim 75 \text{ nm}$. As the nanotubes used here are $\sim 1 \text{ micron}$ long it is not surprising that inter-nanotube contact may result in the drying phase resulting in aggregation in higher volume fraction films.

Representative stress-strain curves for the materials studied in this work are shown in Figure 5.13.

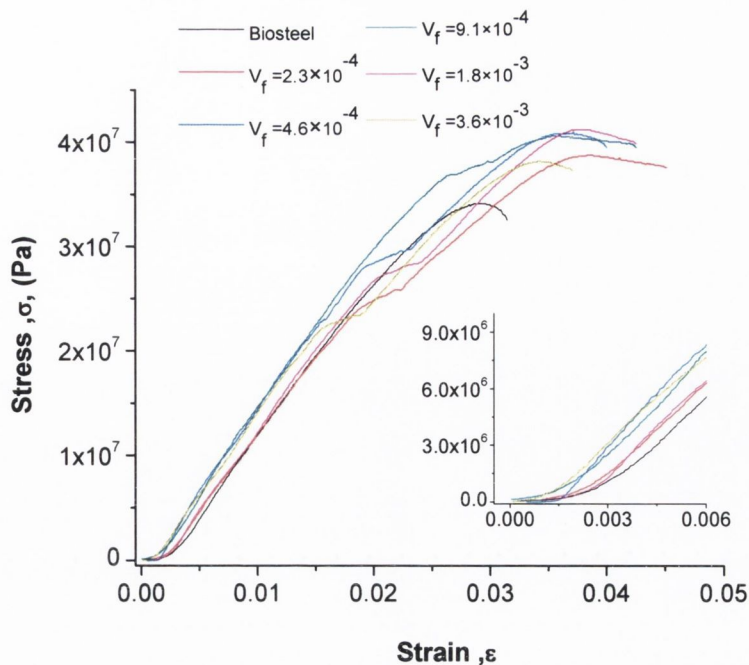


Figure 5.13: Representative stress-strain curves for Biosteel composites for a range of volume fractions of nanotubes.

The Biosteel films display elastic behaviour up to strains of $\sim 2.5\%$ before deforming plastically up to fracture at $\sim 3.1\%$. The Young's modulus, strength and toughness of the Biosteel films were 1.6 GPa, 36.5 MPa and 1.87 MJ/m^3 respectively. These values are significantly larger than those observed for as-prepared, coagulation spun Biosteel fibres ($<1.3 \text{ GPa}$, $<2.3 \text{ MPa}$, $<1.1 \text{ MJ/m}^3$ respectively)[17]. However, it should be pointed out that the fibre results improved dramatically[17] on post-spinning drawing, reaching moduli and strengths of 4-10 GPa and 160-200 MPa respectively. Such coagulation spun fibres also exhibited plastic deformation up to 130% strain and so possessed extremely large toughness's of 55-88 MJ/m^3 . In comparison, natural silk produced in the major ampullate (MA) gland of the spider *Araneus diadematus* displays stiffness, strength, toughness and strain at break of 10 GPa, 1.1 GPa, $\sim 160 \text{ MJ/m}^3$ and 0.27 [16]. These impressive values are due to the presence of alanine rich crystalline domains which act to reinforce all natural silks[15, 16, 21]. Post-drawing of regenerated silks, especially in the presence of water results in the reorganisation of the protein secondary structure, increasing the crystalline fraction and improving the mechanical properties[21]. Dissolution of proteins in strong denaturing solvents such as 1,1,1,3,3,3-Hexafluoro-2-propanol is known to disrupt the secondary structure resulting in low crystalline fraction[17, 21]. Thus the mechanical properties observed for the Biosteel films produced in this work are consistent with silk-like materials with high amorphous content. Interestingly,

our mechanical properties are better than lightly drawn regenerated spider silk (*Nephilia clavipes*, MA gland)[21].

The composite samples display broadly similar stress strain curves to the pure Biosteel. However, adding small amounts of nanotubes results in significant improvements in the four main mechanical parameters: Y , σ_c , T , ϵ_b . The means and standard errors of all four quantities are shown as a function of nanotube volume fraction in Figure 5.14. At low volume fractions, all four parameters increase linearly up to an optimum volume fraction of $\sim 10^{-3}$, followed by a decrease in all parameters at a higher nanotube content. This optimal volume fraction is consistent with the maximum aggregate free volume fraction (fig: 5.12). The reduction in all mechanical properties above this concentration underlines the importance of nanotube dispersion for mechanical reinforcement[22].

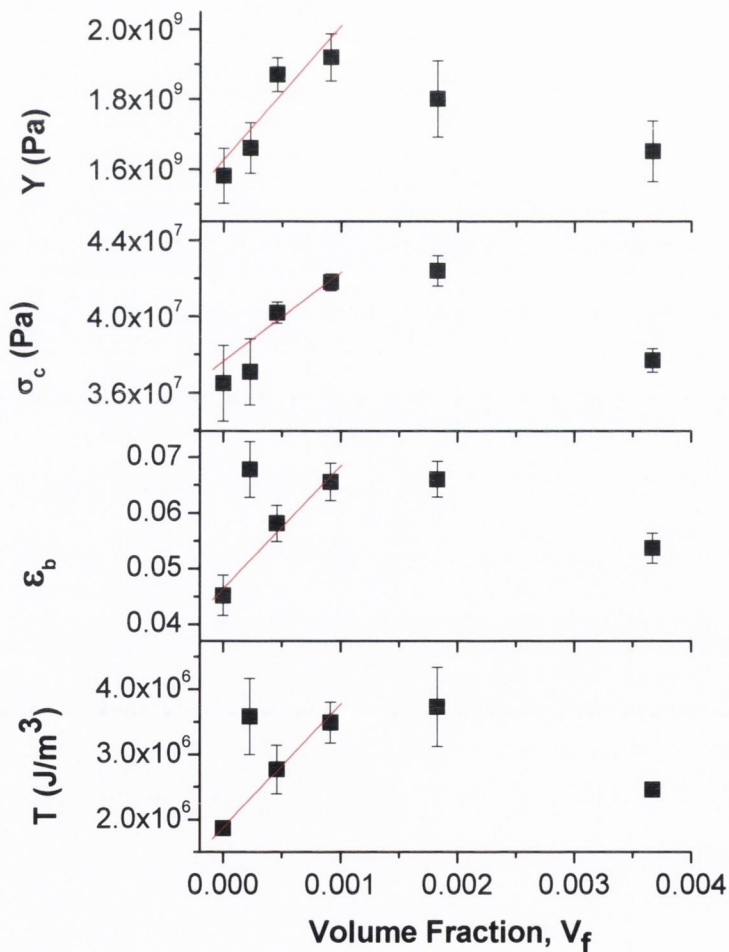


Figure 5.14: Mechanical properties of Biosteel composites for a range of volume fractions of nanotubes with the corresponding standard error.

The Young's modulus increases linearly with volume fraction as predicted by the rule of mixtures[23, 24], reaching 1.9 GPa at the optimum loading level. The rate of increase (dY/dV_f) was found to be 380 ± 100 GPa. For arc discharged SWNTs such as those used in this study, the maximum value of Y_{Eff} is approximately 1 TPa[18, 25]. Taking this value, we can calculate the theoretical dY/dV_f from the rule of mixtures using equations 4.2 and 4.3, as previously described in chapter four. We obtained a maximum value of dY/dV_f to be $\sim 373.4\pm 56.6$ GPa. This value is identical to the experimental value indicating that the stress in the nanotubes is maximised over a significant fraction of their lengths[22]. For micron length nanotubes, this can only happen if the interfacial shear strength is very large, evidence of the effectiveness of the functional groups at transferring stress from the matrix to the nanotubes. Ayutsede et al also made composite fibres by using Bombyx mori silk and SWNTs [26]. By adding 1wt.% of unfunctionalised SWNTs, they improved the Young's modulus from 312 MPa to 705 MPa, equivalent to $dY/dV_f=44.6$ GPa. Their value is much lower than the value of $dY/dV_f=380$ GPa measured in this work. This is further evidence of the importance of attaching appropriate functional groups to any potential mechanical filler material.

Measurements on diameter and length of P5-SWNTs were achieved by a group member Johnny Amiran using AFM. An average value was found to be $\sim 3.6\pm 0.1$ nm and 1.3 ± 0.5 μm for the diameter and the length respectively. Using these values and the Halpin-Tsai model (equation 4.5) dY/dV_f was calculated to be 203.3 ± 88.6 GPa. This is lower than the experimental value by ~ 100 GPa.

The ultimate tensile strength increased linearly with volume fraction from 36.5 MPa (Biosteel) up to 41.8 MPa at a volume fraction of 9.1×10^{-4} . This corresponds to a rate of increase of $d\sigma_c/dV_f=4.7\pm 1.3$ GPa. This value is smaller than expected as the maximum possible value approaches the nanotube strength ie ~ 50 GPa. It is not clear what the reason for this discrepancy is.

The average breaking strain of Biosteel films was 4.5%. While this value is low compared to silks in general[16] and treated Biosteel fibres in particular[17], this brittleness is not unexpected. Regenerated spider silk fibres prepared in the absence of any water have been observed to be brittle, breaking at strains of 4-8%[21]. What is surprising is the fact that addition of a volume fraction of 9.1×10^{-4} nanotubes resulted in an increase in the average strain at break from 4.5% to 6.5 %. This is unexpected as addition of nanotubes to a polymer generally reduces the ductility[22]. However this increase in ductility, coupled with the

strength increases translates into an increase in the fibre toughness. The toughness increased linearly from 1.87 MJ/m^3 for the Biosteel up to 3.48 MJ/m^3 for the sample containing a V_f of 1.8×10^{-3} . This is a dramatic increase for a very small content of nanotubes. Previous work by Ayutsede, showed a dramatic drop in toughness from $\sim 0.58 \text{ MJ/m}^3$ for a film of electrospun regenerated *Bombyx mori* silk to $\sim 0.02 \text{ MJ/M}^3$ at a loading level of 0.5% [26].

It should be pointed out that there are two problems with this work: the mechanical properties saturate at low loading levels and the absence of crystalline protein results in significantly reduced mechanical properties compared to natural silk. The first of these problems could be addressed by careful choice of functional group. The ODA functionalised nanotubes were chosen from a very limited (commercially available) selection on the basis that they could be dispersed in 1,1,1,3,3,3-Hexafluoro-2-propanol and so blended with the Biosteel. While co-solubility demonstrates a certain level of compatibility between ODA and Biosteel (similar Hildebrand parameters) we believe that a careful choice of functional group could lead to better compatibility resulting in improved dispersion and less aggregation at high volume fraction. In addition, due to alignment effects, it is expected that even higher volume fractions could be attained, without aggregation, in a fibre. Furthermore, due to alignment of nanotubes in the fibre, η_0 would be increased to 1. For example, if we could retain dispersion up to 1 vol% (nanotube separation $\sim 9 \text{ nm}$) in a nanotube silk fibre we could expect moduli and strengths of $\sim 12 \text{ GPa}$ and $\sim 160 \text{ MPa}$ respectively even in the absence of protein crystallites.

In order to address the second problem we attempted to induce protein crystallisation by soaking the films in water followed by wet drawing[21]. After a short period soaking, the films curled up into a quasi-helical shape, indicative of significant internal rearrangement. This however made it very difficult to make reproducible mechanical measurements. Another technique was to clamp the film in the tensile tester while applying water via a pipette. While this method was not easily reproducible, strengths of up to 100 MPa were observed.

5.3.4 Conclusion.

We have produced nanotube-silk composites by mixing functionalised nanotubes and Biosteel in 1,1,1,3,3,3-Hexafluoro-2-propanol. Composite films were produced by drop-casting technique. The mechanical properties of the pure Biosteel films were lower than expected due to the effect of the strong denaturing solvent. Increases in stiffness, strength, ductility and toughness were observed at very low nanotube loading levels. Analysis of the

rate of increase of stiffness with volume fraction show extremely good polymer-nanotube stress transfer. However, all mechanical results saturate at a volume fraction of $\sim 0.1\%$ due to nanotube aggregation. Preliminary experiments showed that the mechanical properties of the films could be further enhanced by post-drawing in the presence of water.

	dY/dV_f , (GPa)	$d\sigma_c/dV_f$, (GPa)	dT/dV_f , MJ/m ³	$d\epsilon_b/dV_f$
Value	381 ± 105	4.65 ± 1.26	1888 ± 314	22 ± 5.4
Increase	21.5 % 1.58 GPa → 1.92 GPa	14.5 % 36.5 MPa → 41.8 MPa	87 % 1.87 MJ/m ³ → 348 MJ/m ³	45 % 0.045 % → 0.065 %
Saturation point, (V_f)	9.1×10^{-4}	9.1×10^{-4}	9.1×10^{-4}	9.1×10^{-4}

Table 5.2: Summary of the mechanical properties of Biosteel composites.

5.4 References.

1. Kronenthal, R.L., *Polymer Medecine and Surgery*, ed. P. Press. 1975, New York.
2. Zhang, D.H., et al., *Poly(L-lactide) (PLLA)/multiwalled carbon nanotube (MWCNT) composite: Characterization and biocompatibility evaluation*. Journal of Physical Chemistry B, 2006. 110(26): p. 12910-12915.
3. Tsuji, H. and Y. Ikada, *Properties and morphology of poly(L-lactide) 4. Effects of structural parameters on long-term hydrolysis of poly(L-lactide) in phosphate-buffered solution*. Polymer Degradation and Stability, 2000. 67(1): p. 179-189.
4. Drumright, R.E., P.R. Gruber, and D.E. Henton, *Poly(lactic Acid Technology)*. Advanced Materials, 2000. 12(23): p. 1841.
5. Supronowicz, P.R., et al., *Novel current-conducting composite substrates for exposing osteoblasts to alternating current stimulation*. Journal of Biomedical Materials Research, 2002. 59(3): p. 499-506.
6. Barron, V., et al., *Bioreactors for cardiovascular cell and tissue growth: A review*. Annals of Biomedical Engineering, 2003. 31(9): p. 1017-1030.
7. Niyogi, S., et al., *Chemistry of single-walled carbon nanotubes*. Accounts of Chemical Research, 2002. 35(12): p. 1105-1113.
8. Qian, D., et al., *Load transfer and deformation mechanisms in carbon nanotube-polystyrene composites*. Applied Physics Letters, 2000. 76(20): p. 2868-2870.
9. Khan, U. and J. Coleman, *Tough, super-ductile composites by addition of very low quantities of functionalised nanotubes to polyvinylchloride*. to be submitted, 2007.
10. Chen, G.X., et al., *Synthesis of poly(L-lactide)-functionalized multiwalled carbon nanotubes by ring-opening polymerization*. Macromolecular Chemistry and Physics, 2007. 208(4): p. 389-398.

11. Moon, S.I., et al., *Novel carbon nanotube/poly(L-lactic acid) nanocomposites; Their modulus, thermal stability, and electrical conductivity*. Macromolecular Symposia, 2005. 224: p. 287-295.
12. Coleman, J.N., et al., *High Performance Nanotube-Reinforced Plastics: Understanding the Mechanism of Strength Increase*. Advanced Functional Materials, 2004. 14(8): p. 791-798.
13. Coleman, J.N., et al., *Reinforcement of polymers with carbon nanotubes. The role of an ordered polymer interfacial region. Experiment and modeling*. Polymer, 2006. 47(26): p. 8556-8561.
14. Ferreira, B.M.P., C.A.C. Zavaglia, and E.A.R. Duek, *Films of PLLA/PHBV: Thermal, morphological, and mechanical characterization*. Journal of Applied Polymer Science, 2002. 86(11): p. 2898-2906.
15. Stefan, K., *High-Performance Fibers from Spider Silk*. Angewandte Chemie International Edition, 2002. 41(15): p. 2721-2723.
16. Gosline, J.M., et al., *The mechanical design of spider silks: from fibroin sequence to mechanical function*. J Exp Biol, 1999. 202(23): p. 3295-3303.
17. Lazaris, A., et al., *Spider Silk Fibers Spun from Soluble Recombinant Silk Produced in Mammalian Cells*. Science, 2002. 295(5554): p. 472-476.
18. Yu, M.F., et al., *Tensile loading of ropes of single wall carbon nanotubes and their mechanical properties*. Physical Review Letters, 2000. 84(24): p. 5552-5555.
19. Dalton, A.B., et al., *Super-tough carbon-nanotube fibres*. Nature, 2003. 423(6941): p. 703.
20. Nerie, W., et al., *Surfactant-Free Spinning of Composite Carbon Nanotube Fibers*. Macromolecular Rapid communications, 2006. 27(6042): p. 1035-1038.
21. Seidel, A., et al., *Regenerated spider silk: Processing, properties, and structure*. Macromolecules, 2000. 33(3): p. 775-780.
22. Coleman, J.N., et al., *Small but strong: A review of the mechanical properties of carbon nanotube-polymer composites*. Carbon, 2006. 44(9): p. 1624-1652.
23. Cox, H.L., *The Elasticity and Strength of Paper and Other Fibrous Materials*. British Journal of Applied Physics, 1952. 3(MAR): p. 72-79.
24. Krenchel, H., *Fibre reinforcement*. 1964, Copenhagen: Akademisk Forlag.
25. Salvetat, J.P., *Elastic and shear moduli of single-walled carbon nanotube ropes*. Phys. Rev. Lett., 1999. 82: p. 944-947.
26. Ayutsede, J., et al., *Carbon nanotube Reinforced Bombyx mori Silk Nanofibers by the Electrospinning Process*. Biomacromolecules, 2006. 7: p. 208-214.

Chapter 6: Properties of PVA Composites Produced by Electrospinning.

6.1 Introduction.

In the last two chapters, polymer-nanotube composites were prepared by drop-casting techniques using various different “biopolymer matrices”. In this chapter, Poly(vinyl alcohol) (PVA) was chosen as the biopolymer matrix to produce polymer-nanotube composites using electrospinning. The mechanical properties of electrospun PVA/CNT composites produced in two ways – firstly with a stationary plate collector and secondly with a rotating drum collector are compared. In addition, the mechanical properties of individual PVA/CNT nanofibres calculated from AFM measurements will be presented.

6.2 Background and Motivations.

PVA has received a great deal of attention because of its ability to be processed with carbon nanotubes to form composites. Previous work has demonstrated the effective mechanical reinforcement of this composite system using drop-casting techniques [1-3]. In other work, PVA/CNT fibres were fabricated by coagulation spinning showing the most outstanding toughness achieved so far [4-6]. This high performance is the result of good nanotube dispersions, effective stress transfer due to the formation of an ordered PVA coating on the nanotubes and the macroscopic orientation of the nanotubes within the polymer[7]. Recently, electrospinning was used to incorporate CNTs into a polymeric matrix to form composite nanofibres[8-12]. In this process, the nanotubes are expected to align due to the high extension and the continual narrowing of the electrospinning jet. As a consequence, effective mechanical reinforcement should be obtained. PVA is currently one of the major polymer systems being studied in the electrospinning field. For example, PVA nanofibres have been used as controlled release drug carriers [13, 14]. The formation of electrospun PVA/CNT

nanofibres prepared with both MWNTs and SWNTs has been reported [15-18], however, to our knowledge, no work has yet been presented on the production of electrospun PVA/CNT nanofibres using functionalised SWNTs. Therefore in the following chapter, we discuss the production and characterisation of electrospun PVA nanofibres reinforced with PABS functionalised nanotubes.

6.3. PVA Electrospun Film Preparations.

The PVA used in this study was purchased from Sigma Aldrich (MW 30,000-70,000g/mol). Water-soluble, PABS functionalised SWNTs (www.carbonsolution.com) were chosen to achieve high-quality nanotube dispersions in the PVA/water solutions[19, 20]. These nanotubes will be referred as P8-SWNTs in the following work. Figure 6.1 shows the synthesis of these functionalised SWNTs.

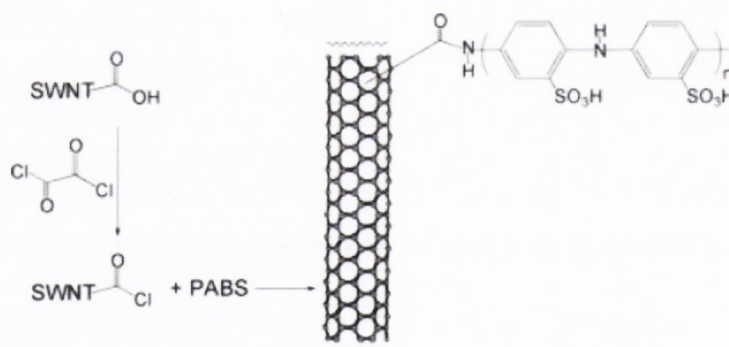


Figure 6.1: Synthesis of P8-SWNTs[19]

As explained in chapter three, the molecular weight; the solution concentration; and the solvent used; all have a significant effect on the structure of the electrospun polymer. The influence of these parameters on the morphology of electrospun PVA nanofibres has been characterised elsewhere [21, 22]. Therefore, the first step in this study was to prepare homogenous PVA nanofibres which were free of defects (no bead formation). With this in mind, we prepared PVA solutions with concentrations ranging from 150g/L up to 250g/L. In order to achieve these solutions, the PVA powder was added slowly to the solution of distilled water and crushed with a spatula in order to minimise the PVA agglomeration. The solution was subsequently placed under the sonic tip for 5 minutes to break up any remaining polymer

aggregations before placing it in a sonic bath for a further 24 hours until complete dissolution occurred. Finally, the solutions were sonicated with the sonic tip for 2 minutes immediately prior to electrospinning.

The experimental set up consisted of a 20mL syringe with a 16 gauge stainless steel needle that was positioned on a horizontally moveable structure (fig 6.2). In this preliminary work, a stationary stainless steel plate (15cm×15cm) was used as a collector. The high voltage was provided by a Brandenburg high voltage generator (0-30kV). In all cases, the needle was positively charged while the collector was grounded. Finally, a syringe pump (KDS 200 syringe pump) was used to ensure a constant flow rate and a stable Taylor cone during the electrospinning process.

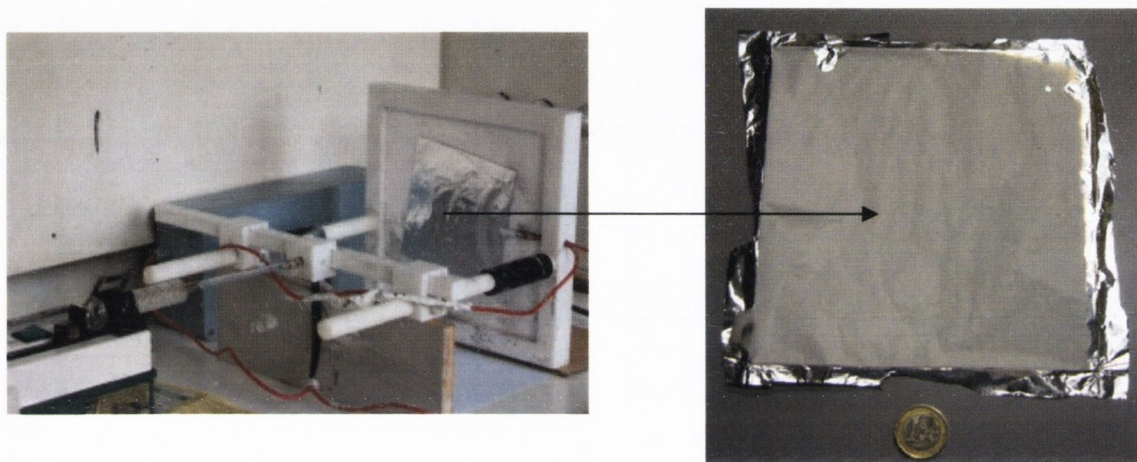
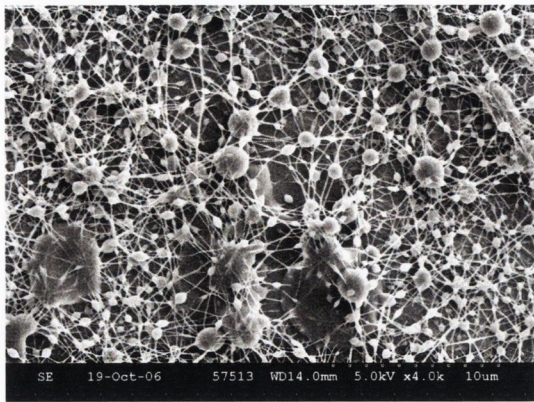
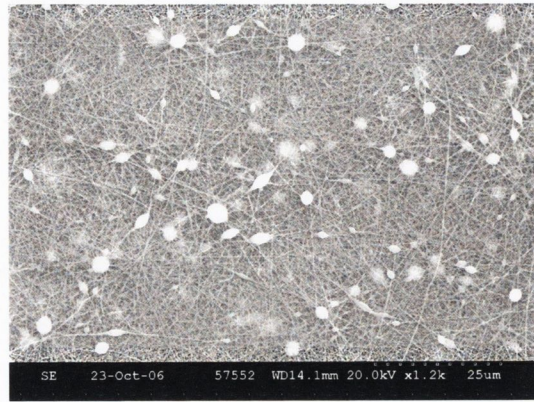


Figure 6.2: a) Electrospinning set up with a stationary plate collector, b) PVA electrospun film.

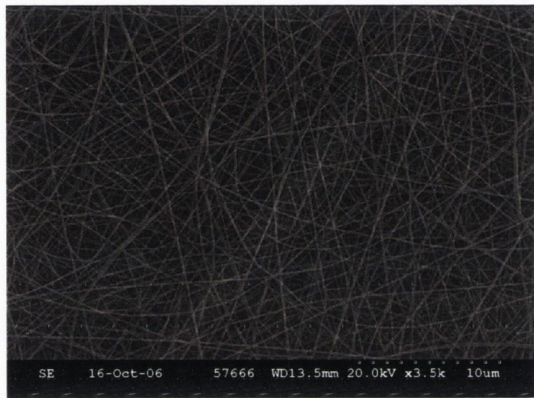
To optimise the PVA nanofibres, we investigated three needle to collector distances (10cm, 15cm and 20cm), with various voltages ranging from 10kV to 20kV. We also investigated several flow rates ranging from 0.003mL/min to 0.01mL/min. The optimum parameters for the production of homogenous nanofibres were found to be 0.003mL/min, 20cm and 20kV for the flow rate, distance and voltage respectively, using a PVA solution with a concentration of 250g/L. Figure 6.3 shows SEM images of PVA nanofibres obtained using various different parameters during this preliminary study. It should be noted that the samples were covered with a 15nm gold/palladium coating to facilitate SEM measurements.



PVA: 150g/L, 20kV, 10cm, 0.008mL/min



PVA: 200g/L, 20kV, 20cm, 0.003mL/min



PVA: 250g/L, 20kV, 20cm, 0.003mL/min

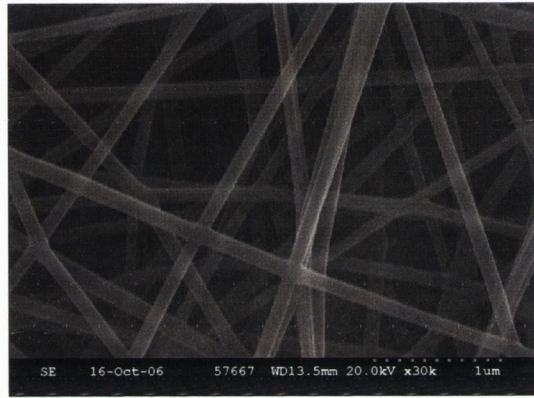


Figure 6.3: SEM images of electrospun PVA films prepared using various parameters.

Using these optimised parameters, a range of electrospun PVA/P8-SWNT composite films with nanotube volume fractions ranging from 0.05 vol% to 0.8 vol% were produced. The typical protocol for preparing PVA/CNT solutions was to disperse the desired quantity of CNTs in 20mL of distilled water using a high-power sonic tip for 5 minutes (120W, 60 kHz), followed by mild sonication in a low-power sonic bath for 3 hours. This procedure gave a good dispersion of nanotubes. Next, the required mass of PVA was added to produce a solution with a concentration of 250g/L. Subsequently, the solution was placed in a sonic bath for an extra 24 hours to obtain a good dissolution. Finally, the solutions were sonicated with the sonic tip for 2 minutes immediately prior to electrospinning.

To confirm that a good dispersion of nanotubes within the electrospun PVA/CNT membrane was achieved, Raman spectroscopy was carried out at ten different positions on each membrane. For each position in all composite membranes investigated, the G and D bands were observed at 1591cm^{-1} and 1345cm^{-1} respectively, suggesting that the nanotubes

were well dispersed within the PVA matrix. However, RBM modes were not detected in any of the composites. For comparison, Raman spectroscopy was also carried out on the electrospun PVA-only membrane. Figure 6.4 shows representative spectra recorded from these materials.

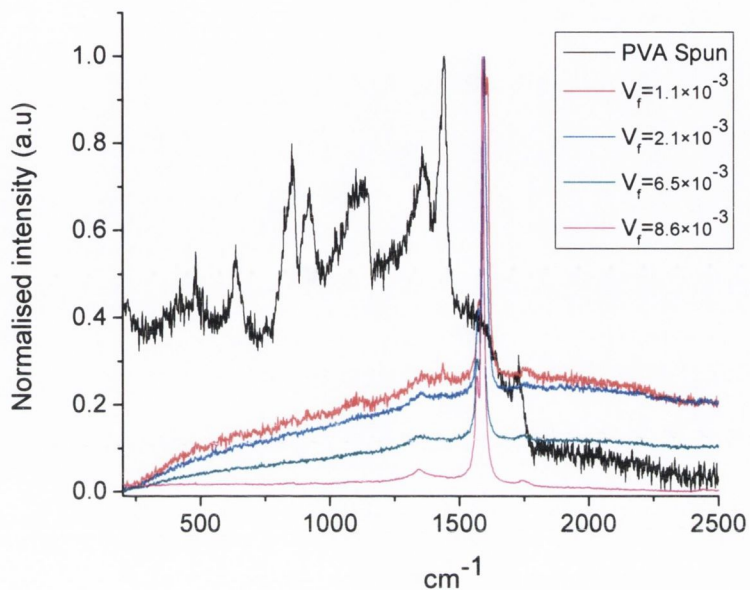


Figure 6.4: Representative Raman spectra of PVA/CNT electrospun membranes.

6.4 Mechanical Properties of PVA Electrospun Films prepared using a Stationary Plate Collector.

The mechanical properties of the electrospun PVA composite films were investigated using the Zwick tensile tester with a 100N load cell and a cross head speed of 0.5mm/min. For each composite, 10 strips were measured for statistical accuracy using a digital micrometer. The dimensions of the strips were 10mm × 2.3mm × 25μm. Figure 6.5 shows representative stress-strain curves for each composite.

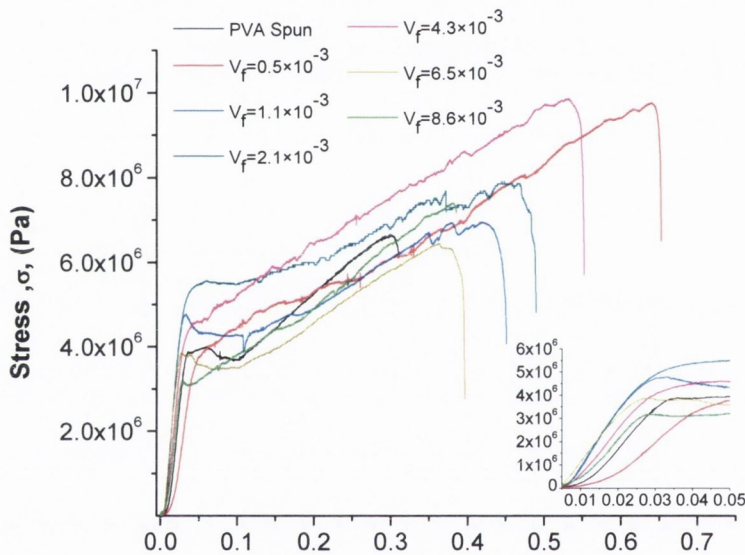


Figure 6.5: Representative stress-strain curves for PVA/CNT electrospun composites with a range of nanotube volume fractions.

As expected for thermoplastics, PVA spun films underwent elastic and plastic deformation when they were subjected to tensile stretching. The elastic deformation occurred up to 3.5% strain and then the plastic deformation took place up to a strain of 31% before breaking. Adding P8-SWNTs dramatically increased the plastic deformation as shown in Figure 6.6. The strain at break increased almost linearly up to a value of 56% strain for 0.43vol% of nanotubes. This represents an increase of 54% compared to the ϵ_b for pristine PVA electrospun films. However, above this optimum nanotube volume fraction ϵ_b was found to reduce again.

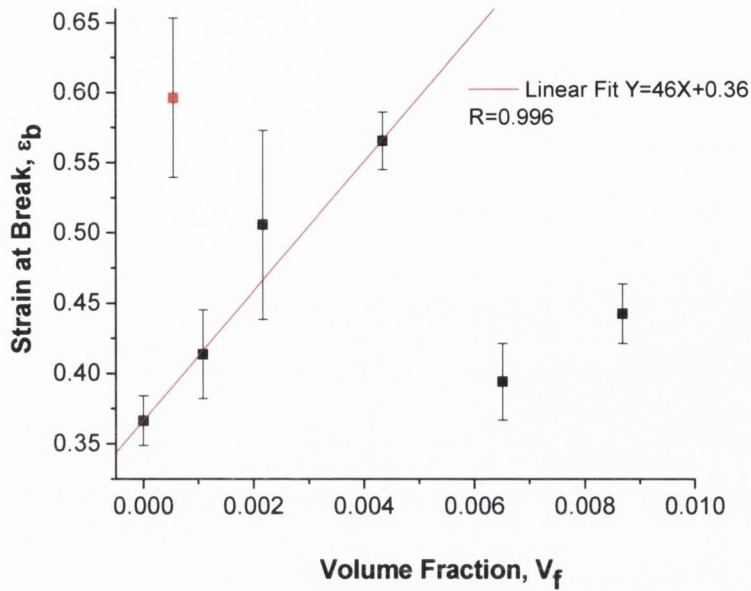


Figure 6.6: Strain at break of PVA/P8-SWNT electrospun film composites as a function of nanotube volume fraction with the corresponding standard error.

The density of each electrospun membrane was calculated by measuring the weight and dimensions of the strips using a digital micrometer and an extremely precise balance (Mettler Toledo XP26). The average density for all the films was calculated as $205 \pm 31 \text{ kg/m}^3$. It should be pointed out that this density is more than six times lower than the density of a thermoplastic polymer (1300 kg/m^3). From this result, the porosity of the membrane was calculated using the following equation:

$$P = 1 - \rho_{\text{membrane}} / \rho_{\text{polymer}} \quad \text{Equation: 6.1}$$

This gives an average porosity of $84 \pm 25\%$ for the electrospun films prepared with a stationary collector plate.

From the stress-strain curves, the Young's modulus, Y , the ultimate tensile strength, σ_c , the breaking strength σ_b , and the toughness, T , were calculated. Figure 6.7 presents these mechanical parameters with their standard errors as a function of the volume fraction of P8-SWNTs.

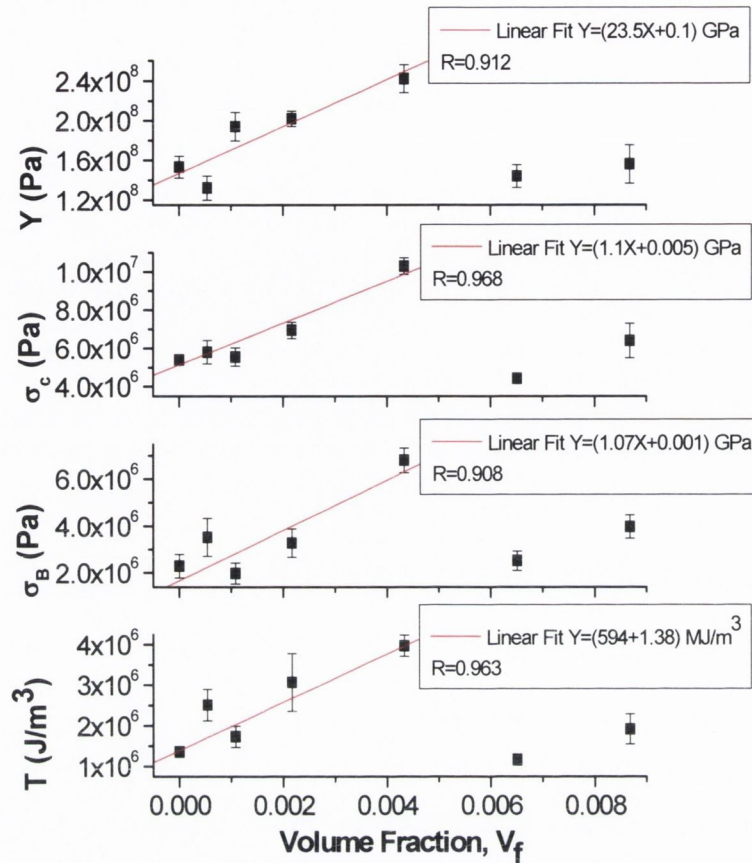


Figure 6.7: Mechanical properties of electrospun PVA films as a function of the nanotube volume fraction with the corresponding standard error.

All four parameters investigated showed a linear increase up to an optimum P8-SWNT volume fraction of 0.43vol%. Above this, all mechanical properties fell off, clearly suggesting that nanotube aggregation occurred above this concentration. Similar trends have been observed in the Y , σ_c and T parameters in the previous chapters when using PMMA[23], PLLA, and Biosteel[24] matrices. In addition, this behaviour was also observed using Poly(vinyl chloride) and chlorinated polypropylene matrices[25]. In these studies, composite films were produced by drop-casting and the optimum nanotube volume fraction was found to be less than 1vol%. Free standing film composites, prepared using PVA with catalytic thin MWNTs, also demonstrated a linear increase in Y , σ_c and T up to 0.6vol% of nanotubes[3]. Our electrospun composite membranes showed an increase in the Young's modulus of 58%, increasing from 0.15GPa to 0.24GPa. This gives a dY/dV_f of 23.5 ± 3.6 GPa. Previous work on electrospun PVA/MWNT composites has been reported, showing an increase of 5% in the Young's modulus (0.175GPa to 0.184GPa) upon the addition of

0.15vol% nanotubes[18]. This corresponds to an enhancement in the Young's modulus of 0.6GPa. The difference in these results could be due to the PVA concentration used in their study (9wt%). They may have exceeded the critical aggregation concentration of nanotubes, resulting in a poor dispersion of the filler. Dispersion issues are even more critical in the electrospinning process since a high concentration of polymer is required. Ko et al were the first group to investigate CNTs as a filler to improve the mechanical properties of electrospun polymer membranes[9]. Using polyacrylonitrile (PAN), they reported an increase of 133% by adding 4wt% of SWNTs. Sen et al demonstrated a dramatic improvement in the stiffness of elastomer polyurethane spun membranes, with increases of 215% (7MPa to 22MPa) and 250% (7MPa to 24.5MPa) upon the addition of 0.87vol% of as-prepared and ester functionalised SWNTs respectively [26]. This corresponds to an enhancement in the Young's modulus of 1.7GPa and 2GPa for as-prepared and ester functionalised SWNTs respectively. This result emphasises the importance of using functionalised nanotubes to improve the dispersion, and the mechanical properties, of the composites. Huang et al also used electrospinning to produce polyurethane composites [27]. In this work, they used carbon black as a filler and employed a rotating drum as the collector. By adding 9.4 vol% of carbon black, their polyurethane composites displayed an increase of more than 400% in the Young's modulus, increasing from 0.74MPa to 3.75MPa.

The ultimate tensile strength of our electrospun membranes shows an increase of 91% from 5.39MPa to 10.3MPa, giving a $d\sigma_c/dV_f$ of 1.09 ± 0.11 GPa. Jeong et al reported an increase of 60% (from 5.8MPa to 9.3MPa) by adding 0.6vol% of MWNTs to electrospun PVA membrane[18]. This corresponds to a $d\sigma_c/dV_f$ of 0.58GPa. Similarly, Sen et al reported increases in the tensile strength of 46% (7.02MPa to 10.26MPa) and 104% (7.02MPa to 14.3MPa) by adding 0.87 vol% of as-prepared and ester-functionalised SWNTs respectively[26]. The breaking strength, σ_B , increased by more than 197% from 2.29MPa to 6.81MPa, giving a $d\sigma_B/dV_f$ of 1.07 ± 0.15 GPa. Unfortunately, no information was available to our knowledge to compare with our data for similar systems.

The last parameter to be investigated was the toughness, which increased by more than 191% from 1.36 to 3.97MJ/m³. This gives a dT/dV_f of 594 ± 156 MJ/m³. The densities of the strips used in this study were measured using a high precision microbalance and a digital micrometer. The density of the PVA electrospun membrane, prepared with 0.43 vol% P8-SWNTs, was calculated to be ~ 255 kg/m³, giving a toughness of ~ 15.6 J/g. This is a remarkable result since the toughness of Kevlar® is only ~ 33 J/g at low strain.

6.5 Mechanical Properties of PVA Electrospun Films using a Rotating Drum Collector.

Mechanical studies on electrospun films prepared with a stationary plate collector have shown that the optimum reinforcement of PVA electrospun membranes was achieved using a volume fraction of P8-SWNTs 0.43 vol%. Therefore, this concentration was used to produce aligned electrospun PVA/CNT nanofibre membranes. Aligning the nanofibres should increase the mechanical properties of the membrane in one preferential direction. In other words, the mechanical properties are no longer isotropic, but anisotropic in two directions (parallel and perpendicular to the direction of the drum rotation). Increasing the rotation speed should increase the anisotropy. Figure 6.8 shows the apparatus used to produce these aligned composites. This set up allows the production of membrane 10cm wide and 30cm long. In order to compare these membranes with those produced using the plate collector, we prepared a solution of PVA (250g/L) with 0.43vol% of P8-SWNTs using the same protocol. In addition, the same electrospinning parameters were used, i.e. a 20 cm needle-collector distance, a voltage of 20kV and a flow rate of 0.003mL/min.

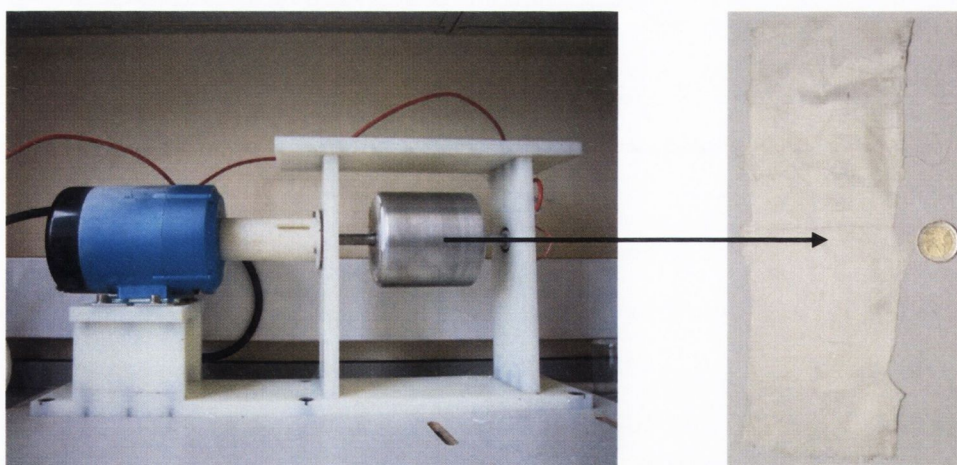
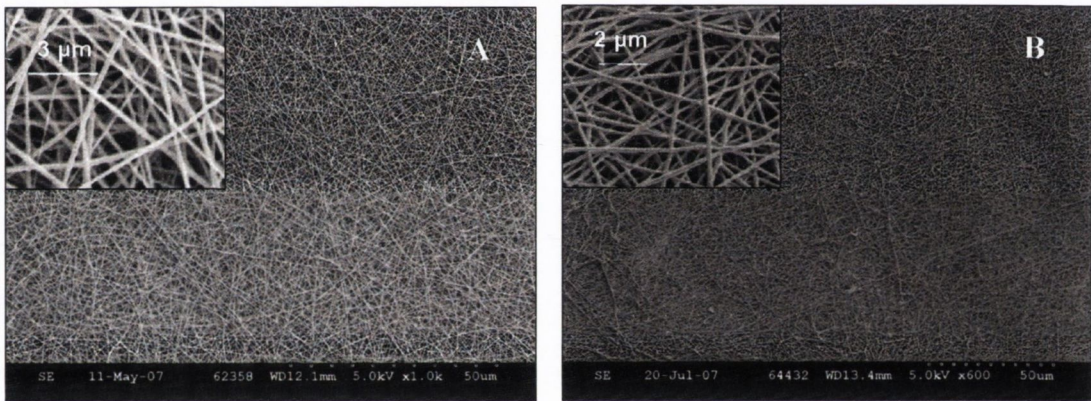


Figure 6.8: Electrospinning apparatus using a rotation drum collector.

Various rotation speeds were used to produce the aligned membrane composites (1818rpm, 1176rpm, 566rpm and 200rpm). The drum rotation speed was calibrated using a laser, a photodiode and an oscilloscope. In order to perform this measurement, the drum was first covered with black cello-tape. Subsequently, a mirror (1 cm × 1 cm) was attached on the drum. Light from a continuous wave Helium-Neon laser (wavelength 632.8 nm) was then used to

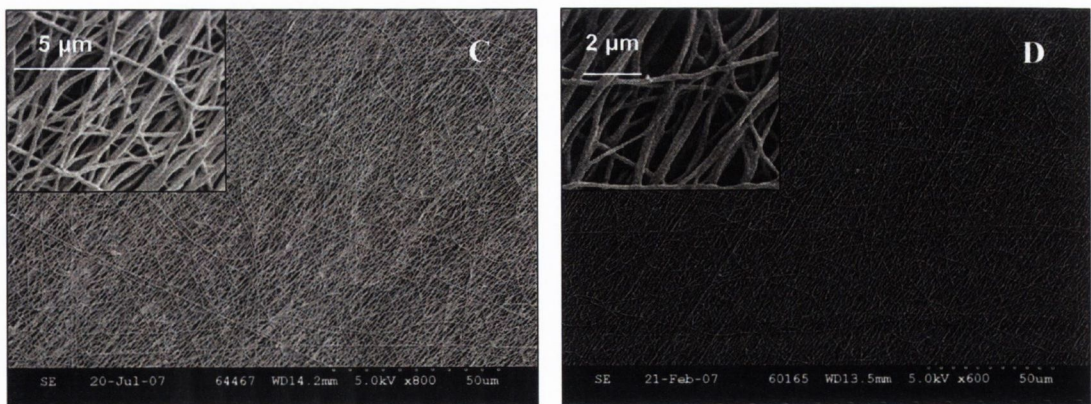
illuminate the mirror at a 45 degrees angle. The reflected beam was collected with a photodiode, which was connected to an oscilloscope. A peak appeared on the oscilloscope for each full rotation of the drum. The period between two successive peaks then gave the effective rotation frequency, which in turn was converted into the angular frequency and the rotation per minute of the drum. It should be pointed out that 1818rpm is the maximum rotation speed allowed by this set up. In order to minimise errors, the same solution was used at each speed.

Morphological characterisation was carried out using scanning electron microscopy (SEM) in order to confirm that increasing the rotation speed increased the alignment of the nanofibres. Figure 6.9 shows SEM images of PVA/P8-SWNT electrospun films for various rotation speeds and cross sections of the films at the higher speed rotation. A previously, all samples investigated by SEM were first coating with gold (15 nm).

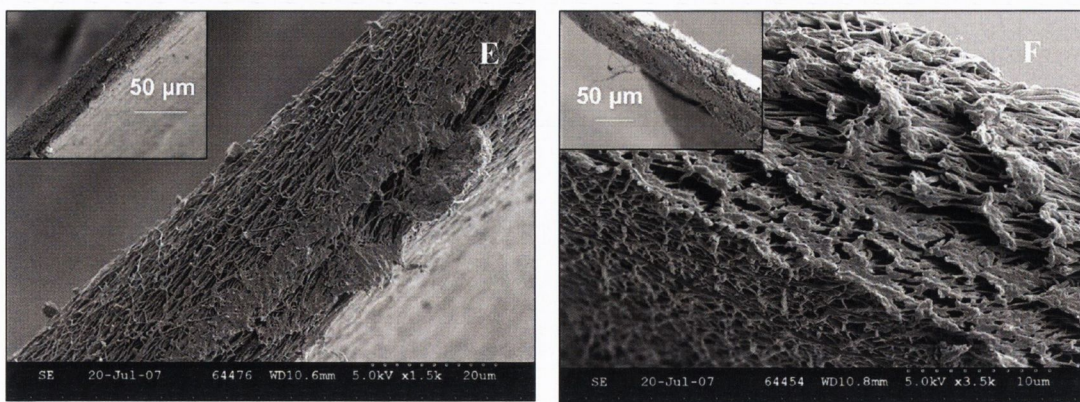


Surface of PVA composites with 0.5wt% of P8-SWNTs

A) Membrane spun onto a stationary plate. B) Membrane spun onto a drum rotating at 200 rpm



Surface of PVA composites with 0.5wt% of P8-SWNTs membrane spun onto a drum rotating C) at 1176 rpm D) at 1818 rpm



Cross sections of an aligned composite membrane (1818 rpm, 0.5wt%) produced by cutting the membrane E) parallel and F) perpendicular to the alignment direction.

Figure 6.9: SEM pictures of PVA/P8-SWNTs electrospun films for various speed rotation and cross sections of the films at the higher speed rotation.

SEM images A, B, C and D clearly show an increase in the nanofibre alignment as the speed is increased up to the maximum of 1818 rpm. The nanofibre morphology also changes slightly, from a cylindrical structure to a flatter structure, because of the stretching caused by the increase in the rotation speed. Pictures E and F show two cross sections of the highest speed nanofibre membrane, cut parallel and perpendicular to the direction of the drum rotation. These pictures clearly show a preferential alignment of the nanofibres in the direction of the drum rotation.

However, it is difficult to assess the degree of fibre alignment at high rotation speeds. To overcome this problem we used Fast Fourier Transform (FFT) on the SEM images to evaluate the alignment of the nanofibres as a function of the rotation speed. These measurements were carried out using the software ImageJ. For each rotation speed, FFT analysis was performed on three SEM images for statistical accuracy. This analysis was also performed on SEM images of electrospun membranes prepared with the collector plate. The FFT images obtained were subsequently treated by an “ovale profile” giving spectra of Gray value versus degrees (Fig 6.10). For each spectrum, the full width at half maximum (FWHM) was measured and plotted against the corresponding rotation speed. A lower FWHM corresponds to a greater alignment of the nanofibres.

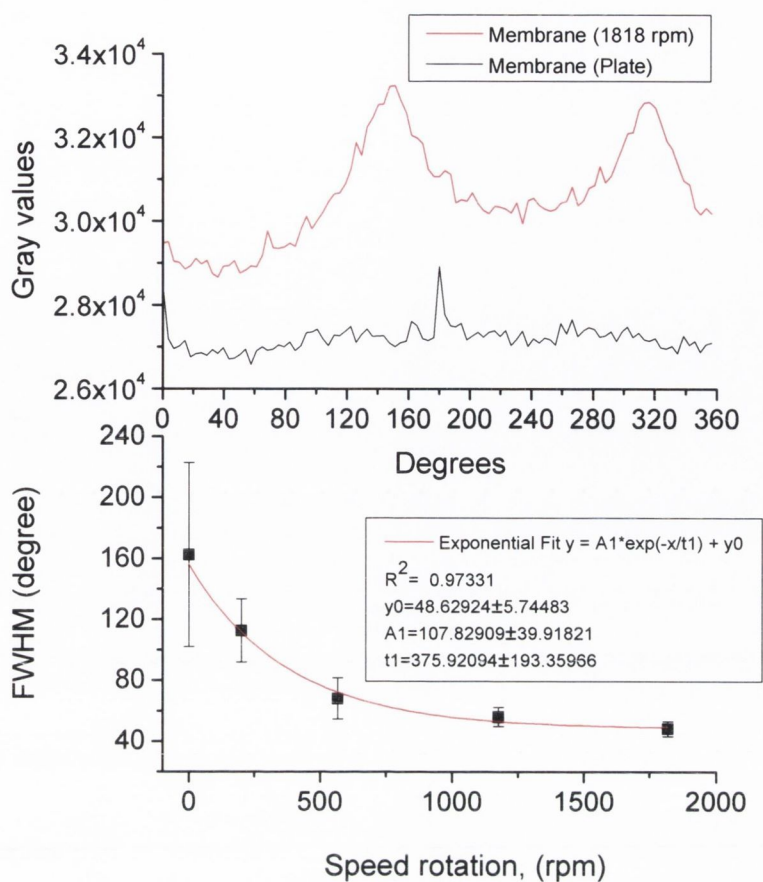


Figure 6.10: FWHM plotted as a function of the rotation speed.

From Figure 6.10, it can be observed that the FWHM follows an exponential decay, converging on a value of 48 ± 6 degrees. This proves that the effective alignment of the fibres increases with rotation speed.

Mechanical measurements on the electrospun PVA composite membranes were also performed with a Zwick tensile tester. Measurements were carried out under the same conditions used in stationary plate collector study. For each rotation speed, 10 strips, both perpendicular and parallel to the direction of the drum rotation, were cut from the membrane. The dimensions of the strips were $10\text{mm} \times 2.3\text{mm} \times 25\mu\text{m}$. For comparison, a drop-cast film was produced from the same solution and tested. This allows a comparison of the mechanical properties of bulk composites and electrospun membranes. Figure 6.11 shows representative stress-stain curves obtained from these tensile measurements.

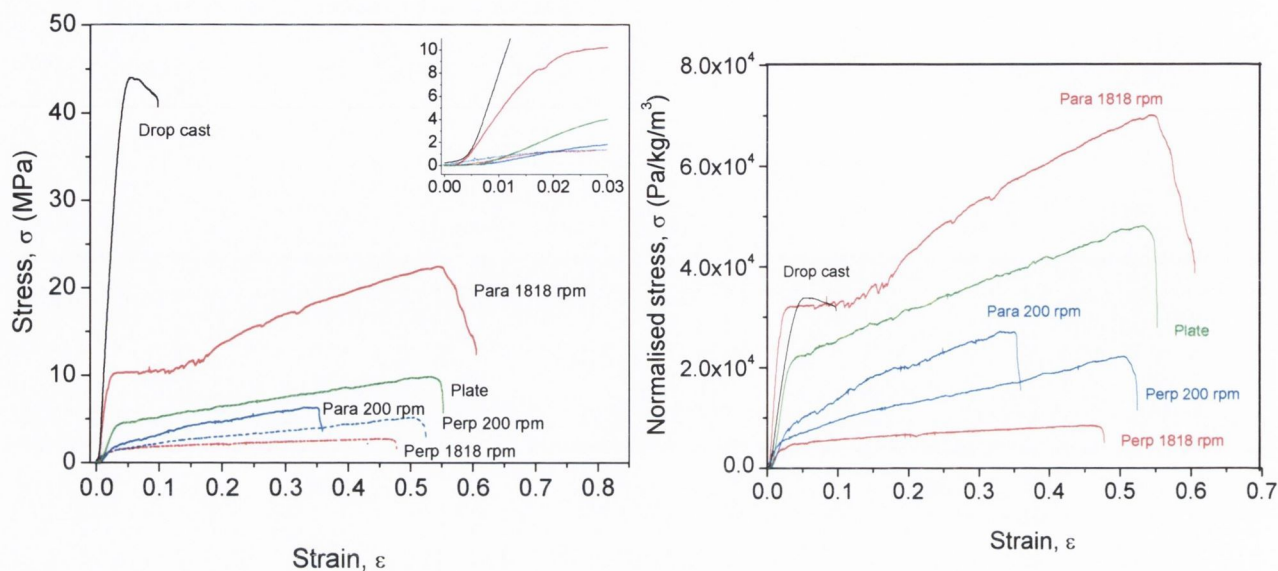


Figure 6.11: Representative stress-strain curves of PVA/P8-SWNTs bulk and electrospun composites.

The bulk and electrospun composites presented dramatic differences when subjected to tensile stretching. Films produced by the drop-casting technique display brittle behaviour with a large elastic deformation up to 5% strain. This is expected as the PVA concentration is relatively high (250g/L). The bulk composites then experienced a small plastic deformation before fracture at ~10% strain. By comparison, the electrospun composites showed a ductile behaviour when stretched. It was found that the strips cut parallel to the drum rotation axis from the 1818rpm membrane (Para 1818rpm) showed stiffer, stronger behaviour than those cut from the membrane prepared with the stationary plate collector. In addition, they also undergo larger plastic deformation (60% strain) than the strips produced with the plate collector (55% strain). In contrast, the strips cut perpendicularly to the drum rotation axis from the 1818rpm membrane (Perp 1818) exhibited lower stiffness, strength and plastic deformation (47% strain) than the “Plate” strips. This is expected since the perpendicular strips are less entangled than the plate strips and the nanofibres are mainly held together by Van der Waals interactions. Consequently, less force is required to stretch and break these strips. Figure 6.12 shows the mechanical parameters (Y , σ_c , ϵ_B , T) with the associated standard error, calculated from the stress-strain measurements for both drop-cast and electrospun composites.

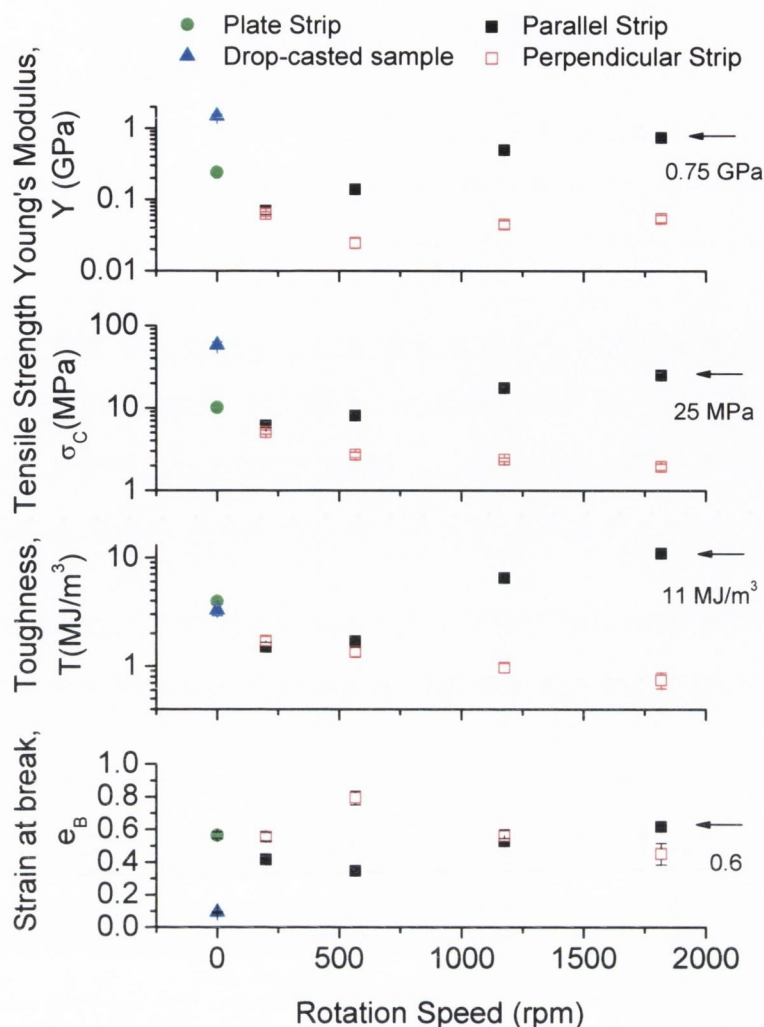


Figure 6.12: Mechanical parameters for drop-cast and electrospun composites with the corresponding standard error.

The perpendicular-film properties are relatively low and do not vary significantly with rotation speed. However, for the lowest speed (200rpm) the mechanical properties approach the values obtained from the membrane formed with the plate collector. All parallel-film properties increased with increasing rotation speed. At the highest speed, the parallel films possessed higher mechanical properties for all parameters investigated than the films prepared with the plate collector. A Young's modulus of $0.74 \pm 0.05 \text{ GPa}$ was observed, which is three times greater than that of the "Plate" films ($0.24 \pm 0.01 \text{ GPa}$). It should be noted that this is only two times smaller than the Young's modulus obtained for drop-cast films ($1.51 \pm 0.08 \text{ GPa}$). Similarly, the tensile strength, σ_c , is ~ 2.5 times greater for the "parallel" strips than for the "plate" strips, with values of $25.1 \pm 1.9 \text{ MPa}$ and $10.3 \pm 0.4 \text{ MPa}$ respectively. For the drop-cast

films, σ_C is only $\sim 50\%$ higher ($58.7 \pm 5.7 \text{ MPa}$). The strain at break increased by just 10% when comparing parallel strips to the plate strips. However, the most impressive result is the toughness, which increased by more than 177% when drum collector is used at the highest speed rather than the collector plate (11 MJ/m^3 and 3.9 MJ/m^3 respectively). The toughness is even more impressive when compared with the drop-cast films, where an increase of 231% was observed ($T_{\text{drop-cast}} = \sim 3.32 \text{ MJ/m}^3$). Using the calculated density of the 1818 rpm electrospun composite films ($\sim 320 \text{ kg/m}^3$), one can calculate the toughness to be 34 J/g . This is a remarkable result since this value matches the toughness of Kevlar.

As for the previous study using the collector plate, the density was measured for each electrospun film prepared with the rotating drum. Figure 6.13 shows the density for each rotation speed.

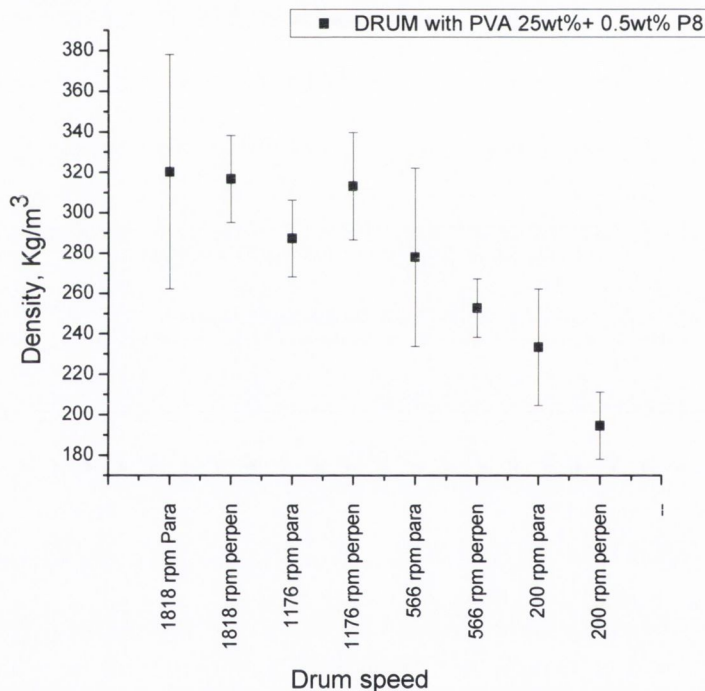


Figure 6.13: The density of the electrospun films as a function of the rotation speed of the drum.

At the maximum speed, the density is $\sim 320 \text{ kg/m}^3$. The density then decreases down to a value of $\sim 200 \text{ kg/m}^3$ for the lowest speed. Electrospun membranes prepared with the plate collector possess similar densities ($\sim 205 \text{ kg/m}^3$). This suggests that below a minimum rotation speed, the rotating drum collector has a minimum impact on the morphology and organisation of the nanofibres in this polymeric system.

6.5 Mechanical Properties of PVA Composite Electrospun Nanofibres.

The mechanical properties of electrospun membranes have been investigated using the tensile tester. For completeness, measurements were also performed on single nanofibre composite using an AFM tip as described in Chapter Three. To perform these measurements, PVA/CNT solutions were prepared at the same concentration (250g/L), with the same range of P8-SWNT volume fractions as for the solutions used in the first study (0.054vol% to 0.8 vol%). SiO₂ substrates, which were pre-patterned with trenches, were then set onto the stationary plate collector and the solutions were electrospun for a very short time (~45seconds) using the same electrospinning parameters employed in the two previous studies (20kV, 20cm, 0.003mL/min). An electronic microscope was used to screen both the amount and the position of single nanofibres over the trenches. This is a crucial step since the nanofibres have to be deposited perpendicularly over trenches and in small quantities in order to allow mechanical measurements with AFM tips. If these criteria were not achieved, the nanofibres were carefully washed away from the substrate and the process repeated until optimum deposition was accomplished.

AFM mechanical measurements were carried out on 15 single nanofibres from each electrospun solution. From these measurements, two main sets of information were required to calculate the Young's modulus, the ultimate tensile strength, the toughness and the strain at break. Firstly, the diameter of the nanofibre was measured, as shown in figure 6.14 by using the AFM apparatus.

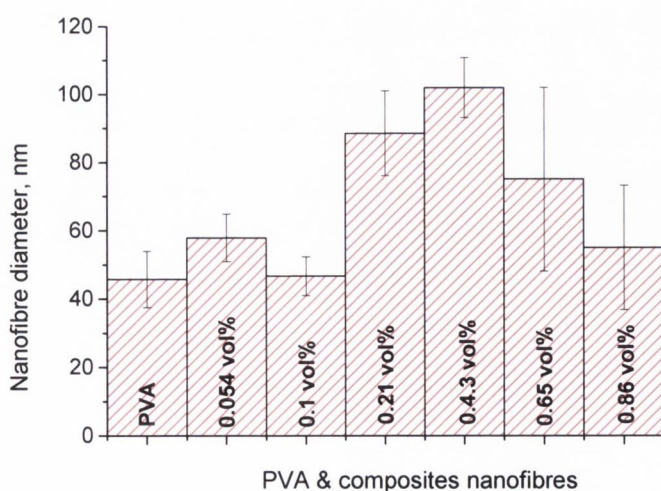


Figure 6.14: Average diameters of PVA and composites electrospun composite.

Secondly, the force displacement curves were recorded, as seen in Figure 6.15.

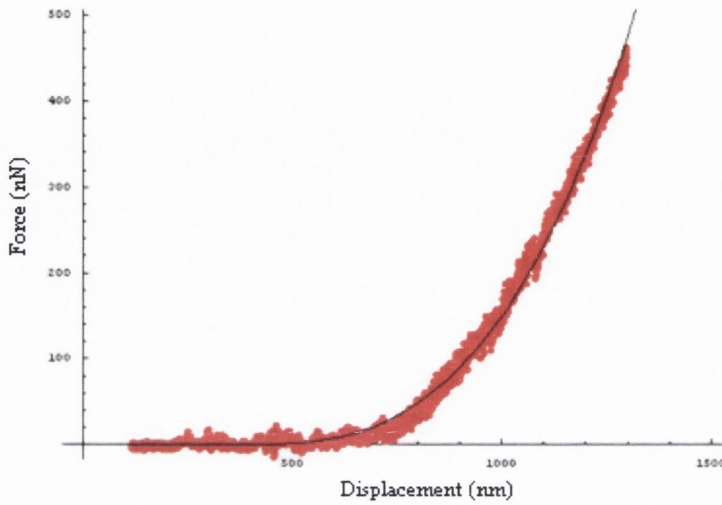


Figure 6.15: Force-displacement curve for a single nanofibre of PVA composite.

For all individual fibre measured, the force, F_m , and the displacement, d , were used to calculate the tensile strength and the strain at break based on the model as shown in Figure 6.16.

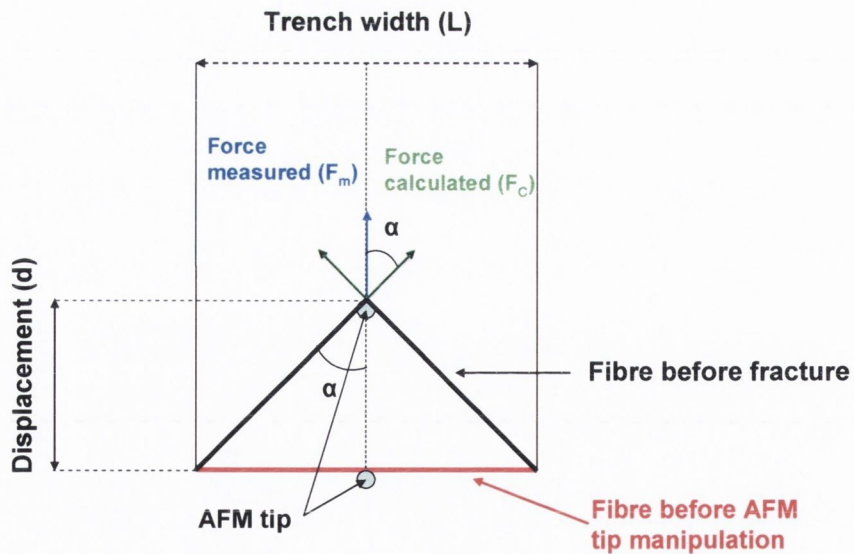


Figure 6.16: Schematic of model used to calculate the mechanical properties of a single electrospun nanofibre.

The first step was to calculate the axial force, F_a , of the fibre before failure. This value is given by the following equation:

$$F_a = \frac{F_m}{2} \sqrt{\left(1 + \frac{L^2}{d^2 4}\right)} \quad \text{Equation 6.1}$$

Then the ultimate tensile strength was calculated by taking $\sigma_c = F_a/A$, where A , the cross sectional area, was calculated from the diameter of each nanofibre. It should be point out that the value obtained for ultimate tensile strength is equal to the value of the breaking strength, since we assume a brittle behaviour with no plastic deformation for all nanofibres investigated. The strain at break was calculated using the following equation which is also based on the model presented in Figure 6.12.

$$\varepsilon_B = \sqrt{\left(1 + \frac{4d^2}{L^2}\right)} - 1 \quad \text{Equation 6.2}$$

Afterwards, the Young's modulus was calculated, assuming that a linear elastic deformation with no plastic deformation occurred giving $Y = \sigma_c/\varepsilon_B$. Finally, the toughness was calculated using the following equation with the assumption of a linear stress strain curve.

$$T = \frac{1}{2} \times \frac{\sigma_c^2}{Y} \quad \text{Equation 6.3}$$

The calculated mechanical parameters from the above equations are presented in Figure 6.17 with their associated standard error. It should be pointed out that for each volume fraction displayed; the two highest and lowest values were disregarded because of error suppression.

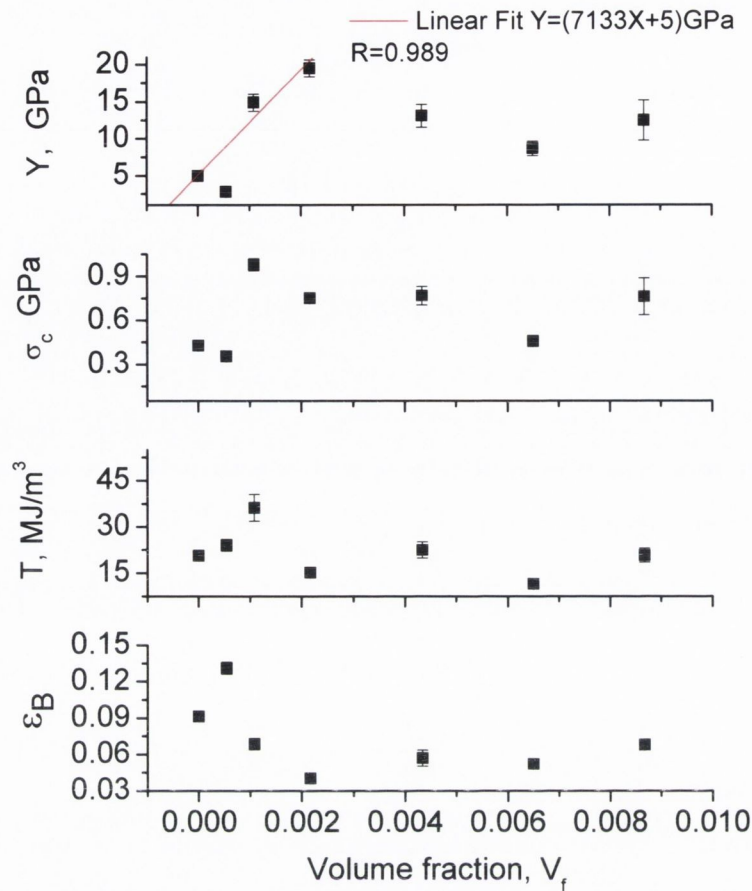


Figure 6.17: Mechanical parameters for single electrospun nanofibres with the corresponding standard error.

All the mechanical properties investigated were found to increase with the addition of CNTs. However, optimum reinforcement was not observed for the same nanotube volume fraction as seen previously for the study on electrospun membranes using the plate collector (0.43vol%). This can be attributed to a variation in the diameters of the nanofibres as show in Figure 6.11. Therefore, the alignment of the nanotubes may vary from one nanofibre to another, giving rise to variations in the mechanical properties as observed in Figure 6.13. The Young's modulus shows a dramatic linear increase from 4.9 to 19.5GPa (293%) upon the addition of less than 0.2vol% of nanotube. This corresponds to a dY/dV_f of $7133 \pm 522 \text{ GPa}$. The elastic modulus for electrospun Poly(acrylonitrile) (PAN) with a range of SWNT mass fractions was measured by Ko et al using AFM in a compression load deformation test[9]. By adding 2.8vol% of SWNTs, the elastic modulus increased by 133%, giving a dY/dV_f of 2.9TPa. More recently, Liu et al used AFM to carry out tensile measurements on single PMMA electrospun fibres[28]. To perform these tests, a PMMA nanofibre was glued at both ends to an AFM tip and a drop of epoxy glue. Once dry, the nanofibre was stretched until

failure. Using this technique, the mechanical properties of functionalised MWNT/PMMA nanofibres were also measured. By adding, 2.7vol% of functionalised MWNTs, the Young's modulus improved by 266%, from 72.8MPa to 267MPa, giving a dY/dV_f of 6.3GPa. These results are 100 times lower than our results. However, their experimental composite modulus agreed with the calculated composite modulus using Halpin-Tsai equation (288GPa). This difference could be explained by the crystalline phase presented in PVA which could induce a strong stress transfer between the polymer and the nanotubes. Kannan et al studied the mechanical properties of PVA/SWNT electrospun nanofibres using Raman spectroscopy[17]. They demonstrated a good stress transfer between the PVA matrix and the nanotubes, with a calculated Young's modulus for the SWNTs of 800GPa. This is a remarkable result since the maximum possible nanotube modulus is ~ 1 TPa.

The ultimate tensile strength, which in this case can be assimilated to the breaking strength, also showed an increase of more than 129%, from 0.42GPa to 0.97GPa, by the addition of 0.1vol% of nanotubes. These are very high strength values for thermoplastic polymers. For poly vinyl polymers, strength are generally accepted to be in a range of 40 to 50MPa[29]. Liu et al reported an increase of 157%, from 30.9MPa to 79.5MPa, in the tensile strength of their electrospun PMMA fibres by adding 2.7vol% of MWNTs [30]. However, Wang et al also demonstrated high strengths of up to 1.71 GPa for PVA bundle fibres[31].

The toughness displayed a linear increase from 20.6 to 36.2MJ/m³ by adding 0.1vol% of nanotubes This represents an increase of 75 %, with a dT/dV_f of 14.5GJ/m³. Taking a density of 1300 kg/m³, the toughness for the optimum vol% is ~ 28 J/g. Once again, this is almost as tough as Kevlar.

The strain at break shows a small increase of 43% by adding 0.5vol% of nanotubes. However above this nanotube concentration, the strain at break is lower than that of electrospun PVA fibres.

In order to understand the high values obtained for dY/dV_f from our AFM results, DSC measurements were carried out on the PVA/CNT electrospun membranes. The following program was used to carry out DSC measurements:

- Two heating scans from 0°C to 210°C at 10°C/min
- One cooling scan from 210°C to 0°C at 100°C/min

Figure 6.16 shows representative DSC heat scans for both electrospun and drop cast films, each with a 0.43vol% of P8-SWNTs. For every nanotube volume fraction, both PVA/CNT electrospun and drop cast film composites were prepared from the same solution, allowing a direct comparison of the thermal properties. In addition, it should be pointed out that we chose to represent only a set of electrospun and drop cast films composites in this figure because others composites films display similar features in their thermal scans. Figure 6.18 also displays the crystallinity, χ , as a function of the nanotube volume fraction for the electrospun films produced with a plate collector. χ was calculated from the first heat scan using equation 3.3 and taking $\Delta H_{100\%}$ for PVA to be 138.6 J/g [32].

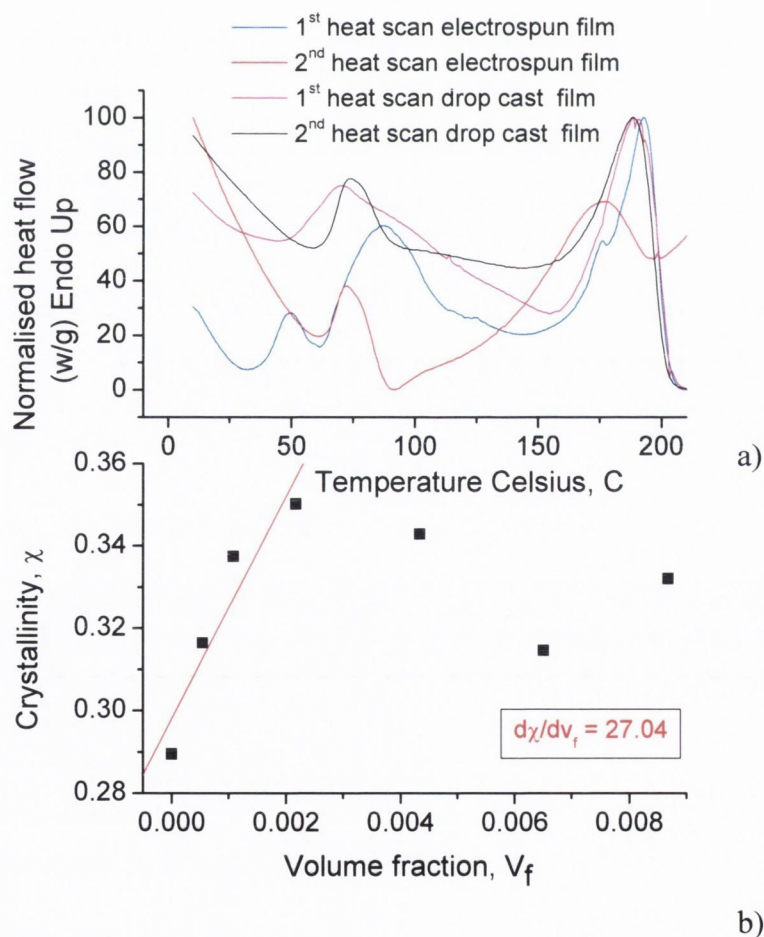


Figure 6.18: a) 1st and 2nd heat scan of PVA electrospun and drop cast film composites with 0.43 vol% of P8-SWNTs, b) Crystallinity, χ , as a function of the volume fraction of carbon nanotubes of electrospun composites films.

From the first heat scan, the glass transition temperature, T_g , was found to be $\sim 43^\circ\text{C}$ and $\sim 58^\circ\text{C}$ for the electrospun and the drop cast films respectively (Figure 6.18 (a)). This value is a much lower than expected for this polymer grade ($\sim 70^\circ\text{C}$) [33]. For the electrospun composite, this dramatic decrease in the T_g can be attributed to the electrospinning process, which leads to less entangled polymer chains. Consequently, less energy is required to reach the glass transition. All electrospun membranes display similar T_g values for the first heat scan. The small decrease of 10°C is observed in the drop cast composite, which can be attributed to the presence of trapped water in the film which acts as a spacer between polymer chains. For the electrospun film, a large endothermic peak is observed after the glass transition around 90°C . This peak is the result of water evaporation. Indeed PVA is known to have a strong affinity for water and the electrospun membrane is highly porous. This effect is highlighted by the very small endothermic peak observed in the drop cast film at 100°C . This also underlines the large surface area achieved when producing electrospun membranes. The second endothermic peak ($\sim 190^\circ\text{C}$), observed in both electrospun and drop cast film composites, corresponds to the melting temperature (T_m) of PVA. This is the expected value for this polymer ($180\text{--}190^\circ\text{C}$) [34]. After a cooling run, a 2nd heating scan was carried out, showing very different characteristics to the 1st scan. Firstly, for both film types, the glass transition temperature increased to $\sim 70^\circ\text{C}$. This shift can be explained by both a morphological change from a porous to a bulk structure and the absence of water in the PVA matrix after the first heat. Indeed, no endothermic water peaks are observed during this heating scan. Finally, the melting peak of the electrospun film was found to shift to 175°C . The reasons for decrease in T_m are still unclear. Comparing the percentage crystallinity in the first heating scans for both the electrospun film and the drop cast film provides more useful information. χ values of 34% and 24% were obtained for the electrospun film and the drop cast film respectively. The variation in these values can be explained by the electrospinning process. It is thought that the electrostatic field causes the polymer molecules to become more ordered during electrospinning, thus inducing a greater crystallinity in the fibres. This effect has also been observed by Zhao et al for electrospun Ethyl-Cyanoethyl Cellulose nanofibres [35].

From Figure 6.18 (b), the percentage crystallinity of electrospun composites increases linearly from 29% to 35% by adding less than 0.2 vol% of P8-SWNTs. This corresponds to an

augmentation of ~21%. This is an interesting result since this linear increase almost matches the linear increase observed in the Young's modulus for PVA/CNT electrospun membranes prepared with the stationary plate collector. However, Coleman et al recorded a linear increase of ~240% for drop-cast PVA/MWNT films[3]. The variation between these values can be explained by our choice of functionalised SWNTs in this study, which may reduce the ability of the PVA to coat the nanotubes. In addition, the induced alignment of the polymer chains from the electrospinning may inhibit the degree of PVA wrapping around the nanotubes. In another study, Coleman et al developed a model to quantify the effect of this induced ordered phase of the PVA on the Young's modulus of the composite[7]. This model was based on the rule of mixtures, taking into account three phases: the nanotube phase, the amorphous PVA phase and the induced ordered PVA phase. The enhancement in the Young's modulus differentiated from this model is expressed as follows:

$$\frac{dY}{dV_f} = (Y_x - Y_a) \frac{d\chi}{dV_f} + (\eta_0 Y_{eff} - Y_a) \quad \text{Equation 6.4}$$

where Y_x and Y_{eff} are the effective Young's moduli of the crystalline polymer phase and the nanotubes respectively. Y_a is the Young's modulus of the amorphous phase and η_0 is related to the orientation of the nanotubes as described in chapters 4 and 5. In this case, $\eta_0 = 1$, since the nanotubes are assumed to be aligned by the electrospinning. Taking Y_x to be 46 GPa[7] and Y_a to be 4.9 GPa, Y_{eff} was calculated to be ~6TPa. This value is much higher than the expected value of 1TPa. This strongly suggests that another mechanism must occur between the nanotubes and the PVA matrix during the electrospinning process. Also, Y_x may be higher for these fibres because maybe crystals are more ordered and stiffer in this case.

6.6 Conclusion.

To conclude, we successfully prepared homogenous electrospun PVA nanofibres from a PVA-water solution at a concentration of 250g/L. The electrospinning parameters were investigated showing the optimum values to be 20kV, 20cm and 0.003mL/min for the voltage, distance and flow rate respectively. In addition, electrospun PVA membranes were produced with a range of P8-SWNT volume fractions using a stationary plate collector. Raman

spectroscopy was carried out, demonstrating that a good dispersion of nanotubes within the electrospun films was achieved. Mechanical measurements revealed a linear increase in all mechanical properties investigated (Y , σ_C , σ_B , ϵ_B and T) as the nanotube volume fraction was increased, up to a maximum value of 0.43vol%. Above this concentration, all mechanical properties fell off, suggesting nanotube aggregation. The average density and porosity of the membranes was calculated to be 205kg/m^3 and 84% respectively. Using the optimum loading level of nanotubes, electrospun composite membranes displayed a toughness of 15.6J/g. By comparison, Kevlar has a toughness of 33J/g. DSC analysis showed a linear increase in the crystallinity for nanotube volume fractions of up to 0.2vol%. DSC also showed an increase in the crystallinity of the polymeric system as a result of the electrospinning technique.

Based on these results, electrospun PVA membranes with 0.43vol% of nanotubes were also produced with various rotation speeds using a rotating drum collector. Using this set up, we demonstrated the effective alignment of the nanofibres as a result of increasing the rotation speed by Fast Fourier Transform analysis. Electrospun composite membranes prepared at the highest rotation speed displayed a Young's modulus and strength values similar to those observed for drop cast composites, but with densities that were 5 times lower. More importantly, this electrospun membrane demonstrated a toughness that was almost equivalent to that of Kevlar (34 J/g).

Finally, mechanical measurements were carried out with an AFM on PVA nanofibres with various volume fractions of P8-SWNTs. These nanofibres displayed very brittle behaviour with no plastic deformation. The Young's modulus, the tensile strength, the strain at break and the toughness were calculated from the force displacement curves using a simple mathematical model. Very high strength values of up to 0.9GPa were obtained for these nanofibres. Extremely high values for the enhancement Young's modulus has also been obtained (7 TPa). This result could not be explained using the double rule of mixtures, suggesting another mechanism taking place.

All the main mechanical results investigated are presented in the table below.

	Membranes from plate collector	Membrane from drum collector	Single nanofibres from AFM measurements
Young's Modulus GPa	$dY/dV_f=23.5\pm 3.6$ 58% increase from 0.15 to 0.24 $V_f=4.3\times 10^{-3}$	0.75 (drop cast film~1.59) 1818rpm $V_f=4.3\times 10^{-3}$	293 % increase from 4.9 to 19.5 $V_f=2.1\times 10^{-3}$
Ultimate Tensile Strength GPa	$d\sigma_c/dV_f=1.09\pm 0.1$ 91% increase from 0.0054 to 0.01 $V_f=4.3\times 10^{-3}$	0.025 (drop cast film~0.058) 1818rpm $V_f=4.3\times 10^{-3}$	129% increase from 0.42 to 0.97 $V_f=1\times 10^{-3}$
Breaking Strength GPa	$d\sigma_B/dV_f=1.07\pm 0.1$ 197% increase from 0.0058 to 0.0093 $V_f=4.3\times 10^{-3}$	<i>Not presented</i>	<i>Not applicable</i>
Toughness MJ/m³	$dT/dV_f=594\pm 156$ 191% increase from 1.36 to 3.97 15.6J/g $V_f=4.3\times 10^{-3}$	11 (drop cast film~3.32) 1818rpm 34J/g $V_f=4.3\times 10^{-3}$	46% increase from 20.6 to 36.2 28J/g $V_f=1\times 10^{-3}$
Strain at Break	$d\varepsilon_B/dV_f=46\pm 5$ 55% increase from 0.36 to 0.56 $V_f=4.3\times 10^{-3}$	0.6 (drop cast film~0.09) 1818rpm $V_f=4.3\times 10^{-3}$	44% increase from 0.09 to 0.13 $V_f=5.4\times 10^{-4}$

Table 6.1: Summary of the mechanical results for PVA composites.

6.7 References.

1. Cadek, M., et al., *Morphological and mechanical properties of carbon-nanotube-reinforced semicrystalline and amorphous polymer composites*. Applied Physics Letters, 2002. 81(27): p. 5123-5125.
2. Cadek, M., et al., *Reinforcement of Polymers with Carbon Nanotubes: The Role of Nanotube Surface Area*. Nano Lett., 2004. 4(2): p. 353-356.
3. Coleman, J.N., et al., *High Performance Nanotube-Reinforced Plastics: Understanding the Mechanism of Strength Increase*. Advanced Functional Materials, 2004. 14(8): p. 791-798.
4. Vigolo, B., et al., *Macroscopic Fibers and Ribbons of Oriented Carbon Nanotubes*. Science, 2000. 290(5495): p. 1331-1334.
5. Dalton, A.B., et al., *Super-tough carbon-nanotube fibres*. 2003. 423(6941): p. 703.

6. Miaudet, P., et al., *Hot drawing of single and multiwall nanotube fibers*. Submitted to Nano Letters, 2005.
7. Coleman, J.N., et al., *Reinforcement of polymers with carbon nanotubes. The role of an ordered polymer interfacial region. Experiment and modeling*. Polymer, 2006. 47(26): p. 8556-8561.
8. Ko, F., et al., *Structure and Properties of Carbon Nanotube Reinforced Nanocomposites* AIAA, 2002.
9. Ko, F., et al., *Electrospinning of continuous carbon nanotube-filled nanofiber yarns*. Advanced Materials, 2003. 15(14): p. 1161-+.
10. Dror, Y., et al., *Carbon Nanotubes Embedded in Oriented Polymer Nanofibers by Electrospinning*. Langmuir, 2003. 19(17): p. 7012-7020.
11. Salalha, W., et al., *Single-walled carbon nanotubes embedded in oriented polymeric nanofibers by electrospinning*. Langmuir, 2004. 20(22): p. 9852-9855.
12. Liu, L.Q., et al., *One-step electrospun nanofiber-based composite ropes*. Applied Physics Letters, 2007. 90(8).
13. Zeng, J., et al., *Poly(vinyl alcohol) nanofibers by electrospinning as a protein delivery system and the retardation of enzyme release by additional polymer coatings*. Biomacromolecules, 2005. 6(3): p. 1484-1488.
14. Taepaiboon, P., U. Rungsardthong, and P. Supaphol, *Drug-loaded electrospun mats of poly(vinyl alcohol) fibres and their release characteristics of four model drugs*. Nanotechnology, 2006. 17(9): p. 2317-2329.
15. Zhou, W.P., et al., *Elastic deformation of multiwalled carbon nanotubes in electrospun MWCNTs-PEO and MWCNTs-PVA nanofibers*. Polymer, 2005. 46(26): p. 12689-12695.
16. Naebe, M., et al., *Effects of MWNT nanofillers on structures and properties of PVA electrospun nanofibres*. Nanotechnology, 2007. 18(22).
17. Kannan, P., S.J. Eichhorn, and R.J. Young, *Deformation of isolated single-wall carbon nanotubes in electrospun polymer nanofibres*. Nanotechnology, 2007. 18(23).
18. Jeong, J.S., et al., *Mechanical properties of electrospun PVA/MWNTs composite nanofibers*. Thin Solid Films, 2007. 515(12): p. 5136-5141.
19. Zhao, B., H. Hu, and R.C. Haddon, *Synthesis and properties of a water-soluble single-walled carbon nanotube-poly(m-aminobenzene sulfonic acid) graft copolymer*. Advanced Functional Materials, 2004. 14(1): p. 71-76.
20. Zhao, B., et al., *Synthesis and characterization of water soluble single-walled carbon nanotube graft copolymers*. Journal of the American Chemical Society, 2005. 127(22): p. 8197-8203.
21. Lee, J.S., et al., *Role of molecular weight of atactic poly(vinyl alcohol) (PVA) in the structure and properties of PVA nanofabric prepared by electrospinning*. Journal of Applied Polymer Science, 2004. 93(4): p. 1638-1646.
22. Koski, A., K. Yim, and S. Shivkumar, *Effect of molecular weight on fibrous PVA produced by electrospinning*. Materials Letters, 2004. 58(3-4): p. 493-497.
23. Blond, D., et al., *Enhancement of modulus, strength, and toughness in poly(methyl methacrylate)-based composites by the incorporation of poly(methyl methacrylate)-functionalized nanotubes*. Advanced Functional Materials, 2006. 16(12): p. 1608-1614.
24. Blond, D., et al., *Toughening of artificial silk by incorporation of carbon nanotubes*. to be submitted, 2007.
25. Khan, U. and J. Coleman, *Tough, super-ductile composites by addition of very low quantities of functionalised nanotubes to polyvinylchloride*. to be submitted, 2007.

26. Sen, R., et al., *Preparation of single-walled carbon nanotube reinforced polystyrene and polyurethane nanofibers and membranes by electrospinning*. Nano Letters, 2004. 4(3): p. 459-464.
27. Jeesang Hwang, J.M.T.G., *Electrical and mechanical properties of carbon-black-filled, electrospun nanocomposite fiber webs*. Journal of Applied Polymer Science, 2007. 104(4): p. 2410-2417.
28. Liu, L.Q., et al., *Tensile mechanics of electrospun multiwalled nanotube/poly(methyl methacrylate) nanofibers*. Advanced Materials, 2007. 19(9): p. 1228-+.
29. Callister, W.D., *Materials Science And Engineering An Introduction*, ed. t. editions. 2007.
30. Liu, L., et al., *Mechanical Properties of Functionalized Single-Walled Carbon-Nanotube/Poly(vinyl alcohol) Nanocomposites*. Advanced Functional Materials, 2005. 15(6): p. 975-980.
31. Wang, Y., Y.M. Xia, and Y.X. Jiang, *Tensile behaviour and strength distribution of polyvinyl-alcohol fibre at high strain rates*. Applied Composite Materials, 2001. 8(5): p. 297-306.
32. Hassan, C.M. and A.P. Nikolaos, *Structure and Applications of Poly(vinyl alcohol) Hydrogels Produced by Conventional Crosslinking or by Freezing/Thawing Methods* Advances in Polymer Science, 2004. 153: p. 37.
33. Ryan, K.P., *Polymer Crystallisation as reinforcement Mechanism for Polymer-Carbon nanotube*, in *School of Physics*. 2005, Trinity College Dublin: Dublin.
34. Pritchard, J.G., *Poly(vinyl alcohol); Basic properties and uses* Gordon and Breach Science Publishers, London, 1970.
35. Zhao, S.L., et al., *Electrospinning of ethyl-cyanoethyl cellulose/tetrahydrofuran solutions*. Journal of Applied Polymer Science, 2004. 91(1): p. 242-246.

Chapter 7: Conclusion & Future Work.

7.1 Conclusions.

New class of polymer composites have been successfully produced using carbon nanotubes as fillers in this thesis. These nanofillers were chosen because of their outstanding mechanical, thermal and electrical properties. The main focus of the work was to improve the mechanical properties of the composites compared to the neat polymer. For each study, this goal was achieved using a specific way of production. Furthermore, Mechanical improvements obtained in these composites were realised at a low loading level of carbon nanotubes.

The first polymer matrix investigated in this work was Poly (methyl methacrylate) (PMMA). Two types of composites were successfully produced with OH-MWNTs by in situ polymerisation, followed by solution mixing and drop-cast processing. The first composite was based on polymerised PMMA and polymerised PMMA with OH-MWNTs (Composite A). The second composite was formed from polymerised PMMA, PMMA with OH-MWNTs and commercial PMMA (Composites B). FTIR studies suggested that bonding between carbon nanotubes and PMMA may occur at the –OH functionality, and also at the outer layer of the CNTs. Mechanical properties have shown an increase in all the parameters investigated for a low content of carbon nanotubes in both systems (Composites A&B). Using Krenchel's rule of mixtures and Halpin-Tsai theories to calculate the theoretical enhancement of the Young's modulus failed to fit the experimental dY/dV_f for composite A. Shear stress, τ , was calculated with the two different models. The first model gave an unreasonably high value of 470 ± 400 MPa for composite A compared to the expected value of 50–100 MPa. However this model gave a more acceptable value of 133 ± 121 MPa for composites B. Therefore the second model, which takes into account the microscopy studies, was used to fit the experimental data of composite A. In this case the calculated polymer shear strength was found to be 88 ± 115 MPa. While this is much higher than the expected value of approximately 6.4 MPa, it is an acceptable value within the error. The range of this error can be explained by the large

variations in the lengths of the nanotubes as observed in the TEM studies. Finally, at higher mass fractions, the mechanical properties tend to fall off. This is probably due to aggregation effects at high concentration.

The second polymer matrix investigated in this thesis was Poly (L- lactic acid) (PLLA). Low and high molecular weight PLLA composites, with OH-MWNTs and SWNTs functionalised with octadecylamine, were produced by solution mixing and drop-casting processing. The best mechanical reinforcement was achieved with low molecular weight PLLA composites with OH-MWNTs. All the mechanical parameters investigated (Y , σ_C , σ_B , ϵ_B , T) show a linear increase, up to an optimum volume fraction of nanotubes, before falling off due to aggregation effects. Using the strength of fibre-reinforced composites, described by the rule of mixtures (equation 4.6), gives an acceptable value for τ (169.6 ± 155.6 MPa). This suggests that this model is valid for explaining the mechanical reinforcement. Thermal analysis has shown that nanotubes do not have an effect on the thermal degradation of the sample. Moreover, the glass transition and the percentage crystallinity do not undergo dramatic changes by the addition of CNTs. Using the same batch of OH-MWNTs with high molecular weight PLLA shows a lower mechanical reinforcement than the low molecular weight PLLA composites. One possible explanation is that long molecular chains may decrease the dispersion of CNTs, resulting in poor mechanical reinforcement. Using SWNTs functionalised with octadecylamine with high molecular weight PLLA also showed low reinforcement in the stiffness and strength. However, strain at break and toughness exhibited a dramatic increase of 264% and 225% respectively by adding 0.21 vol % of CNTs.

We also have produced nanotube-silk composites by mixing octadecylamine functionalised nanotubes and Biosteel in 1,1,1,3,3,3-Hexafluoro-2-propanol by drop-cast processing. The mechanical properties of the pure Biosteel films were lower than expected due to the effect of the strong denaturing solvent. Increases in stiffness, strength, ductility and toughness were observed at very low nanotube loading levels. Analysis of the rate of increase of stiffness with volume fraction shows extremely good polymer-nanotube stress transfer. However, all mechanical results saturate at a volume fraction of $\sim 0.1\%$ due to nanotube aggregation.

The last polymer matrix investigated was Poly (vinyl alcohol) (PVA). Polymer nanofibre composite films were produced using electrospinning techniques by adding m-poly (aminobenzene sulfonic acid) functionalised SWNTs (P8-SWNTs). Homogenous electrospun nanofibres were obtained with a water PVA solution at 250g/l using the following electrospinning parameters with a stationary plate collector: 20kv, 20cm and 0.003 ml/min. Raman spectroscopy was carried out to demonstrate that a good dispersion of nanotubes was present within the electrospun PVA films containing various volume fractions of P8-SWNTs. Mechanical measurements performed on these composites revealed a linear increase in all of the mechanical parameters investigated, (Y , σ_C , σ_B , ϵ_B and T), up to a maximum of 0.43 vol% of nanotubes. Above this concentration, all mechanical properties decreased, suggesting nanotube aggregation. The average density and porosity of these membranes were also calculated to be 205 kg/m³ and 84% respectively. Using the optimum loading level of nanotubes, electrospun composite membranes display a toughness of 15.56 J/g. This represents half the toughness of Kevlar® (33 J/g). DSC analysis showed a linear increase in the crystallinity up to 0.2vol% of nanotubes. DSC also established an increase in the crystallinity in this polymeric system, due to the electrospinning technique.

From these results, a study was carried out using a drum rotating collector to produce electrospun PVA membranes with 0.43 vol% of nanotubes with various speed rotations. We have demonstrated the effective alignment of nanofibres by increasing the speed rotation, using Fast Fourier Transform analysis and SEM characterisation. Electrospun composite membranes, obtained at the high rotation speed, displayed a Young's modulus and strength values in the same range as the drop cast film produced from the same solution. This is an interesting result since electrospun membranes display a density 5 times lower than drop cast films. More importantly, at the higher rotation speed, electrospun membrane demonstrated a toughness almost equivalent to Kevlar (27.86 J/g).

Finally, mechanical measurements were achieved on PVA nanofibres for various volume fractions of P8-SWNTs using an AFM. These nanofibres showed very brittle behaviour with no plastic deformations. The Young's modulus, tensile strength, strain at break and toughness were calculated from the force displacement curves using a simple mathematical model. Very high strength values were obtained, up to 0.9 GPa, for these nanofibres. Extremely high value for the enhancement Young's modulus has also been calculated (7 TPa). However, the model used to quantify the mechanical reinforcement did not explain the observed enhancement.

To conclude, the techniques used to achieve these composites are efficient at a low loading level of nanotubes. However, above 1wt% of CNTs, all the mechanical parameters investigated are falling off due to nanotube aggregations. This clearly highlights the limitation of these processes to improve further the mechanical properties of polymer composites. Therefore, new techniques are required to fully take advantage of the outstanding mechanical properties of carbon nanotubes by dispersing successfully these fillers at higher concentrations.

7.2 Future work.

The results presented here indicate the potential for carbon nanotubes in mechanical reinforcement. A significant amount of research is focused on this field using various nanoparticles and a wide range of polymers. However, success has been limited so far due to a lack of understanding of the interactions between the polymer, solvent and the nanoparticles involved. In this way, further studies should be carried out to understand the effect of octadecylamine functionalisation for the mechanical improvement of the PLLA composites. Post-processing composites is also an important aspect to take into account in order to optimise the potential reinforcement. With this in mind, attempts have been made to improve the mechanical properties of biosteel composites by post-drawing with water. However, a more accurate and systematic set-up is required to effectively improve the composite properties. Post-hot stretching processes could also be performed on PVA electrospun nanofibres to improve their properties. This process demonstrates a strong improvement in the mechanical properties on PVA/SWNTs achieved by coagulation spinning.

In the electrospinning study, we used functionalised SWNTs to help the dispersion of the nanotubes in a highly concentrated PVA solution. Further work would be required to evaluate the impact of the functionalised nanotubes on the mechanical properties by using as-prepared SWNTs instead. In addition, more measurements on single nanofibres using the AFM technique would also be needed with various batches of nanotubes to confirm the obtained results.

Finally but not presented in this thesis, electrospun low molecular weight PLLA membrane composites have also been produced using various concentration of as prepared SWNTs and SWNTs functionalised with octadecylamine. Morphological mechanical and thermal properties of these membrane composites were achieved. This study was done in collaboration with the National Centre for Biomedical Engineering Science (NCBES) in Galway (Ireland). The aim was to assess the feasibility of these materials as scaffolds for tissue engineering. However, more research needs to be address in this project. Similarly to the presented studies in this thesis, mechanical improvement is achieved with less than 0.5 wt% of carbon nanotubes. Unfortunately, improving the electrical properties of the scaffold is also required to overall properties of the scaffold for tissue engineering applications. To reach an electric percolation threshold more than 5 wt% of CNTs would be needed with such type of composites. Therefore more researches need to be addressed to obtain the desired electrical and mechanical properties.

APPENDIX: PUBLICATION LIST

First Author journal paper.

“Strong, tough electrospun polymer-nanotube composite membranes with extremely low density”.

Blond D, Blighe .F, Walshe W, Young K, McCauley J, Carpenter L, Almecija D, Blau WJ, Coleman JN.

(Accepted in *Advanced Functional Materials*)

“Toughening of artificial silk by incorporation of carbon nanotubes”

Blond D, McCarthy D, Blau WJ, Coleman JN.

Biomacromolecules 8, 3973–3976 (2007)

“Enhancement of modulus, strength, and toughness in poly(methyl methacrylate)-based composites by the incorporation of poly(methyl methacrylate)-functionalized nanotubes”.

Blond D, Barron V, Ruether M, Ryan KP, Nicolosi V, Blau WJ, Coleman JN.

Advanced Functional Materials 16 (12):1608-1614 (2006)

Co-author journal paper.

“Carbon nanotubes for reinforcement of plastics? A case study with poly(vinyl alcohol)”.

Ryan KP, Cadek M, Nicolosi V, Blond D, Ruether M, Armstrong G, Swan H, Fonseca A, Nagy JB, Maser WK, Blau WJ, Coleman JN.

Composites Science and Technology 67 (7-8): 1640-1649 (2007)

Co-author conference proceedings.

“Effect of Nanotube Type on the Enhancement of Mechanical Properties of Free-Standing Polymer/Nanotube Composite Films”.

Cadek M, Coleman JN, Blond D, Fonseca A, Nagy JB, Szostak K, Béguin F, Blau WJ.

AIP Conference Proceeding, 685, 269-277 (2003).

“Characterisation of Nanotube Based Artificial Muscle Material”.

Kiernan G, Barron V, Blond D, Drury A, Coleman JN, Murphy R, Cadek M, Blau WJ

Journal Proceedings SPIE, 4876, 775-783 (2002).